university of groningen

MASTER THESIS

Increasing the intensity of a slow molecular beam using an electrostatic hexapole

Author:
Joost W. F. van Hofslot

First examiner:
Prof. Dr. Steven HOEKSTRA

Second examiner:
Prof. Dr. Hendrick BETHLEM

A thesis submitted in fulfillment of the requirements for the degree of Master of Science

in the

Van Swinderen Institute for Particle Physics and Gravity

September 30, 2021

UNIVERSITY OF GRONINGEN

Abstract

Increasing the intensity of a slow molecular beam using an electrostatic hexapole

by Joost W. F. van Hofslot

Heavy polar diatomic molecules can be used as sensitive probes of violations of fundamental symmetries. The NL-eEDM collaboration works towards a measurement of the permanent electric dipole moment of the electron using a slow, cold and intense beam of BaF molecules, to possibly find evidence of physics beyond the Standard Model. Steps towards this goal have been taken using a SrF beam, which is generated by a cryogenic buffer gas source, slowed down using a 4.5 meter traveling wave Stark decelerator and detected using laser induced fluorescence spectroscopy.

Due to the distance between vacuum elements, phase space matching between the source and decelerator is suboptimal, leading to the loss of molecules with larger transverse velocities. This work outlines the operating principles, design, implementation and testing of an electrostatic hexapole located between the source and decelerator. The lensing effect of the hexapole is estimated to increase the number of decelerated SrF molecules by at least a factor 2 using ac-guiding at 190m/s measurements. The combined effect of the hexapole lens and the addition of ac-guiding sections to the waveform are shown to increase the number of detected molecular packets in the fluorescence time of flight signal. Consequently, the factor gain due to the hexapole in number of molecules obtained at the end of the decelerator when decelerating to 30 m/s is likely larger than the factor 2 obtained using ac-guiding at 190 m/s. An electric field shield is designed to minimize the influence of latent electric fields on the fluorescence measurement.

A definitive conclusion on the intensity increase which can be attributed to the hexapole is currently impossible. The detection laser samples only a small part of the molecular beam that exits the decelerator, and therefore only a small fraction of the total amount of guided or decelerated molecules is detected. Therefore, the factor 2 is likely an underestimate. Lastly, the discrepancy between measurements and simulations suggests that further analyses of the detection zone volume and the acceptance of the decelerator need to be conducted.

With the hexapole in place, the focus can turn towards laser cooling of BaF, for which a custom vacuum chamber is designed and delivered. Reducing the tranverse velocity of the beam is an essential step towards an eEDM measurement using a slow, intense and cold beam of BaF molecules.

Contents

Chapter 1

Introduction

1.1 The adequate but incomplete Standard Model

Particles, forces, and an insight into the most fundamental aspects of nature: using these ingredients, the Standard model of Particle Physics (SM) encompasses an experimentally verified theoretical framework to describe nature at the smallest scales. The SM is widely regarded as the most successful theory in physics. Since it's inception in the 1970, the SM has correctly explained and predicted a wide variety of phenomena relating to high energy particle physics, culminating in the prediction and subsequent discovery of the top quark [1] and the Higgs boson [2].

While the SM currently serves as our best description of particle physics, there remain certain phenomena it cannot explain. Among these is the hierachy problem, relating to the number of elementary particle families and their relative energy scales and masses [3], the existence of dark matter [4], the quantification of gravity (or lack thereof) [5], the observed asymmetry between the amount of matter and antimatter in the universe [6] and more recently the positive muon magnetic anomaly [7].

Quantum field theories such as the SM must abide by the $\mathcal{CPT}$ symmetry principle, which states that the model should be invariant under the combined operation of charge conjugation $\mathcal{C}$, space inversion or parity conjugation $\mathcal{P}$, and time reversal $\mathcal{T}$ [8]. Assumed validity of the $\mathcal{CPT}$ theorem implies that for instance $\mathcal{T}$ symmetry violation is equal to combined $\mathcal{C}$ and $\mathcal{P}$ or $\mathcal{CP}$ symmetry violation. One such example of $\mathcal{CP}$ violation is the slightly different weak interaction of particles and antiparticles, originating from the interaction of leptons and quarks with the Higgs field [9][10]. A second example is the potential presence of a nonzero permanent electric dipole moment (EDM) in a composite or elementary particle [11]. The EDM is quantum mechanical effect describing a potentially asymmetric interaction between a particle and an electric field, due to an intrinsic property of the particle [12][13]. The classical equivalent of such an interaction would be an uneven distribution of charge [14].

The complex phase present in the CKM matrix ensures that a certain amount of $\mathcal{CP}$ violation is incorporated into the SM [10], to explain for instance the neutral kaon to pion decay [15]. However, this amount is insufficient to explain the matter versus antimatter asymmetry of the universe, under the assumption that the net baryon and lepton numbers might both have taken the symmetrical value of zero in the early universe [16][17][18]. Extensions of the SM typically contain additional sources for $\mathcal{CP}$ violation in various magnitudes. Therefore, probing $\mathcal{CP}$ violating observables is central to achieving a deeper understanding of nature, as the magnitude and origin of these observables can tell us which theory might eventually extend or succeed the Standard Model.

1.2 Thesis outline

The NL-eEDM collaboration is currently building a setup to conduct an eEDM measurement using a slow, cold and intense beam of BaF molecules. The work presented in this thesis mainly concerns the production of the required molecular beam, which uses a cryogenic buffer gas source and a traveling-wave Stark decelerator. Specifically, the aim is to increase the intensity of the decelerated beam, a necessary step towards a competitive measurement of the eEDM.
Chapter 2 briefly highlights the parameters with an influence on the sensitivity of an eEDM precision experiment using a molecular beam. The operating principles of the beam production components are discussed.
Chapter 3 describes the work conducted to design, create, implement and test an electrostatic hexapole such that an optimal phase space matching between the molecular beam and the decelerator is achieved, which translates to an increase in the intensity of the decelerated beam.

Chapter 2

Background and theory

Heavy polar diatomic molecules can be used as sensitive probes of violations of fundamental symmetries. One such symmetry violation is a nonzero magnitude of the electron electric dipole moment, or eEDM. If an eEDM value larger than that predicted by the Standard Model is measured, this would signal physics beyond the Standard Model. The NL-eEDM collaboration is currently building a setup to conduct an eEDM measurement using a slow, cold and intense beam of BaF molecules. This chapter briefly highlights the parameters with an influence on the sensitivity of an eEDM precision experiment using a molecular beam. Steps towards the final NL-eEDM setup have been taken using a SrF beam, which is generated by a cryogenic buffer gas source, slowed down using a 4.5 meter traveling wave Stark decelerator and detected using laser induced fluorescence spectroscopy.

2.1 Fundamental physics, CP violation and electric dipole moments

The field of EDM experiments was launched in 1952, after Ramsey and Purcell proposed that elementary particles could possess a permanent electric dipole moment [19]. Figure 2.1 shows the effects of $\mathcal{C}$, $\mathcal{P}$ and $\mathcal{T}$ conjugation performed on such a fundamental particle with spin S and a charge distribution such that a permanent EDM d is present. According to the Wigner-Eckart theorem, the effective dipole moment of such a particle must lie along its spin [17]. The parity conjugation $\mathcal{P}$ reverses the direction of d_e but does not change spin S. The time conjugation $\mathcal{T}$ reverses the direction of S but leaves d_e unchanged. Therefore, if a non-zero permanent electric dipole moment d_e were to be observed in for instance an electron, it would signal both $\mathcal{P}$ and $\mathcal{T}$ violation, and consequently $\mathcal{CP}$ violation.

The search for additional sources of $\mathcal{CP}$ violation through EDM signatures can be categorized in various classes of experiments: neutrons, paramagnetic atoms and molecules which have unpaired electrons, diamagnetic atoms with paired electrons, and hadrons [21]. Each class of EDM experiments provides sensitivity to a different combination of $\mathcal{CP}$ violating mechanisms.

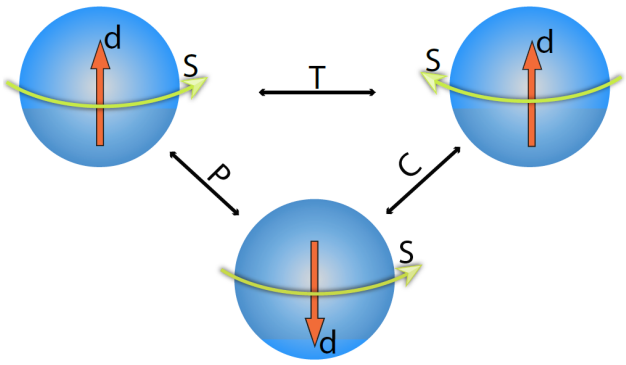

FIGURE 2.1: A fundamental particle with spin s and permanent EDM d subject to operations $\mathcal{C}$, $\mathcal{P}$ and $\mathcal{T}$ [20].

2.1.1 Neutron EDM

Initial experiments searching for a $\mathcal{CP}$ violating EDM signal chose to use widely available neutron beams, as such a neutral particle - compared to protons or electrons - would not experience an acceleration when exposed to an electrostatic field. A more thorough exposition of the motivation behind this choice is provided in [22]. The previously mentioned Ramsey himself stated that the fact that the total charge of the neutron is zero does not immediately mean that the charge distribution should be zero everywhere [23]. Since neutrons are comprised of quarks, the nEDM or neutron EDM provides an interesting probe of the $\mathcal{CP}$ violating parameter θ, a nonzero vacuum angle in the QCD model [24]. This angle θ contributes to the nEDM with the order $\theta \times$ neutron diameter. Current experimental endeavours have determined θ to have an upper limit of $\mathcal{O}(10^{-10})$ [25][26], and the question of why θ is so small or even zero is dubbed the 'Strong CP problem' [27][28].

2.1.2 Electron EDM and paramagnetic molecules

An EDM signal in paramagnetic systems originates from the unpaired electron's EDM (eEDM) and electron-nucleon scalar-pseudoscalar interactions [21][29]. The coupling constants associated with these effects are d_e and k_s, respectively [30]. Especially interesting are paramagnetic polar diatomic molecules containing heavy atoms, in which the effect of the eEDM is greatly enhanced [31][32].

The enhancement factor originates from the relativistic velocities of electrons near the nucleus, and can be quantified in terms of an effective electric field $E_{eff} \approx 8Z^3\alpha^2 E_{ext}$, with atomic number Z, fine structure constant α and external electric field E_{ext} [33][34][35][36]. The factor Z^3 indicates a preference for systems containing heavy nuclei. The parameter E_{eff} cannot be directly measured. Instead, it has to be obtained from molecular structure calculations. The effect of these relativistic electrons is smaller in diamagnetic systems due to their closed electron shells. In such systems, the Schiff theorem states that the nuclear dipole moment causes the atomic electrons to rearrange themselves so that they develop a 'screening' dipole moment opposite that of the nucleus [37]. Therefore, diamagnetic systems do not experience the aforementioned enhanced sensitivity to the eEDM, and are better suited for studying hadronic sources of $\mathcal{CP}$ violating processes that are expected to produce an EDM signal [38].

An added benefit of paramagnetic molecules compared to atoms is their high polarizability originating from nearly degenerate opposite-parity rotational levels, which allows them to be nearly fully polarized with realistically achievable electric fields [39][14]. The attainable degree of polarization can greatly exceed that of an atom exposed to such an electric field [40][39]. A high degree of polarization is a key ingredient for preparation of the state in which the eEDM induced interaction energy is to be measured.

Though their complex structure and energy levels make molecules challenging to control, the advantages listed above far outweigh the drawbacks due to complexity [41]. With the enhancement factor for eEDM sensitivity and polarizability in mind, paramagnetic polar diatomic molecules with a large mass difference present attractive subjects for fundamental physics research concerning $\mathcal{CP}$ violating phenomena.

2.2 Measuring the eEDM

The $\mathcal{CP}$ violating mechanisms incorporated in the SM predict an extremely small eEDM value of $d_e \sim \mathcal{O}(10^{-38})\ e \cdot \text{cm}$, originating from vacuum fluctuations and interactions with virtual particles on the fourth- or quark loop level in their Feynman diagram [42][43]. Unfortunately, this is a magnitude far below that which can be probed with present-day experimental sensitivities. The current upper limit on the eEDM was measured to be $|d_e| < 1.1 \times 10^{-29}\ e \cdot \text{cm}$ and consistent with zero, obtained in 2018 by the ACME collaboration using the paramagnetic ThO molecule [44].

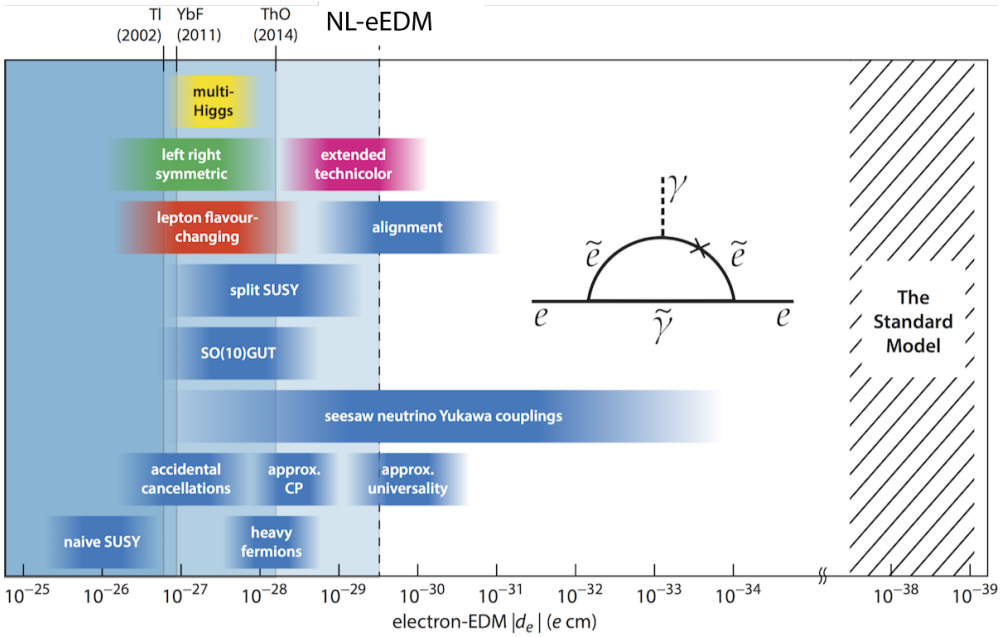

FIGURE 2.2: Experimental eEDM upper bounds compared to eEDM magnitude predicted by various Standard Model extensions [45].

However, various extensions of the SM contain additional sources of $\mathcal{CP}$ violating processes, and predict the value d_e to be orders of magnitude larger, within reach of current experimental techniques [31]. A number of these extensions and their corresponding predicted eEDM values are shown in Figure 2.2. The difficulties accompanied with these extensions originate from the fact that they often involve particles with large masses or extremely weak interactions, which require large and expensive experiments such as the LHC to detect. Acting complimentary to such enormous facilities, eEDM experiments present a low-energy, high precision laboratory scale method for finding physics beyond the Standard Model.

2.2.1 Experimental signature and relevant parameters

All EDM experiments are based on observing the effect of an external electric field $\vec{E}_{ext}$ on the subject particle, clouded by much larger magnetic effects [46]. A brief summary of recent eEDM experiments is shown in Table 2.1. Similar to the interaction between a magnetic dipole moment μ with a magnetic field $\vec{B}$, the electron EDM d_e will shift the energy levels of the particle when it is exposed to an external electric field E_{ext}. The corresponding Hamiltonian describing these two interactions is written as $\hat{H} = -\mu\vec{B} - d_e\vec{E}_{eff}$ [42], where E_{eff} is connected to E_{ext} through the enhancement factor. The induced shift in energy levels is shown in Figure 2.3. For molecular beam experiments, the required external electric field $\vec{E}_{ext}$ is usually generated by two parallel plane electrodes, with the enclosed volume where the molecules can interact with the electric and magnetic field referred to as the interaction region. The relevant observable for particles propagating in free flight between these plates is the spin precession frequency or energy level difference, which can have contributions due to both an electric- and magnetic dipole moment [36][47].

For a paramagnetic polar diatomic molecule, the interaction of the eEDM with the strong effective electric field of the polarized molecule leads to spin precession. When the molecule resides in the eEDM measurement state, the spin precession frequency will increase or decrease when a parallel or antiparallel external magnetic field $\vec{B}$ is also present in the interaction region, respectively, depending on the

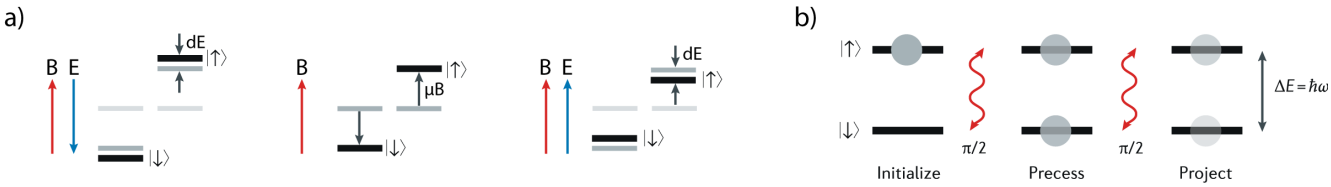

FIGURE 2.3: **a)** In the presence of an external electric field $\vec{E}_{ext}$ oriented parallel or antiparallel to an applied magnetic field $\vec{B}$, a permanent EDM d (with state vectors $|\uparrow\rangle$ and $|\uparrow\rangle$ w.r.t. $\vec{E}_{ext}$) is detectable as a modification (dark grey) of the Zeeman splitting (black). The energy levels shift closer together or further apart, i.e. $\Delta E(\vec{B} \uparrow\downarrow \vec{E_{ext}}) = (2\mu B + dE)$ and $\Delta E(\vec{B} \uparrow\uparrow \vec{E_{ext}}) = 2(\mu B - dE)$, respectively. **b)** Spectroscopic sequence used to detect the phase difference in the spin precession. A rf pulse creates the superposition in which the eEDM dependent phase difference is accumulated. Figure adapted from [47]

direction of $\vec{E}$. Since $\vec{E}$ can be parallel and antiparallel to $\vec{B}$ in two directions, a total of 8 different energy shifts can be measured [48]. The magnetic field induced energy shift presents an additional experimental complication, aside from the tiny magnitude of the eEDM. The magnetic contributions to the spin precession present a source of systematic errors, as it can create a 'fake' eEDM signal if the magnetic field is not sufficiently understood, controlled, perfectly reversed and mitigated. By switching the polarity of the field plates to change the orientation of $\vec{E}_{ext}$ between parallel or antiparallel with respect to $\vec{B}$, the magnetic contribution to the spin precession can be cancelled out [46].

Before entering the interaction region, a $\pi/2$ pulse brings the molecules into a superposition of two hyperfine substates, which is sensitive to both parallel or antiparallel alignment between the eEDM d_e and the magnetic field $\vec{B}$. In the NL-eEDM experiment, this superposition consists of the $m_f = \pm 1$ substates of the $X^2\Sigma^+, N = 0, F = 1$ state. As the molecules then propagate through the magnetically shielded interaction region, the superposition of the eEDM sensitive hyperfine substates builds up a spin precession phase. The eEDM magnitude can be detected through a difference in the total accumulated phase between the parallel and antiparallel orientation of the electric and magnetic fields [9]. After propagating through the interaction region, the superposition is projected back onto the $N = 0, F = 0$ using a second $\pi/2$ pulse. The number of molecules that end up in this state depend on the detailed evolution of the superposition in the fields [48]. A laser induced fluorescence transition is used to excite the molecules from the $N = 0, F = 0$ and $N = 0, F = 1$ states to an electronically excited state. The probabilities p_0 and p_1 to find a molecule in the $F = 0$ and $F = 1$ states scales according $p_0 \propto \cos^2 \Phi_{EDM}$ and $p_0 \propto \sin^2 \Phi_{EDM}$, respectively. The quantities a_0 and a_1, corresponding to the number of fluorescence counts recorded for the decay from excited molecules, will trace out two sinusoidal curves (or Ramsey fringes) of opposite phase as a function of applied magnetic field [49], and can be combined to define an asymmetry $\mathcal{A}$:

$$\mathcal{A} = \frac{a_0 - a_1}{a_0 + a_1} \sim 2B\Phi_{EDM} \tag{2.1}$$

The experiment measures Φ_{EDM} by measuring the change in $\mathcal{A}$ after reversing the polarity of the electric field plates. Therefore, the eEDM experiment amounts to counting the number of particles that result in each spin state [47]. A graphical view of the corresponding spectroscopic sequence is shown in Figure 2.3.

For a heavy diatomic polar molecule, the total accumulated phase difference Φ_{EDM} due to the eEDM can be expressed as follows [9][50]:

$$\Phi_{EDM} = \frac{d_e |P| E_{eff} \tau}{\hbar} \tag{2.2}$$

Where $|P|$ denotes the polarisation factor of the molecule and τ the coherent interaction time or spin precession time. Using the quantum shot noise limit, the statistical uncertainty σ_d corresponding to an

eEDM measurement can be expressed as follows [9][17][51]:

$$\sigma_d = \frac{\hbar}{e} \frac{1}{2|P|E_{eff}\tau\sqrt{\dot{N}T}} \tag{2.3}$$

Where the counting rate $\dot{N}$ and the measurement time T combine to produce the total amount of detected particles N_{tot}. Here, $\dot{N}$ is the product of the fraction of detected fluorescence photons and the number of molecules in the addressed N state [52]. The parameters listed in equation 2.3 are useful to discuss the main requirements for a successful eEDM measurement and are further discussed below. Each type of experiment will favor certain parameters more than others. When designing an eEDM experiment, the goal is to maximize the combination of parameters $|P|, E_{eff}, \tau, \dot{N}$ and T.

TABLE 2.1: Figure of merit comparison between completed and ongoing eEDM experiments using polar diatomic molecules. Red denotes projected values. YbF, ThO and BaF are beam experiments, HfF^+ uses a rf trap.

Molecule	Year	Electronic state	E_{eff}, GV/cm	$\dot{N}$ in /s	τ in ms	eEDM in $e \cdot$ cm	References
YbF	2011	$X^2\Sigma_{1/2}$, ground	15-25	10^9	1	$d_e < 1.1 \cdot 10^{-27}$	[50][53][54][55]
HfF^+	2017	$^3\Delta_1$, metastable	23	10	700	$d_e < 1.3 \cdot 10^{-28}$	[56][57][58]
ThO	2018	$^3\Delta_1$, metastable	75-84	10^{11}	1	$d_e < 1.1 \cdot 10^{-29}$	[44][57]
BaF	-	$X^2\Sigma_{1/2}$, ground	6-8	$7 \cdot 10^5$	15	$d_e < 5 \cdot 10^{-30}$	[9]

Effective electric field and polarization factor

The role of the external electric field in a molecular eEDM experiment is to align the molecules [48]. The average projection of the internal electric dipole moment of the molecules onto the direction of the applied electric field $\vec{E}_{ext}$ can be expressed as the polarization P [59]. Complete polarization means that the internuclear axis, which points from the positive/heavy to the negative/light nucleus, and consequently the effective electric field of the molecule, is on average maximally aligned in the lab frame either parallel or antiparallel to the external electric field [13]. A graphical depiction of this large degree of polarization is shown in Figure 2.4. In line with that analogy, some suggest it is more appropriate to replace the previously mentioned E_{eff} by $E_{eff,max}$ and write $E_{eff} = PE_{eff,max}$, where $E_{eff,max}$ is the maximum effective field seen by the electron when the molecule is fully polarised in the case of $P = 1$ [60]. Equation 2.3 shows that a factor two decrease in the obtained degree of polarisation $|P|$, requires a factor four increase in the total measurement time T. Therefore, a large degree of polarization using lab accessible electric field strengths is a requirement since this decreases measurement time, and produces the largest possible Stark shift and total spin precession, and consequently eEDM sensitivity.

Coherence time

Coherence time can be visualised as the amount of time which the superposition, consisting of for instance the previously mentioned eEDM sensitive $m_f = \pm 1$ hyperfine substates, spends inside the electric and magnetic fields. The achieved coherence time in beam experiments is usually a trade off between velocity of the beam and length of the interaction region. The HfF^+ eEDM experiment consisted of HfF^+ located inside a radiofrequency trap with a relatively high coherence time of $\sim$ 700ms [56]. The molecular ions are trapped using an electric field that rotates in the radial plane. While stricly not related to the coherence time, both the HfF^+ and ThO experiments have the advantage of systematic error rejection due to the parity doublet of the metastable $^3\Delta_1$ state, which means that no reversal of external fields is needed [32][62]. However, the metastable state bears a disadvantage in its limited lifetime and consequently the maximum achievable coherence time. The next generation of the HfF^+ experiment

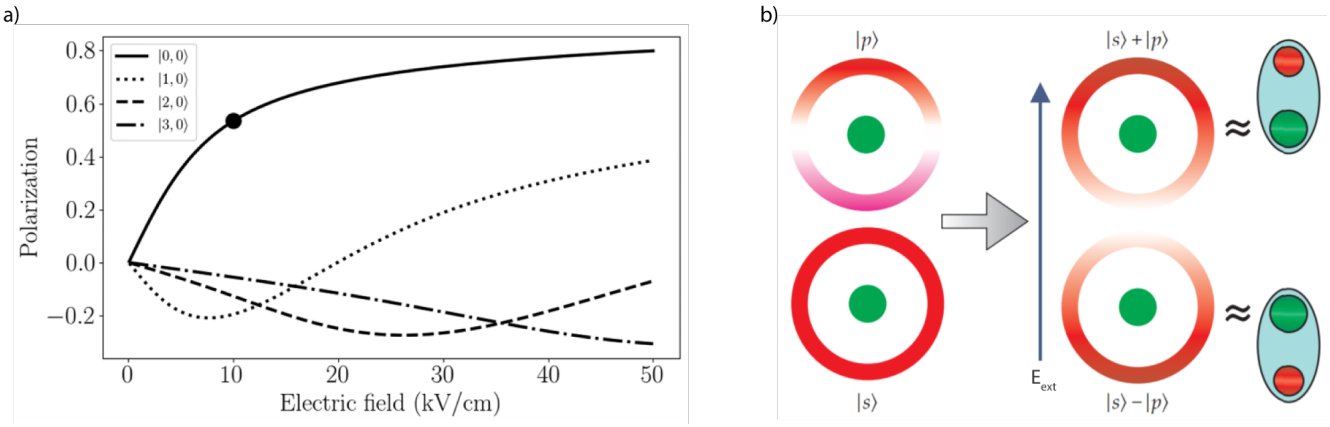

FIGURE 2.4: **a)** Polarization curves of the four lowest rotational states of $X^2\Sigma^+$ BaF, labeled $|N, M_N\rangle$ [31]. The eEDM measurement state $|0,0\rangle$ can achieve a polarization factor of $\sim$ 0.55 at field strengths aimed for by the NL-eEDM experiment, as indicated by the dot. The upper bounds on E_{eff} listed in Table 2.1 generally assume a polarization factor of close to 1. **b)** An external electric field E_{ext} results in results in mixing of close-lying opposite-parity rotational states to produce a large degree of polarization. This mixing can be illustrated using hydrogenic $|s\rangle$ and $|p\rangle$ orbitals [47]. These orbitals are shown for a light, negatively charged atom (red) orbiting a heavy positive atom (green). The shading of the red wavefunction denotes amplitude, with pink negative and white zero. Here, $|s\rangle$ denotes the ground-state, parity-even, J = 0 wavefunction and $|p\rangle$ the parity-odd, first-excited-state, J = 1 wavefunction. Wavefunction interferences yield configurations where the internuclear axis of the molecule aligns parallel to ($|s\rangle$) or antiparallel to ($|p\rangle$) to the applied external electric field, which corresponds to fully polarized molecules. Figure from [61].

aims to use ThF^+ to achieve a coherence time of up to 20 s, along with an increased effective electric field [63].

Counting rate and measurement time

The combination of counting rate and measurement time produce the total number of detected molecules. Important factors here are for instance the molecular beam intensity, detection efficiency, the amount of molecules in the eEDM measurement state, the repetition rate of the experiment and down time between repetitions. The success of the most recent ACME/ThO measurement, mentioned in Section 2.2, is largely attributable to the extremely high count rate achieved using a buffer-gas cooled molecular beam [59][47]. This more than counteracts the relatively short coherence time of $\tau \sim$ 1ms.

2.3 A slow, cold and intense molecular beam for an eEDM experiment

A joint effort between the Van Swinderen Institute connected to the University of Groningen and the LaserLaB Amsterdam at the VU University, the NL-eEDM collaboration works towards a measurement of the permanent electric dipole moment of the electron. A detailed description of the proposed experiment is provided in [9]. A slow, cold and intense beam of heavy polar paramagnetic BaF molecules will be used to measure the eEDM with a projected sensitivity at the 10^{-30} $e \cdot$ cm level. The full proposed experimental setup is shown in Figure 2.5.

The BaF molecule has a smaller effective electric field compared to molecules used for previous record breaking eEDM measurements using the heavier YbF, HfF^+ and ThO molecules, as shown in Table 2.1. However, a competitive measurement is still possible when combining the techniques of cryogenic buffer gas generation of molecular beams, Stark deceleration and laser cooling, as the combination of these elements is projected to produce a relatively high counting rate $\dot{N}$ and coherence time τ. Aside from the previously mentioned eEDM sensitivity, the choice for BaF is motivated by it's favourable Stark

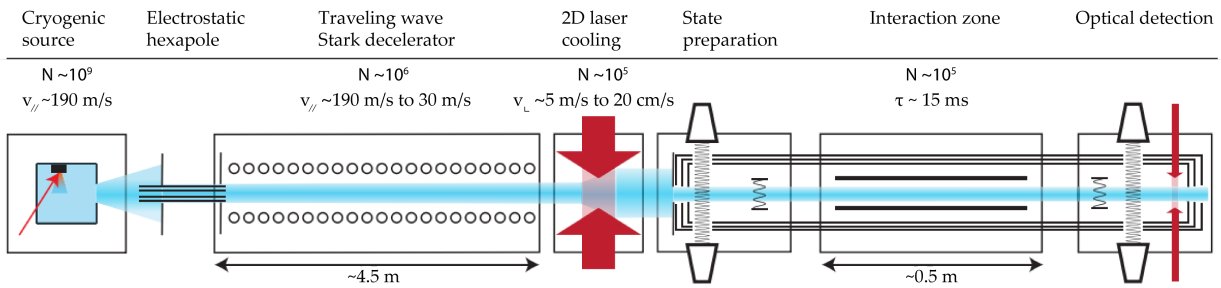

FIGURE 2.5: Figure of merit representation of the experiment proposed by the NL-eEDM collaboration [9][20].

shift combined with a relatively low mass, and highly diagonal Franck-Condon factors, which enable efficient deceleration at relatively modest field strengths and reliable fluorescence detection, respectively. The latter even opens up the possibility of laser cooling through optical cycling of $\sim 10^3$ photons.

In the run-up to the final eEDM measurement, the setup is divided over three laboratories, focused on source optimization, beam production and conducting an eEDM measurement. The eEDM measurement lab conducts BaF spectroscopy to investigate the parameters needed for efficient laser cooling, oversees the development and testing of the magnetic shield, and cultivates the expertise required for setting up the eEDM phase measurement. The beam production lab, where this project was executed, is tasked with generating the required slow, cold and intense beam and currently houses the cryogenic source, hexapole, Stark decelerator and in the near future the laser cooling chamber. The source optimization lab is dedicated to optimizing the cryogenic source such that the produced number of molecules in the desired low field seeking rotational state, with a velocity that still enables efficient deceleration, is maximized. Investigations include different cell geometries, carrier gases and ablation methods.

Throughout this project, molecular beam deceleration results are obtained using a SrF beam, which is generated by a cryogenic buffer gas source, slowed down using a 4.5 meter traveling wave Stark decelerator and detected using laser induced fluorescence spectroscopy. Sections 2.3.1 through 2.3.4 briefly cover each component in the Slow beam lab, present at the start of the project.

2.3.1 The Stark effect and traveling-wave Stark deceleration

The Stark effect describes a change in molecular energy levels due to interaction with an applied electric field and plays a central role in the NL-eEDM experimental setup, providing both the mechanism for manipulation of the molecular beam and the build up of the eEDM dependent phase difference mentioned in Section 2.2.1.

The Stark effect in polar diatomic molecules

The following description of the Stark effect for SrF and BaF is based on those found in [20][65][66]. As the rotational constant B of BaF is very similar to that of SrF (0.21 cm^{-1} versus 0.25 cm^{-1}, respectively [65]), the Stark shift of BaF closely resembles that of SrF. The momenta and group representation of a molecule is commonly written down in the molecular term symbol $^{2S+1}\Lambda_\Omega$. When applied to SrF/BaF, the electronic ground state $X^2\Sigma^+$ obtains it's total spin $S = 1/2$ from a lone valence electron and has total electronic angular momentum $L = 0$. The $^+$ indicates the reflection symmetry in any plane containing the internuclear axis. The rotational states of SrF and BaF in the $X^2\Sigma^+(v = 0)$ state are best described by Hund's case b, shown in Figure 2.7. The good quantum numbers for Hund's case b are Λ, N, S and J. Here, L is strongly coupled to the internuclear axis $\hat{z}$ and projected as Λ, Λ is coupled to angular momentum of the rotating nuclei R to form total angular momentum without spins N and N

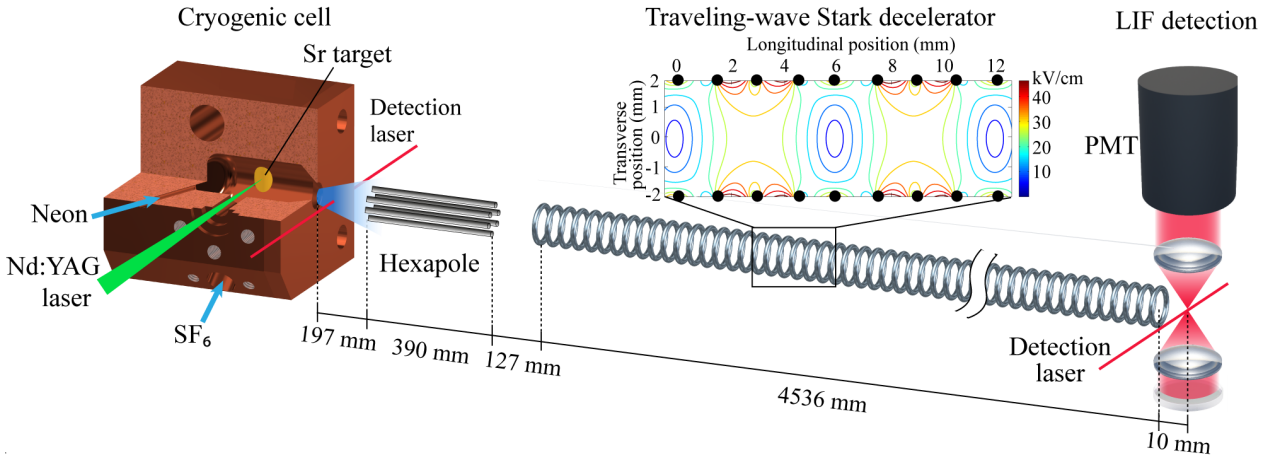

FIGURE 2.6: Experimental setup at the end of this project. Beamline elements indicated are not to scale. SrF molecular beams are produced in a cryogenic buffer gas source. After exiting the cryogenic cell through an orifice with a diameter of 4.5 mm, part of the beam is refocused using a 390 mm long electrostatic hexapole with an inner diameter of 12 mm, located between two sections of free flight. Next, the beam enters the first 4 mm inner diameter ring of the 4536 mm long traveling-wave Stark decelerator, in which it is usually guided at a constant velocity or decelerated at a constant deceleration strength. After leaving the decelerator, molecules are detected using laser induced fluorescence. Figure adapted from [64].

is coupled to electronic spin angular momentum S to form total angular momentum excluding nuclear spin J: $J = N + S = \Lambda\hat{z} + R + S$ [67]. In Hund's case b, spin-orbit coupling is weak and consequently Ω, the projection of J along the internuclear axis, is undefined.

The Stark effect for polar diatomic molecules in the $^1\Sigma$ state with rotational constant B occurs when the intrinsic electric dipole moment d interacts with an external electric field $\vec{E}_{ext}$, thereby shifting the rotational energy levels by an amount $\Delta\mathcal{E}_s$. For small electric fields, where the interaction of the molecule's dipole moment d with the electric field is much smaller than the interaction between the nuclear spin I and rotational angular momentum N, a second order perturbative approach gives the following energy shift [68][69]:

$$\Delta\mathcal{E}_s(N,M) = \frac{d^2\vec{E}^2}{Bhc} f(N,M), \text{ where } f(N,M) = \frac{1}{2}\frac{N(N+1) - 3M^2}{N(N+1)(2N-1)(2N+3)} \tag{2.4}$$

Where the azimuthal quantum number M is introduced, which denotes the projection of rotational quantum number N along the external electric field axis instead of the internuclear axis. Since M ranges from $-N$ to N, the resulting energy shift consists of $2N+1$ sublevels. In the $X^2\Sigma^+$ state, $f(0,0) = -1/6$, which leads to a Stark shift of $\Delta\mathcal{E}_s(0,0) = -\frac{d^2E^2}{6Bhc}$. Furthermore, $\Delta\mathcal{E}_s(1,0) = \frac{d^2E^2}{10Bhc}$ and $\Delta\mathcal{E}_s(1,1) = -\frac{d^2E^2}{20Bhc}$. The resulting force $\vec{F} = -\vec{\nabla}\mathcal{E}(E)$ is directed opposite to the gradient of the Stark energy.

An important distinction between positively and negatively shifted states arises. A positive Stark shift, such as $\Delta E_s(1,0)$, indicates that molecules will gain energy with an increased electric field, and are therefore attracted to local minima. Such a state is commonly referred to as 'low field seeking' (LFS). Similarly, a negative Stark shift indicates a high field seeking (HFS) state.

However, the quadratic behaviour shown in equation 2.4 does not infinitely hold for increasing electric field strength. The Hund's case labeling is based on the hierarchy in interaction strengths. For heavy molecules with small rotational constants, such as SrF and BaF, only a small electric field is required to obtain complete mixing of close-lying rotational states. At higher field strengths, when the Stark

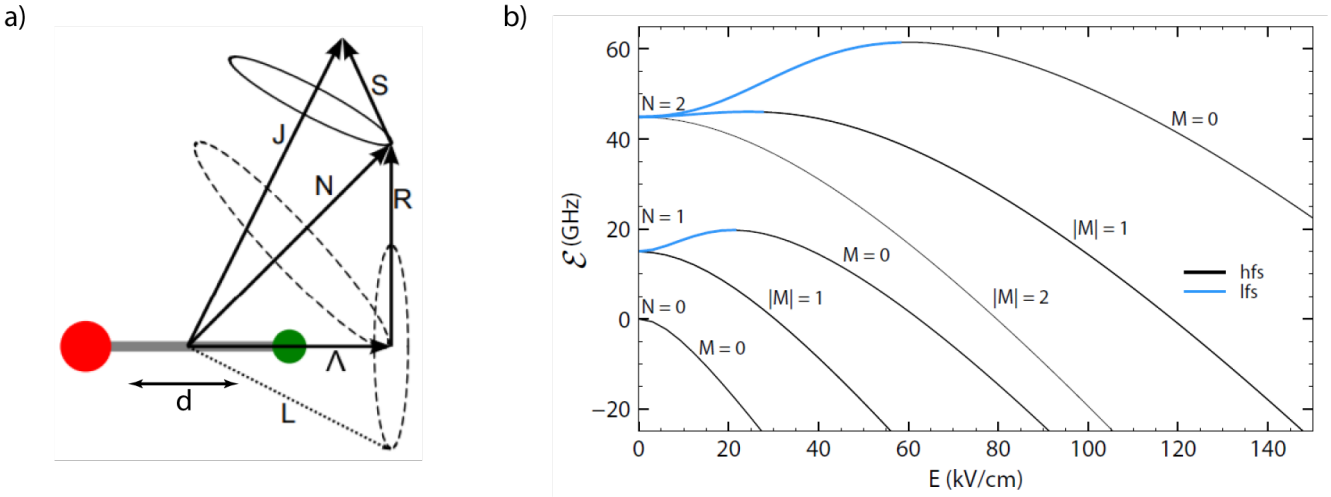

FIGURE 2.7: **a)** Hund's case b occurs for strong electronic coupling, weak spin-orbit coupling and mediocre rotational coupling. Rotation R occurs in and out of the plane [67]. **b)** Stark shift of SrF $X^2\Sigma^+$ with ($v = 0$) for different rotational quantum numbers N [20].

shift is large compared to the interaction energy between neighbouring rotational levels, the behaviour becomes linear due to mixing with rotational levels that are not direct neighbours. At this point, the quantum numbers of Hund's case b are no longer valid. Eventually, every state will become high field seeking, since a low lying state has many states of higher J above it [70]. Therefore, a solution at high field strengths can only be obtained by full diagonalization of the Hamiltonian, as shown in [65]. The Stark shift of SrF $X^2\Sigma^+$ in the vibrational ground state is shown in Figure 2.7, which is obtained using the spectrum simulation program PGHOPER [20]. For the LFS $N = 1, M = 0$ and $N = 2, M = 0$ states, the aforementioned change from quadratic to linear occurs around 5kV/cm and 20kV/cm, respectively.

The obtained knowledge on the LFS and HFS character of certain states of SrF and BaF is subsequently used to create potentials wells inside the traveling-wave Stark decelerator.

A controllable moving electric field trap

The traveling-wave Stark decelerator, henceforth referred to as the decelerator, uses a time-varying high voltage electric field applied to ring-shaped electrodes to create a moving three dimensional trapping potential for molecules in a low field seeking state. By reducing the velocity of the traps in which the molecules are confined, the velocity of the molecules that remain trapped is reduced as well. Using this approach, relatively fast molecular beams (300 - 1000 m/s) can be slowed down to a much lower forward velocity (50 - 150 m/s) [71]. Recently, the decelerator has even been used to decelerate molecules to zero velocity and keep them trapped for up to 50 ms [64].

The decelerator currently consists of 9 modules holding 8 rods with 42 rings each spaced 12 mm apart, totalling 3024 rings over 4536 mm [66]. Each ring has an inner diameter of 4 mm, a thickness of 0.6 mm and every 9th ring is connected to the same electrode. All modules are contained in vacuum chambers and kept at $\sim 10^{-8}$mbar. More details on the construction of the decelerator can be found in [65]. Figure 2.8 shows a 3D model of a single decelerator module and a zoomed in view of the rings.

A sinusoidally varying voltage of the form $V_n(t) = V_0 \sin(-\phi(t) + 2\pi n/8)$ is applied on the 8 electrodes to create the moving traps, with the voltage phase difference between consecutive electrodes equal to

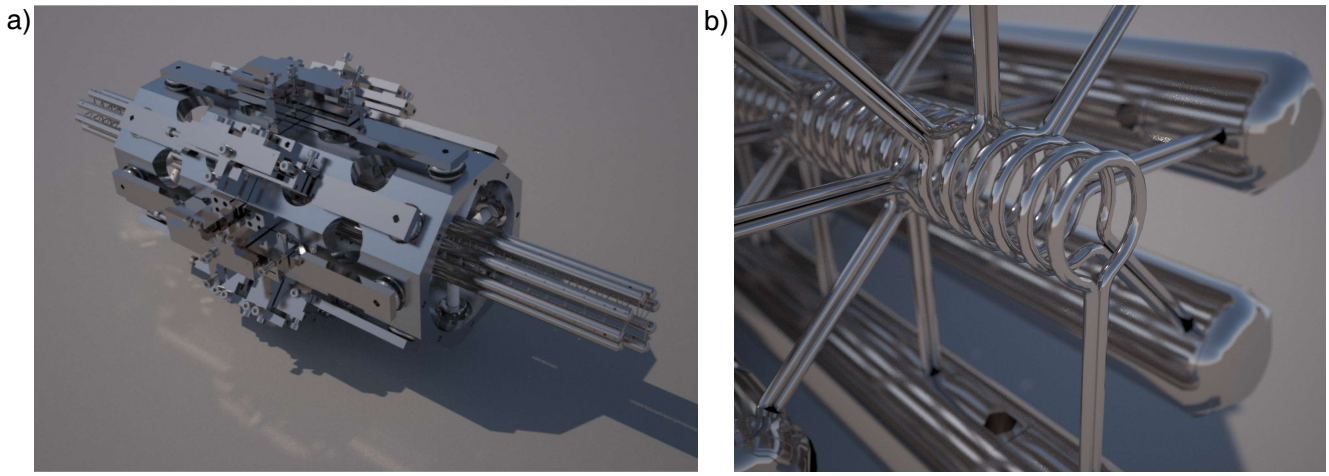

FIGURE 2.8: **a)** 3D render of a single decelerator module. **b)** Magnified image of ring electrodes at the end of a module. Both renders were created by Steven Hoekstra.

$2\pi/8$. The decelerator is usually operated in either constant velocity (ac-guiding)[1] or in constant deceleration mode. The propagation velocity of the traps is determined by the oscillation frequency of the potential applied to electrode number n [66]:

$$V_n^g(t) = V_a \sin\left(-\frac{2\pi v_0}{T}t + \frac{2\pi n}{8}\right) \qquad \text{constant velocity} \tag{2.5a}$$

$$V_n^d(t) = V_a \sin\left(\frac{-2\pi}{T}\left(v_i t - a\frac{t^2}{2}\right) + \frac{2\pi n}{8}\right) \qquad \text{constant deceleration} \tag{2.5b}$$

Where $V_n(t)$ denotes the voltage amplitude, v_0 the constant velocity in guiding mode, T the period of the applied voltage and L the length of the decelerator. The constant deceleration strength a from initial velocity v_i to final velocity v_f is introduced through $a = (v_i^2 - v_f^2)/2L$. Compared to the linear $\phi(t)$ variation required to obtain traps moving at a constant velocity, deceleration requires a gradual chirp of the frequency of the sine wave. The sinusoidal voltage applied to achieve the strongest ($\phi = 0$) and weakest ($\phi = \pi/8$) confinement in the radial direction for an applied voltage amplitude of 5 kV is shown in Figure 2.9.

The waveforms described in equations 2.5a and 2.5b are created with a fictitious 'synchronous molecule' in mind. The electric field on the first ring switches on when the synchronous molecule enters the decelerator, with a velocity assumed to be exactly v_i upon entering [73]. Similarly, the voltage waveform is turned off when the synchronous molecule exits the last ring with a velocity v_f. When the waveform is switched on and off, a ramp-up or ramp-down time has to be taken into account, as the amplifiers cannot deliver a high voltage instantaneously. The synchronous molecule is assumed to be located exactly in the center of it's corresponding potential trap. Alternatively, the traps can be thought of as moving with the speed of the synchronous molecule.

A strong confining force requires a large energy difference between the center and edge of the trap. Maximizing the restoring force experienced by the LFS molecules is achieved by maximizing the electric field gradient, which depends on the inner diameter of each ring as well as the applied electric field. As the diameter of each ring is fixed, the only remaining variable is the applied electric field. As shown in Figure 2.7, the total energy difference due to the Stark shift for the LFS part of the $v = 0, N = 2, M = 0$

[1] dc-guiding mode uses a static voltage to create a potential that is only confining in the radial direction [72].

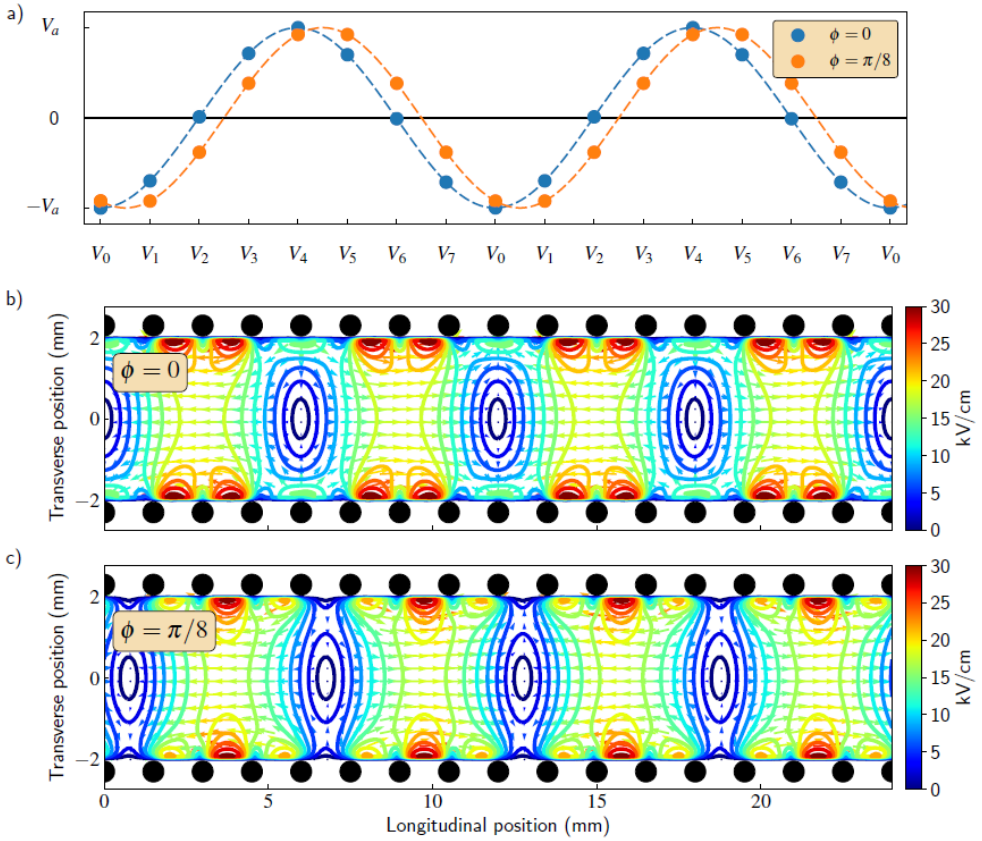

FIGURE 2.9: **a)** The voltages V_n on electrode n for two different phases of the sine wave. The phases $\phi = 0, \pi/8$ are chosen since they represent the largest and smallest confining potential, respectively. Electrode locations are marked by a dot. **b, c)** Contour lines of constant electric field inside the decelerator rings show the potential minima structure. The voltages used to generate these traps corresponds to those shown in part **a** of the figure. The trapping potential experienced by the molecules can be obtained by convolution of the electric field and the Stark shift of a particular state. Figure from [66].

is larger compared to that of the $v = 0, N = 1, M = 0$ state. Therefore, a logical start would be to attempt deceleration in the $N = 2$ state. As can be inferred from Figure 2.7, this means that the electric field is required to be on the order of $\sim$ 60kV/cm. However, there are technical limitations on the amplifiers used to generate the oscillating voltage, such as for instance the combined requirements of the maximum maintained voltage amplitude, repetition rate, bandwidth during the deceleration period, capacitive load and sweeping from tens of kHz to DC in $\sim$ 50 ms [66]. This means that the amplifiers are currently constrained to a voltage amplitude of 5 kV, corresponding to a maximum electric field of 21 kV/cm. Therefore, deceleration results are currently obtained using molecules in the $N = 1$ state. Previous simulations on the total 3D phase space acceptance of the decelerator suggest that, for equal initial populations in the $N = 1$ and $N = 2$ state, deceleration at a voltage amplitude of 10 kV of 20kV$_{pp}$ will result in a factor 2 increase in the amount of trapped molecules in the $N = 2$ state compared to the $N = 1$ state [66][65].

To illustrate the versatility and lossless nature of the moving potential traps, recent work has shown the decelerator to be capable of decelerating molecules to standstill ínside the decelerator, holding them in their trap for up to 50 ms, and accelerating the packets out again [64].

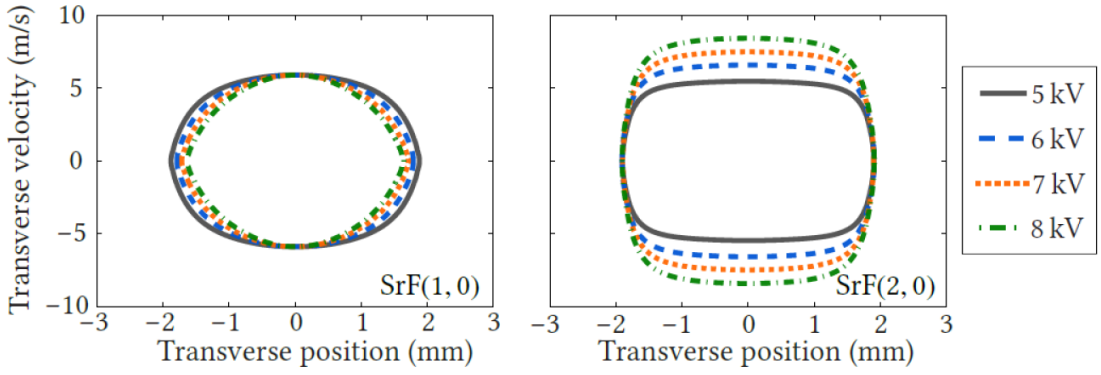

FIGURE 2.10: Transverse phase space acceptance of the traveling-wave Stark decelerator for two LFS SrF(N,M) states for ac-guiding at four different voltage amplitudes [65].

Phase space acceptance and stability

To assess the performance that can be expected from traveling wave Stark deceleration of heavy diatomic molecules in a low field seeking state, a series of phase space simulations have been conducted [65][66]. A phase space diagram can provide valuable information on the maximum velocity and radial position a molecule should have, relative to the synchronous molecule, in order to remain trapped. The area within the separatrix is dubbed the phase space acceptance, and stable deceleration only occurs for molecules located in this region. During the deceleration process, the phase space density of the molecules located in the phase space acceptance is kept constant, and the molecules in each trap will oscillate around the synchronous molecule [73].

Simulation results on the transverse 1D phase space acceptance of the decelerator are shown in Figure 2.10. For SrF(1,0) and the current decelerator geometry, the LFS to HFS turning point is reached for roughly 5 kV. Therefore, a higher voltage amplitude only acts to spatially compress the trap by introducing a HFS region near the ring edges, leading to a smaller phase space acceptance. For SrF(2,0), the voltage amplitude can be increased up to $\sim$ 10 kV until this turning point is reached. Therefore, increasing the voltage amplitude from 5 kV to 8 kV increases the depth of the potential experienced by the molecules. Operating at deceleration instead of ac-guiding also decreases the phase space acceptance, due to the decrease in potential depth [65]. To summarize, the magnitude of the phase space acceptance is determined by the geometry of the successive ring electrodes, the deceleration strength of the waveform, the electric field strength and the Stark curve of the subject molecules. The shape of the separatrix is important for the phase space matching described in Chapter 3.

2.3.2 A cryogenic buffer gas source of molecular beams

The proposed NL-eEDM experiment requires a slow, cold and intense molecular beam. Previously, deceleration results were obtained using a supersonic beam obtained from the expansion of a carrier gas from an Even–Lavie valve in combination with a laser ablated metal target [74][75]. A supersonic expansion cools the rotational and vibrational degrees of freedom of a molecular beam, to produce velocity distributions with a temperature on the order of 1 K [76]. However, the relatively large forward velocity of such a supersonic expansion beam means that a high deceleration strength is required in order to remove a significant amount of kinetic energy in a Stark decelerator of realistic dimensions. Therefore, a cryogenic buffer gas source of molecular beams has been developed [20][77][78].

Compared to the supersonic expansion technique, molecular beams created using a cryogenic buffer gas approach benefit from both an increased intensity and a lower average velocity, yielding 10^{10} molecules per pulse per steradian at $\sim$ 190m/s compared to 10^8 at $\sim$ 600m/s [79]. However, their velocity spread

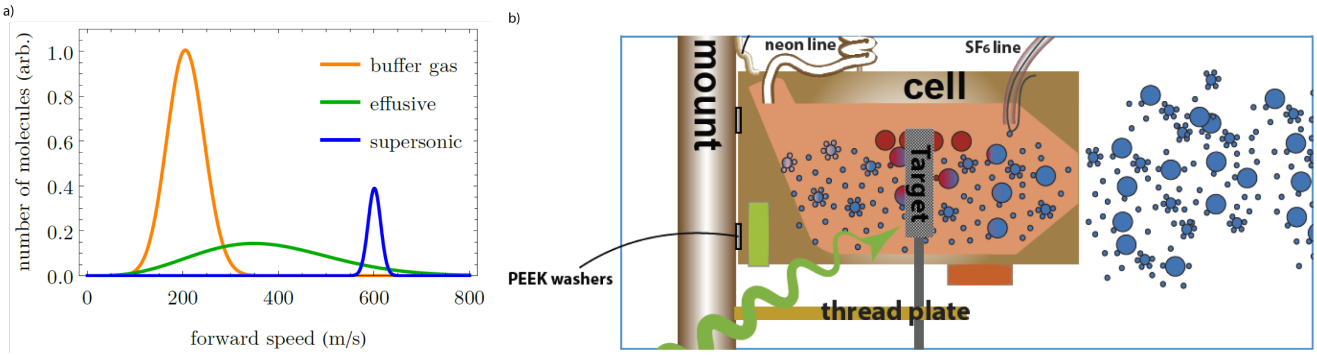

FIGURE 2.11: **a)** Figure of merit comparison of velocity distributions for buffer gas cooled, effusive and supersonic beam sources. The high intensity of the buffer gas beam is indicated through the large integral of it's distribution [62]. **b)** Schematic description of molecular beam formation inside the cryogenic cell [20].

is usually larger, as shown in Figure 2.11a. As the decelerator can generate multiple potential traps spaced 6 mm apart [66], the increased velocity spread simply fills a larger amount of potential traps which are decelerated in parallel. However, a larger velocity spread also enhances the distortion of the phase space distribution as the beam experiences free flight propagation. This distortion will be further discussed in Section 3.2.

A detailed description of the cryogenic buffer gas source which is currently in use can be found in [20]. Figure 2.11b shows a schematic description of molecular beam formation inside the cryogenic cell. Inside the cell, a rotating solid Sr target is ablated using a 3-6 mJ, 5 ns laser pulse from a INLITE II-20 Nd:YAG laser at 532 nm with a repetition rate of 10 Hz. SF_6 gas is injected at a rate of 0.5 sccm and reacts with the ablation products to form SrF, which is subsequently cooled inside a two-stage pulse tube cryocooler using liquid helium. The warm, outer stage is kept at $\sim$ 25K and the cold, inner stage at $\sim$ 4K. The cell is attached to the inner stage and kept at 17K using a heater. The pressure outside of the cell is kept at $\sim 10^{-8}$mbar. The internal and motional degrees of freedom of the SrF molecules thermalize due repeated collisions with the background buffer gas, in this case ^{4}Ne injected at a rate of 8 sccm and a temperature of 17 K. Finally, a beam of $\sim 10^9$ (or $\sim 10^{10}$ sr^{-1}) SrF molecules per shot in the $X^2\Sigma^+(v = 0, N = 1, M = 0)$ state is created as the molecules exit the cell through an orifice. The molecules are detected 5 mm away from the orifice by observing absorption on the strong transition described in subsection 2.3.3, using a photodiode. When operated using standard settings, the source produces a molecular beam with a longitudinal velocity of 190 ± 50 m/s in a pulse of 5-10 ms, with transverse velocity spread of $\pm$ 30 m/s and a rotational temperature of 11 K [80].

2.3.3 Laser induced fluorescence detection

Typical energy level transitions within a diatomic molecule can be electronic, vibrational or rotational of nature, listed in order of decreasing energy difference. Light collected from such a transition can be used to infer the presence of a molecule. In order to detect the SrF molecules at the exit of the decelerator, a laser induced fluorescence (LIF) scheme is used. LIF detection requires a stable source of light at the relevant wavelength(s), such that molecules will reliably scatter light. To this end, the strong one-photon electronic transition $A^2\Pi_{1/2}(v' = 0, J = 1/2) \rightarrow X^2\Sigma^+(v' = 0, N = 1)$, shown in Figure 2.12, is used for both the absorption and LIF detection. The highly diagonal Franck-Condon factors (FCFs) between sublevels of these two states indicate very little spontaneous decay to dark, excited vibrational states [81], and create efficient detection conditions and even allow for repeated optical cycling [82]. The interaction of the nuclear spin $I_F = 1/2$ of the ^{19}F atom with the total angular momentum excluding spin J is responsible for the creation of the hyperfine structure: $F = I + J$. The hyperfine interaction creates 4 substates in the $X^2\Sigma^+(v' = 0, N = 1)$ state. These substates can create loss channels in the

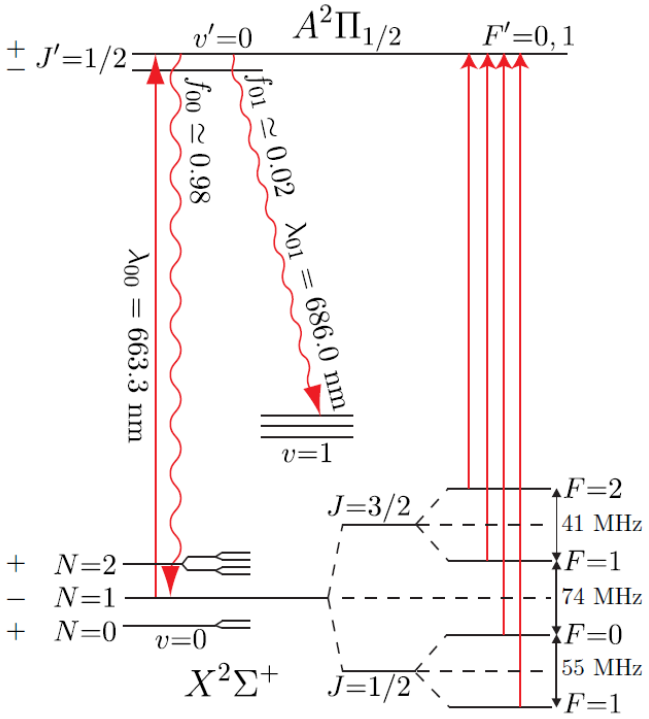

FIGURE 2.12: Energy level structure of the $A^2\Pi_{1/2}(v' = 0, J = 1/2) \rightarrow X^2\Sigma^+(v' = 0, N = 1)$ transition, including relevant Franck-Condon factors f_{xx}, transition wavelengths and hyperfine structure of the $N = 1$ state [66]. The hyperfine splitting of the $A^2\Pi_{1/2}$ state is < 3 MHz and is therefore unresolved [83].

detection scheme if they are not addressed.

The optical infrastructure used to generate the necessary wavelengths is shown in Figure 2.13. Laser light at a wavelength of 663.3 nm is generated by a home-built external cavity diode laser[2], dubbed the master laser, which controlled by a diode laser controller[3]. Part of the emitted beam is split off towards a wavelength meter and the first scannable Fabry-Perot cavity[4], dubbed the laserlocker cavity. Light from a commerically available HeNe laser[5] is coupled into the laserlocker cavity and serves as a stable reference. The frequency mode spectrum of the input lasers is obtained using the cavity. By monitoring the frequency difference between the diode and HeNe laser and establishing a current feedback loop, a linewidth of 1 MHz of the detection laser sent to the experiment is achieved [66][20].

The part of the beam not sent to the laserlocker cavity is sent through an EOM[6], to which a sinusoidal voltage with a frequency of 42.5MHz, a voltage amplitude of 600 mV and a duty cycle of 50% is supplied. With these settings, the EOM creates a phase modulation that largely divides the power of the input beam over four equally frequency-spaced sidebands that best match the aforementioned hyperfine structure [84]. The light is then coupled into a second diode laser, dubbed the slave laser, which uses optical feedback to increase the power allocated to the sidebands. A tapered amplifier[7] further increases the power. Next, the light is divided between another cavity and two optical fibers, one for absorption detection and one for LIF detection. The cavity is used to monitor if sideband creation and optical feedback to the slave laser occur successfully. In standard operating conditions, the current applied to

[2]Opnext Hitachi HL6545MG
[3]Moglabs, DLC-202
[4]Thorlabs SA200-5B, 632.991 nm
[5]Thorlabs HRS015B, specified stability 1 MHz drift over 60 minutes.
[6]JENOPTIK PM660
[7]Toptica BoosTA

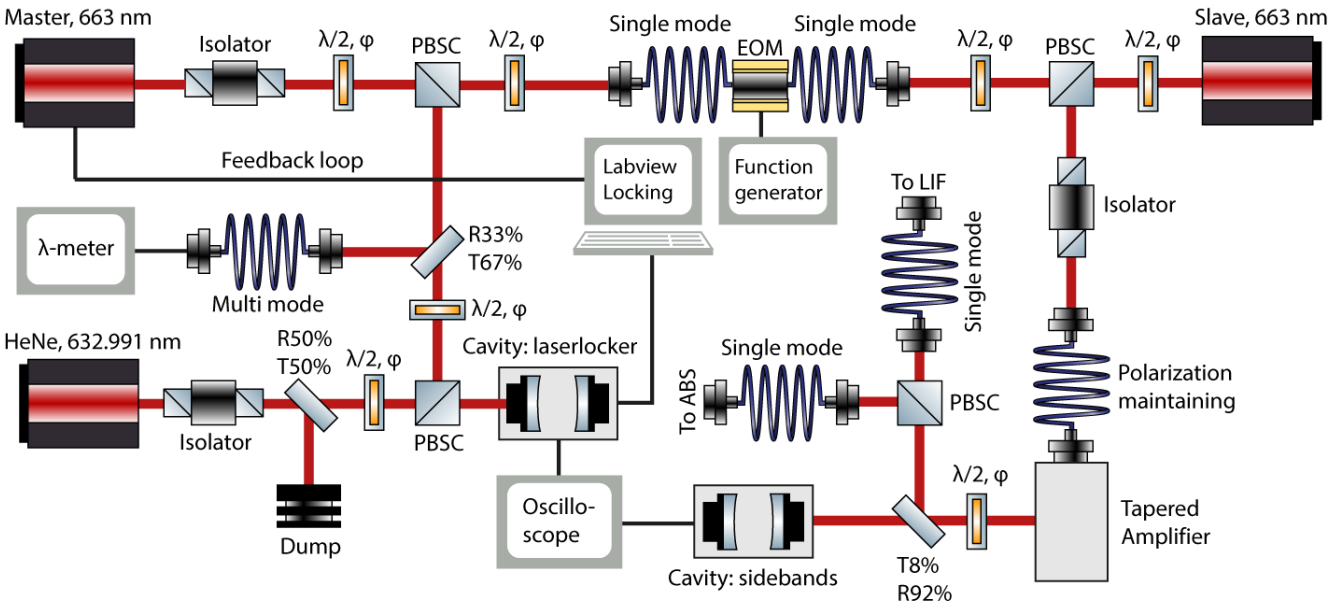

FIGURE 2.13: Optical setup used for generating the laser light required for addressing the transition pictured in Figure 2.12. Some elements can be rotated through an angle ϕ to alter their transmission.

the master laser is varied such that the wavelength meter measures 15076.22 cm^{-1} (corresponding to 663.2962 nm), after which the laser lock is engaged.

Outside of the vacuum chamber housing the exit of the decelerator, the LIF detection laser is collimated into a beam with a diameter of 0.7 mm and a power of 0.5 mW. The detection laser crosses the molecular beam ∼10 mm after the molecules exit the last ring of the decelerator, as shown in Figure 2.5. Molecules are excited on the $A^2\Pi_{1/2}(v' = 0, J = 1/2) \rightarrow X^2\Sigma^+(v' = 0, N = 1)$ transition and their fluorescence is collected by a combination of lenses, with a collection solid angle of 0.93 steradian and a collection efficiency of 7.5%, and imaged onto a PMT[8] with a quantum efficiency of 40%. With a magnification factor of 2.7, the 5mm by 5 mm effective area leads to a 1.9 by 1.9 mm from which scattered light can be collected.

The resulting time-dependent photon counts are converted into a time-of-flight (TOF) profile by making a histogram with respect to their arrival time. A number of typical deceleration measurements obtained before the hexapole was installed are shown in Figure 2.14 [64]. The zoomed view of the constant velocity ac-guiding operation mode shown in Figure 2.14b illustrates that the decelerator selects a central part of the beam and fills ∼ 16 potential traps spaced 6 mm apart. Figure 2.14c shows the potential trap signature for deceleration to lower velocities. The decrease in signal intensity is attributed to both a decrease in longitudinal and transverse acceptance of the decelerator for an increasing deceleration strength, and an increase in divergence of the beam at lower velocities, as the transverse velocity of the molecules does not significantly change during deceleration.

2.3.4 Increasing the number of decelerated molecules

The low rotational temperature of the cryogenic molecular beam ensures that the molecules are mainly located in the lower rotational states. The fraction of molecules that occupy the low field seeking $X^2\Sigma^+(v' = 0, N = 1)$, compared to other high field seeking states, will determine the amount of molecules that can be decelerated per ablation shot. Of these molecules, a fraction of $1.5 \cdot 10^{-6}$ have a position and velocity that falls within the acceptance of the decelerator [64]. Apart from switching to

[8] Hamamatsu H7422p-40

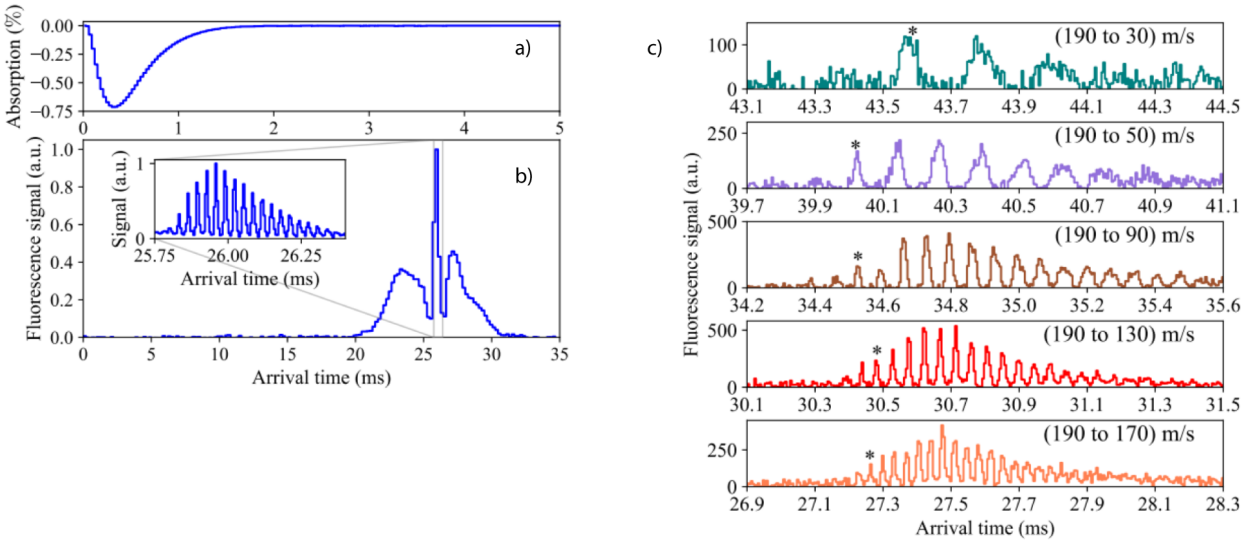

FIGURE 2.14: Typical absorption and fluorescence time-of-flight signals obtained from deceleration and acguiding of a molecular beam, where $t = 0$ corresponds to the time at which the Nd:YAG laser ablates the target and * denotes the synchronous molecule. **a)** From the peak in the absorption signal, it is estimated that molecules on average take 300 µs to exit the cell. **b)** The experimental time-of-flight profile using a binsize of 200 µs shows the guiding through the decelerator of the SrF molecular beam with an average velocity of 190 m/s at 5.0 kV. Inset: a zoom-in of the guided peak with a binsize of 5 µs, which shows the repeated electric field trap structure. **c)** Zoom in of the time-of-flight histograms around the arrival time of the decelerated peaks with a binsize of 5µs. Figures adapted from [64].

higher voltage amplitudes, increasing the number of decelerated molecules can be done by for instance optical pumping into low field seeking states, or by increasing the aforementioned fraction through better phase space matching between the source and decelerator (Chapter 3).

Optical pumping to low field seeking states

The hyperfine interaction is not only responsible for creating a substructure in the $A^2\Pi_{1/2}(v' = 0, J = 1/2) \rightarrow X^2\Sigma^+(v' = 0, N = 1)$ transition, as shown in Figure 2.12, but also influences the efficiency of the decelerator. Figure 2.15 shows the Stark shift at relatively low field strengths of the hyperfine substates of the low field seeking $X^2\Sigma^+(v' = 0, N = 1)$ rotational state. Each hyperfine substate has a low field- or high field seeking character, and transitions from low to high field seeking states can cause molecules to escape the moving potential generated by the decelerator. Previous work contains an experimental and simulated investigation of the possibility to increase the fraction of low-field seeking molecules by optical pumping between hyperfine states [72]. In this work, the pump laser beam transversely crossed the molecular beam 12 cm downstream from the entrance of the decelerator, in between two rings. This approach yielded an increase in the number of low field seeking molecules of at most 50%.

An alternative approach is to optically pump molecules into low field seeking states before they enter the decelerator. Currently, this would involve constructing a pumping scheme to deliver molecules into the $X^2\Sigma^+(v' = 0, N = 1)$ state, taking into account the relevant transition rules. A similar procedure was used to improve the statistical sensitivity of the YbF eEDM experiment, which yielded an order-of-magnitude increase in the number of molecules that could participate in the eEDM experiment [60]. There, the population in (N, F) = (0, 1), (2, 1), and both (2, 2) states is optically pumped into (0, 0) via the odd-parity $J' = 1/2$ state.

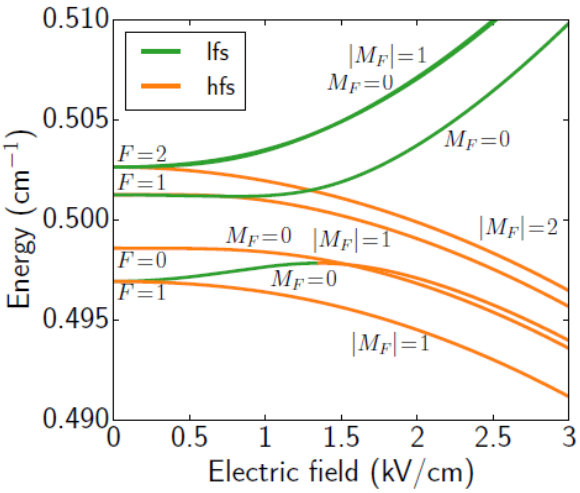

FIGURE 2.15: Low field magnification of the Stark shift in the hyperfine levels (F, m_F) of the $X^2\Sigma^+(v' = 0, N = 1)$ state shown in Figure 2.7. Crossings indicate that only a low field strength is required to induce state transitions and thereby mixing of the levels. Figure from [66].

2.4 Conclusion

This chapter introduces the context of eEDM experiments and the framework within this project was conducted. A brief overview of the experiment proposed by the NL-eEDM is given, with a focus on the elements that are currently used to create and detect the slow molecular beam.

Chapter 3

Improving the transfer of molecules using an electrostatic hexapole

After the extensive control of the velocity of the molecular beam was demonstrated in [64], the focus will shift towards increasing the number of decelerated particles per ablation shot. Increasing the number of decelerated molecules is a necessary step towards a competitive measurement of the eEDM. A maximal number of decelerated particles is obtained when the phase space distribution of the input molecular beam perfectly overlaps with the phase space acceptance of the decelerator [85]. This chapter describes the work conducted to design, create, implement and test an electrostatic hexapole such that an optimal phase space matching is achieved, which translates to an increase in the intensity of the decelerated beam. Finally, a possible estimate of the factor increase in the detected number of molecules which can be attributed to implementation of the hexapole is discussed.

3.1 Motivation and objective

With the goal of efficient deceleration in mind, the phase space acceptance of the traveling-wave Stark decelerator places strict constraints on the phase space distribution of the input molecular beam. In an ideal world, every molecule emitted by the cryogenic source will enter the decelerator. The orifice of the source is designed such that it features an emittance that fully overlaps the phase space acceptance of the decelerator. Furthermore, the voltage waveform applied to the decelerator is optimized to the velocity distribution of the molecular beam. However, real world restrictions such as the multiple thermal shields needed for the source, vacuum chamber dimensions, close couplers and a valve introduce unwanted free flight propagation and thereby change the phase space distribution of the beam. The divergence of the molecular beam during free flight from the source to the decelerator is illustrated in Figure 3.1. A simple calculation is enough to show the impact of several milliseconds of free flight. In Table 6.3 in [80], it is estimated that the initial transverse spread of the molecules is restricted to $\pm$ 0.5 mm. A molecular beam with a velocity of 190 m/s takes 1.95 ms of free flight to cover the 369 mm between the cell exit and the decelerator. However, a transverse velocity of $v_t = 0.25$ m/s is enough to spread out 0.5 mm in the radial direction during this free flight. As the molecular beam emitted by the source has a transverse velocity spread of 60 m/s, a large number of molecules will have a transverse velocity in excess of 0.25 m/s, and consequently falls outside of the phase space acceptance of the decelerator, even though the transverse velocity acceptance of the decelerator is calculated to be $\pm$ 5 m/s [65]. The discrepancy between these two number illustrates a significant underfilling of the phase space acceptance of the decelerator.

The phase space acceptance of the decelerator is largest when it is operated at a constant velocity, or ac-guiding. As the deceleration strength increases, the phase space acceptance of the decelerator decreases. in both the longitudinal and transverse directions [65]. Therefore, it is important to maximally fill the transverse phase space acceptance for the ac-guiding operation mode, in order to ensure improved filling of the transverse phase space acceptance when decelerating to 30 m/s, the velocity required for the

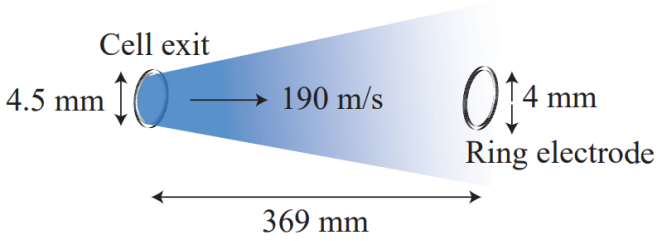

FIGURE 3.1: Divergence of the molecular beam during free flight from the cryogenic source to decelerator, before installation of the hexapole [80].

final eEDM experiment. This chapter describes the work conducted to achieve optimal phase space matching using an electrostatic hexapole, which acts as a focusing lens.

3.2 Designing an electrostatic lens

For the better part of five decades, the unique focusing properties of electrostatic multipoles have provided many experimental phycisists with the tools required to control and manipulate molecular beams [86]. The ideal electric deflection field used to create a lens will exert a strong, constant force in one direction, while the force in the perpendicular direction is zero [71]. Monitoring the evolution of the phase space distribution is a useful tool to assess the functionality of such a lens.

A magnetic analogue to an electrostatic lens also exists, which uses the Zeeman effect to achieve transverse focusing of a molecular beam [87]. Compared to focusing achieved using electric fields, magnetic fields offer many technical challenges [88]. Two examples are the increased rise and fall time of the magnetic field compared to an electric field and the Ohmic heating owing due to the application of very high currents [71]. The molecular beam source used in this project is designed for a decelerator that uses the low electric field seeking states. Therefore, implementing a magnetic lens would introduce added complexity by requiring optical pumping to states that are low magnetic field seeking before the beam enters the lens, and pumping to low electric field seeking states after the beam exits the lens. A magnetic field can also be used to force the dark states, which are not coupled to the fluorescence detection scheme, to Larmor precess into bright states [84].

3.2.1 Phase space matching

The phase space distribution is commonly used to characterize the width and angular divergence of a particle beam [89]. The process of Stark deceleration can be envisioned as isolating a predetermined packet with a narrow spatial and velocity distribution, and translating this packet to lower velocities [90]. When connecting multiple elements of a beamline, one has to make sure that the phase space density remains constant during propagation through the machine, to avoid unnecessary losses of molecules. Important to note is that the phase space density remains constant throughout deceleration: a direct consequence of Liouville's theorem [91]. The phase space density will be defined during creation of the molecular beam and will not increase throughout the beamline. However, when a group of molecules is transferred from one element to the next and these elements are not properly matched, the density will dilute or decrease [71]. In general, optimal phase space matching is achieved when the distribution of a molecular packet fully overlaps with the acceptance of the beamline element it enters.

The phase space distribution of the molecular beam characterizes the longitudinal and transverse position and velocity spreads of the beam, providing four parameters with an influence on the number of

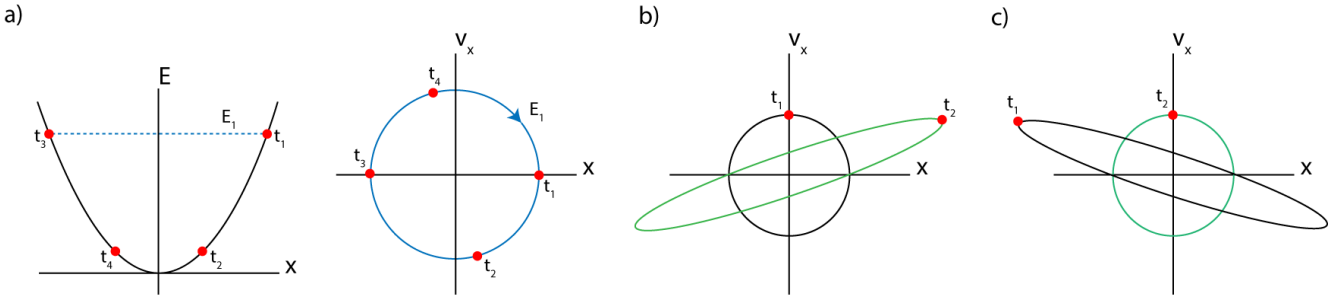

FIGURE 3.2: Perfect lensing illustrated through manipulation of the phase space distribution using a harmonic potential (blue) and free flight (green). **a)** The restoring force in a harmonic potential effectively rotates an initial distribution without changing it's shape. **b)** Free flight from t_1 to t_2 acts to skew the distribution. In this diagram, the particle will move in a straight line to the right between t_1 and t_2. According to Liouville's theorem, the area enclosed by the circle and ellipse are equal. **c)** After propagation through a harmonic potential has rotated the distribution (black), additional free flight from t_1 to t_2 allows for obtaining the original distribution emitted by the source.

molecules that can be decelerated. The transverse component of the molecular beam's velocity distribution is of main importance in obtaining improved phase space matching between the source and decelerator, since many different potential traps inside the decelerator can be filled in parallel, but molecules still have to fall within the transverse position and velocity acceptance, owing to the dimensions of the rings and the applied voltages, respectively. During free flight, there is no force acting on the molecules and the beam will diverge. If a refocusing element is placed downstream from the source, the divergent nature of the beam can be corrected to converge into the next element, analogous to a biconvex lens in ray optics.

Creating a perfect lens

Optimal imaging of the phase space distribution from one element to the next can be achieved using a perfect lens. The effect of a perfect lens on the evolution of a phase space distribution is shown in Figure 3.2. If a perfectly harmonic focusing element is located between two sections of free flight equal in length, the entire phase space area of the input beam originating from a point source can be imaged onto the acceptance of the next element. A perfect lens requires a fully harmonic potential. As molecules oscillate in such a potential, they will trace out a circle in phase space. Therefore, a harmonic potential does not change the shape of a distribution and only rotates it uniformly. Alternatively, a section of free flight will stretch and slightly tilt the distribution, increasing the position spread but keeping the velocity spread constant. Particles with a relatively large velocity will move away from the center of the distribution quicker than those with a relatively small velocity. During this process, the area of the phase space distribution remains constant [92]. During free flight, the distribution cannot rotate more than 90 degrees, as this would indicate an infinite position spread.

Various phenomena can inhibit the creation of a truly perfect lens, and lead to for instance a soft focus. Beam sources will always have a certain aperture size, compared to perfect point sources, which makes it near impossible to focus the beam to an area smaller than the aperture size. Furthermore, the potential might not be purely harmonic, creating a nonlinear force at certain radial distances inside the lens. An anharmonic potential will change the focus from a sharp point to a ring, an effect similar to that of spherical abberation in optical lenses [71]. Such blurring of the focus is illustrated in Figure 3.3.

3.2.2 Using the Stark shift to create an electrostatic lens

The same electric field dependent energy level shift used to create traveling potential traps of the decelerator can also be employed for additional focusing or deflection of the molecular beam [95]. Of main

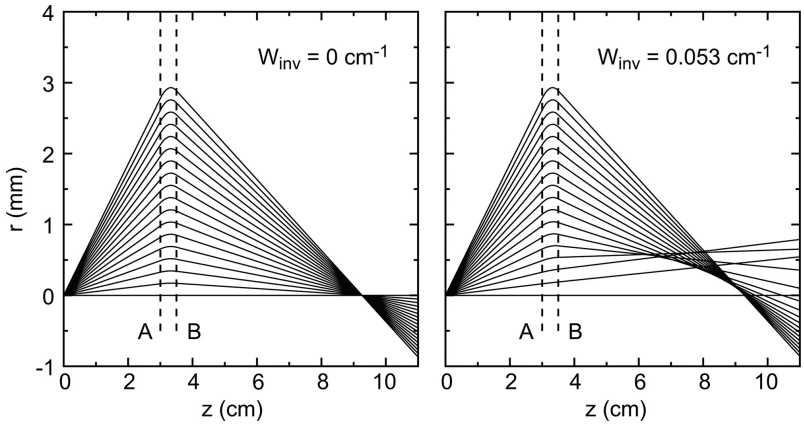

FIGURE 3.3: The trajectories of low electric field seeking ND_3 molecules originating from a single point, which are refocused using an electrostatic hexapole (lenght A to B), show blurring of the focus due to anharmonicity in the refocusing potential. Without inversion splitting, the force experienced by the molecules inside the hexapole is perfectly linear [93], corresponding to a perfect lens. With inversion splitting included, the refocusing force close at small radial distances becomes nonlinear. One possible method of correcting for such nonlinearities is placing quadrupole and hexapole fields in series [94]. Figure from [71].

interest for this work is transverse collimation and focusing, which for polar molecules in low-field seeking states can be achieved by using electrostatic lenses, e.g., quadrupole or hexapole lenses [90]. This section will discuss the requirements on the electric field and Stark shift necessary to create such a focusing lens.

Characterizing the electrostatic field of a multipole lens

The following description of the electrostatic multipole focusing of a molecular beam is obtained from [71] and [96]. Any axially symmetric electrostatic field must satisfy the Laplace equation [97]. In two dimensions, a general solution to the Laplace equation $\nabla^2\Phi = 0$ may be expressed as a multipole expansion:

$$\Phi(r,\theta) = \Phi_0\left[\sum_{n=1}^{\infty}\frac{a_n}{n}\left(\frac{r}{r_0}\right)^n\cos(n\theta) + \sum_{n=1}^{\infty}\frac{b_n}{n}\left(\frac{r}{r_0}\right)^n\sin(n\theta)\right] \tag{3.1}$$

Where r_0 denotes the radius of the electric field. The $n = 2$ and $n = 3$ terms represent quadrupole and hexapole fields, respectively. By omitting all other multipole contributions other than the pure n=1,2,3, the above simplifies to:

$$\Phi(x,y) = \Phi_0\left[a_1\frac{x}{r_0} + a_2\frac{(x^2-y^2)}{2r_0^2} + a_3\frac{(x^3-3xy^2)}{3r_0^3}\right] \tag{3.2}$$

A pure quadrupole or hexapole field can be obtained by setting all coefficients but a_2 or a_3, respectively, to zero:

$$\Phi_q(x,y) = \Phi_0\left(a_2\frac{(x^2-y^2)}{2r_0^2}\right) \rightarrow E_q(r,\theta) = \Phi_0\frac{a_2}{r_0^2}r \qquad \text{quadrupole} \tag{3.3a}$$

$$\Phi_h(x,y) = \Phi_0\left(a_2\frac{(x^3-3xy^2)}{3r_0^3}\right) \rightarrow E_h(r,\theta) = \Phi_0\frac{a_3}{r_0^3}r^2 \qquad \text{hexapole} \tag{3.3b}$$

The restoring force due to the change in Stark energy is defined as follows:

$$\vec{F}(r) = -\nabla W_{Stark}(r) \tag{3.4}$$

A perfect lens requires a harmonic potential or linear force. This places the following constraints on the electric field:

$$\nabla W_S(r) \propto E \rightarrow \vec{F}(r) = -\nabla(E(r,\theta)) \qquad \text{linear Stark shift} \tag{3.5a}$$

$$\nabla W_S(r) \propto E^2 \rightarrow \vec{F}(r) = -\nabla(E(r,\theta)^2) \qquad \text{quadratic Stark shift} \tag{3.5b}$$

A quadrupole field is constructed using four electrode rods with alternating polarity. The ideal hexapole field however, consists of six hyperbolic electrodes with alternating polarity, located on the corners of a hexagon. As the high voltages commonly applied to such hexapoles would lead to discharges, hyperbolic electrodes are unfeasible. The best approximation is obtained using circular electrode rods with a radius of $R = 0.565 r_0$ [96].

Equations 3.3a and 3.3b show that in order to obtain a linear restoring force, a linear Stark shift requires an electric field that varies quadratically away from the center, which can be obtained using the hexapole field. Similarly, a quadratic Stark shift requires a linear electric field, obtained using a quadrupole field. The next step is to determine the shape of the Stark curve at relevant field strengths, to decide which multipole field will produce an optimal lensing effect.

3.2.3 Simulations on phase space trajectories

In order to gain a deeper understanding of the changes in the measured number of decelerated molecules that can be obtained by implementing an electrostatic hexapole or quadrupole, a number of phase space simulations were conducted. The code of these simulations was written by Hendrick Bethlem.

Description of the simulations

The code is based on tracking the position, velocity and 'hit status' of molecules propagating through the setup. The code models the effect of freeflight, the hexapole and the decelerator on an initial phase space distribution. If the position of a molecule exceeds the dimensions of the setup, i.e. an impact with for instance the hexapole rods occurs, the 'hit status' is changed to false. The trajectories inside the hexapole can be modeled by calculating the acceleration experienced by the SrF/BaF molecules as they traverse through the hexapole, based on a numerical approximation of the derivative and on the full expressions of the electrostatic potential shown in equations 3.3a and 3.3b. Relevant input parameters for the simulations are an electric dipole moment of $\vec{\mu}_e = 3.170(3)$D [98][99], rotational constant $B = 0.21594802$ [100], the phase space acceptance of the decelerator, and the dimensions of the detection zone.

The transverse acceptance is approximated as a circle in phase space, with maximum values x_{acc} and $v_{x,acc}$. The detection volume is approximated as the two-dimensional overlap between the transverse dimensions of the molecular beam and the LIF detection laser, with the width of the LIF detection beam parallel to the molecular beam propagation direction not taken into account. The molecules are considered 'detected' if they successfully make it to this area and have a true 'hit status'. In the vertical direction, the size of the detection area is limited by the diameter of the LIF detection laser. In the horizontal direction, the size of the detection area is limited to 1.9 mm, due to the magnification factor from the fluorescence light collection system ($M = 2.7$ [80]) and the active area of the PMT (5x5 mm).

Characterizing the Stark shift of BaF and SrF

The Stark curves for the $X^2\Sigma^+(v' = 0, N = 1)$ state are obtained from PGOPHER. Next, a parametrization was created by Hendrick Bethlem to approximate these curve at an electric field strength between 0 and 20 kV/cm. At low electric field strengths, between roughly 0 and 5 kV/cm, the Stark shift W_S can

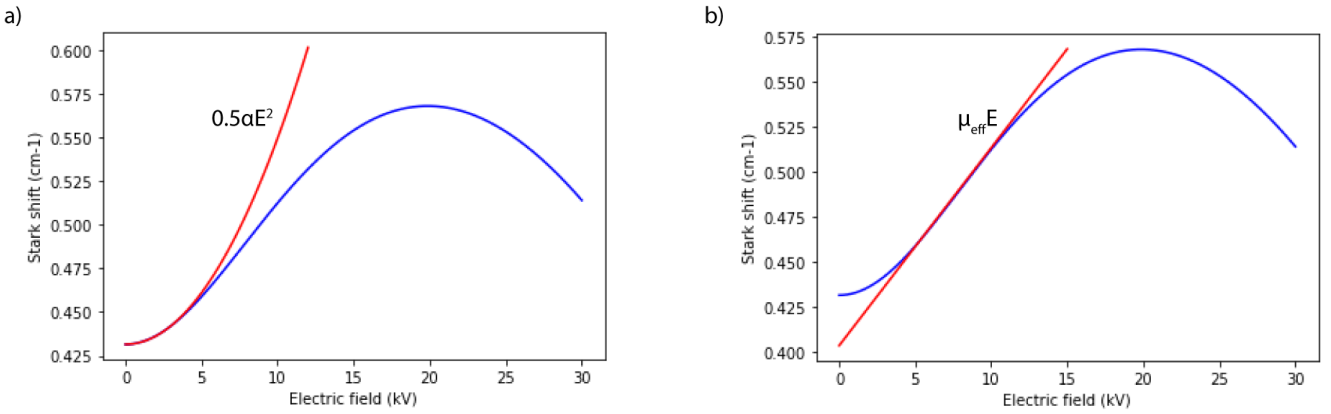

FIGURE 3.4: Quadratic and linear approximations to the Stark curve of BaF and SrF in $v = 0, N = 1, M = 0$ state for the low and intermediate field strength regime, respectively.

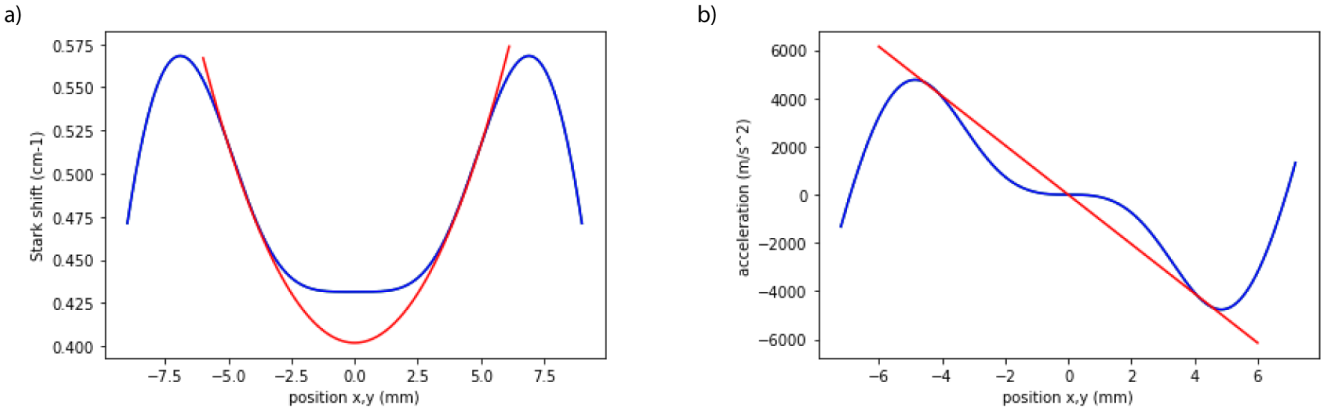

FIGURE 3.5: Transverse potential (**a**) and corresponding acceleration (**b**) experienced by SrF molecules inside the hexapole (blue) compared to a perfectly harmonic potential (red).

be approximated by a quadratic function of the form $\frac{1}{2}\alpha E^2$ [101][102][68]. Here, $\alpha = 0.18 * (\mu_e^2/B) = 0.0023641\text{cm}^{-1}/(\text{kV/cm})^2$. At intermediate field strengths, between roughly 5 and 15 kV/cm, the Stark shift W_S can be approximated by a linear function of the form $W_S = \mu_{eff}E$. Here, μ_{eff} acts as the derivative of Stark shift over the electric field strength [70]. The simulations use a value of $\mu_{eff} = 0.011$ $\text{cm}^{-1}/(\text{kV/cm})$.

3.2.4 Final design

A series of molecular trajectory simulations for varying free flight distances before and after the hexapole, in combination with varying hexapole lengths, were conducted by Hendrick Bethlem and Anno Touwen. A single hexapole of 390 mm length was chosen to implement in the existing setup. The final layout of the beamline elements required for installation of the hexapole is shown in Figure 3.6. For these dimensions, the improvement phase space matching is shown in Figure 3.10. A Hositrad HMC1000 series XY manipulator was included, to allow for aligning the hexapole parallel to and in line with the source and the decelerator. By moving one of the two plastic rings holding the hexapole rods together in the transverse plane, as shown in Figure 3.13, the center of the hexapole can be aligned with the center of the source. The second plastic ring is mounted inside a bellow, and consequently provides the the exit plane of the hexapole the freedom to move around slightly.

The magnitudes of the free flight sections before and after the hexapole are a result of matching the

required beamline elements (valve, close couplers, manipulator) with the perfect lens geometry mentioned in Section 3.2.1. While the schematic description in Figure 3.6 shows a free flight of 200 mm, followed by a hexapole of 396 mm, followed by 125 mm of free flight, further investigation concluded that these values were slightly different in reality. Therefore, the simulations presented from here on out use a free flight from cell exit to hexapole of 197 mm, a hexapole of 390 mm in length and a final free flight from the hexapole to the first ring of the decelerator of 127 mm. The total propagation distance between the cell exit and the first ring of the decelerator is then equal to 714 mm.

Figure 3.7 shows a transverse slice of the hexapole, as well as simulated molecular trajectories inside the hexapole. Figure 3.9 shows a histogram of the simulated transverse velocity distribution of the molecular beam as it enters the decelerator, before and after implementation of the hexapole. Since the potential experienced by the molecules is flat for small radial distances, as shown in Figure 3.5, molecules with a small transverse velocity are likely located near the hexapole center and will propagate in a straight line close to the beam axis. Therefore, the implementation of the hexapole effectively translates to an increase in the free flight distance for these molecules. Consequently, a larger number of molecules with a small transverse velocity will not enter the decelerator

When molecules approach the electrodes at larger radial distances, they experience a correcting force oriented towards the origin in the radial direction. Consequently, compared to the setup without the hexapole installed, an increased number of molecules with a relatively large transverse velocity (compared to the acceptance of the decelerator) will enter the decelerator, as shown in Figure 3.9. Figure 3.7 also shows the soft focus in both the transverse and longitudinal direction. The hexapole lens focuses the molecules into the decelerator rings, rather than a single point.

For the chosen hexapole geometry, the electric field at $r = r_0 = 6$mm has a strength of 15.0 kV/cm. The depth of the hexapole potential is equal to $W_S(r = r_0) - W_S(r = 0) = 0.123$ cm^{-1}, which corresponds to a temperature of 177 mK. In such a potential, the maximum (transverse) velocity that remains trapped is 5.24m/s.

3.3 Construction, implementation and alignment

To create the space necessary for the installation of the new components, the source was moved backwards roughly 390 mm, after which the alignment between source and decelerator was checked. The moving procedure consisted of slightly lifting the cold head using the laboratory crane and sliding the source chamber backwards. The geometry of the alignment procedure that followed the move is shown in Figure 3.11. From this geometry, an upper bound on the maximum distance D between the center of the cell exit (β) and the center of the first decelerator ring (α) of $D = 1$ mm is obtained, which serves as a measure of the alignment between the source and the decelerator.

The fiber coupler that emits the fluorescence detection laser (with radius B = 0.35 mm) was rotated towards a pair of mirrors and aimed through the decelerator towards the source, as parallel as possible to the longitudinal axis of the decelerator. The first mirror of this pair was adjusted by looking at the scattering pattern of the laser on the last decelerator ring, such that the laser entered the decelerator as close to the center of the last decelerator ring as possible, thereby maximizing distance A. The value of A is estimated to be no larger than 1 mm, a quarter of the inner diameter of the decelerator rings. The second mirror was used to maximize the intensity of the laser spot (with an estimated radius of $E = 1.5$ mm) on a detection card held in front of the cell exit, while retaining the circular shape of the spot. The source chamber was then moved in small increments, with the goal of minimizing D, the distance between the center of the cell exit and the center of the laser spot. The free flight distance from the cell exit to the first ring of the decelerator is obtained from Figure 3.6. The total travel length inside

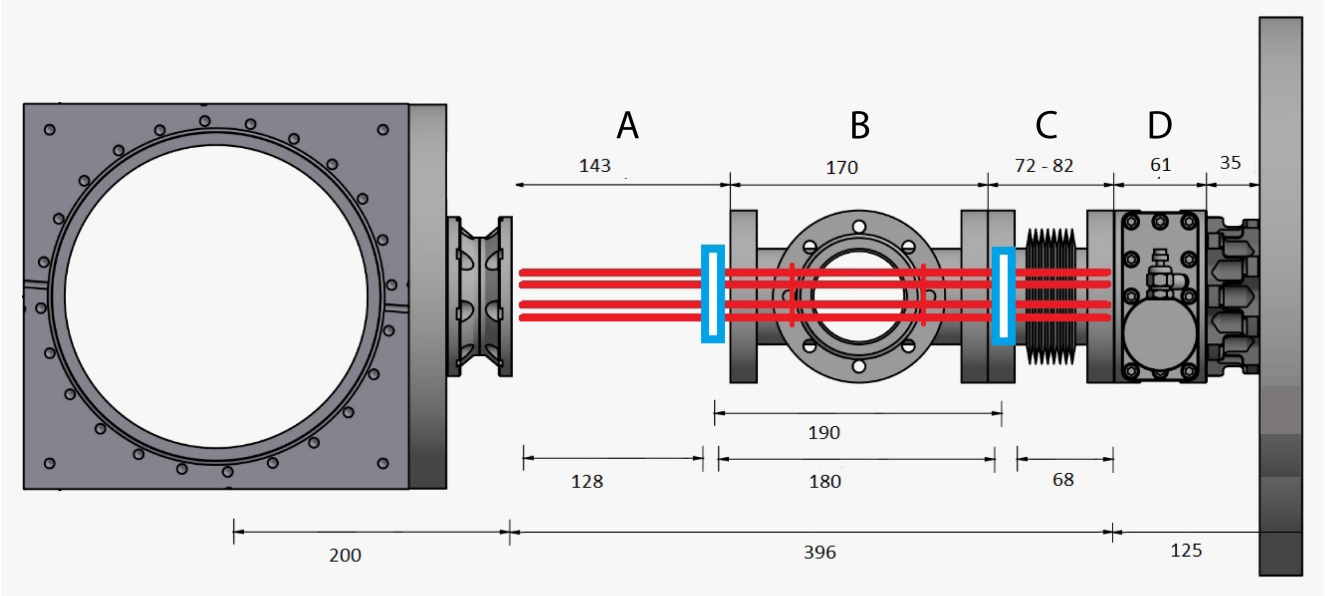

FIGURE 3.6: Schematic representation of the vacuum elements corresponding to the hexapole setup, placed between the source chamber (left) and decelerator (right). Molecules will propagate from left to right through the setup. Components belonging to the hexapole setup are the manipulator (A), the X-shaped vacuum chamber (B), a bellow (C) and a pre-existing valve (D). The hexapole rods (red) are held together by two plastic rings (blue), one of which is clamped inside the manipulator, while the other is clamped inside the bellow. The schematic drawing of the manipulator is proprietary information and is therefore not included.

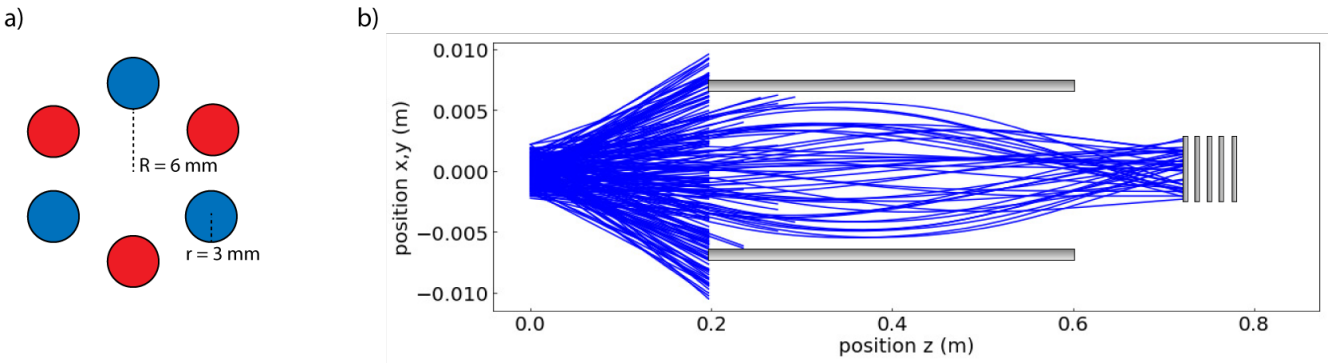

FIGURE 3.7: **a)** Geometry of the hexapole with positive (blue) and negative (red) polarities indicated. **b)** Molecular trajectories during 197 mm free flight, 390 mm inside the hexapole and 127 mm free flight towards the first ring(s) of the decelerator. The hexapole creates a radially oriented refocusing force that alters the molecular trajectories and acts as a lens. Once the molecules leave the hexapole, their trajectories become a straight line. A low field seeking molecule that moves radially out-ward experiences a centrally oriented correcting force. Since molecules experience less than a full period of transverse oscillation, this hexapole is referred to as a focuser as opposed to a guide.

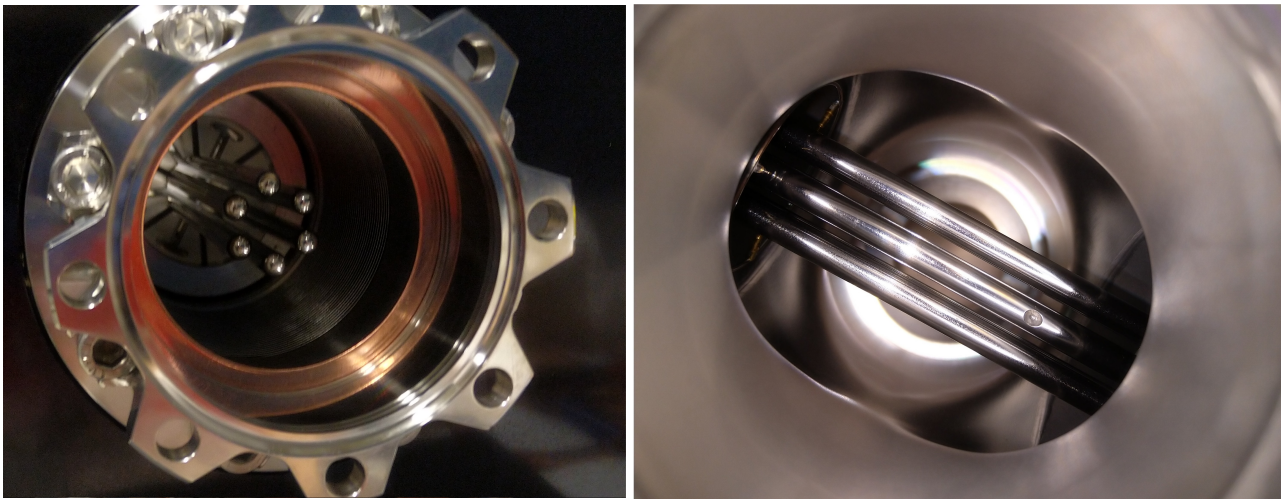

FIGURE 3.8: **a)** Hexapole mounted inside manipulator and vacuum chamber, as seen from source. The metal element in the foreground is the close coupler used to mount the manipulator to the source chamber. The plastic ring which holds the hexapole rods together has internal grooves to minimize the risk of discharges. **b)** Hexapole rods as seen from the top of the X-shaped vacuum chamber.

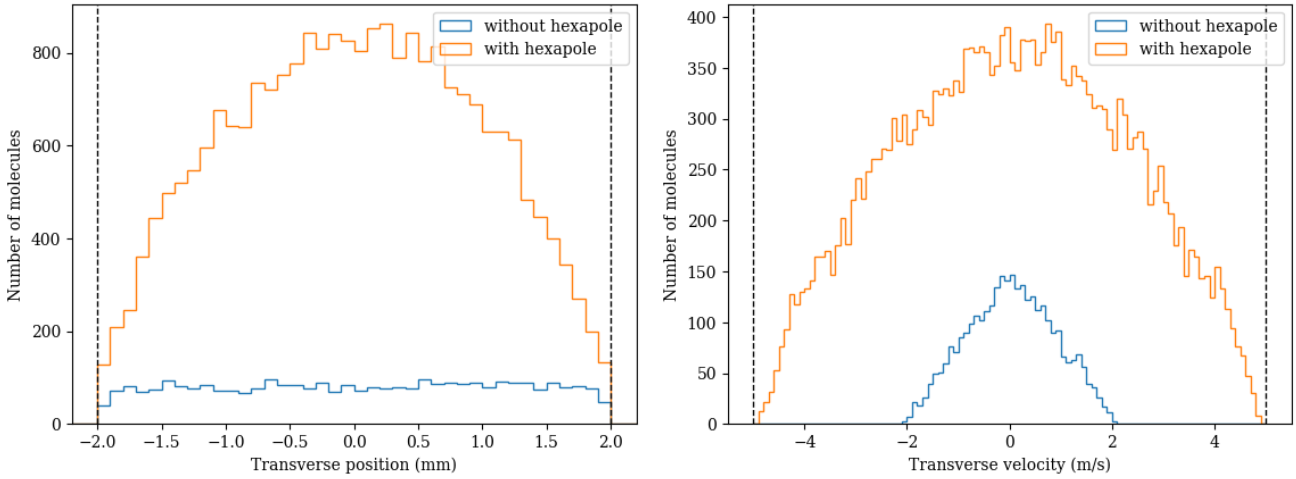

FIGURE 3.9: Provisional simulation results on the transverse position **(left)** and transverse velocity **(right)** distribution of the molecular beam which enters the decelerator, before (labeled 'without') and after (labeled 'with') implementation of the hexapole. The simulation was conducted using 200k molecules, with a molecular beam with a longitudinal velocity of 190 $\pm$10 m/s and a transverse velocity of 0 ± 20 m/s. The dotted lines denote the decelerator acceptance x_{acc} and $v_{x,acc}$, the values of which are specified in 3.2.3. In the simulation labeled 'with hexapole', a voltage of $\pm$ 3 kV is applied to the hexapole. A molecule with position x, y and velocity v_x, v_y is considered accepted if it falls within the phase space acceptance of each of the two transverse directions, i.e. $\left[(x/x_a cc)^2 + (v_x/v_{x,acc})^2\right] < 1$ and $\left[(y/x_a cc)^2 + (v_y/x_a cc)^2\right] < 1$. This method slightly overestimates the acceptance as the x and y phase space acceptances are decoupled. Therefore, at the time of writing, these simulation results are still under investigation.

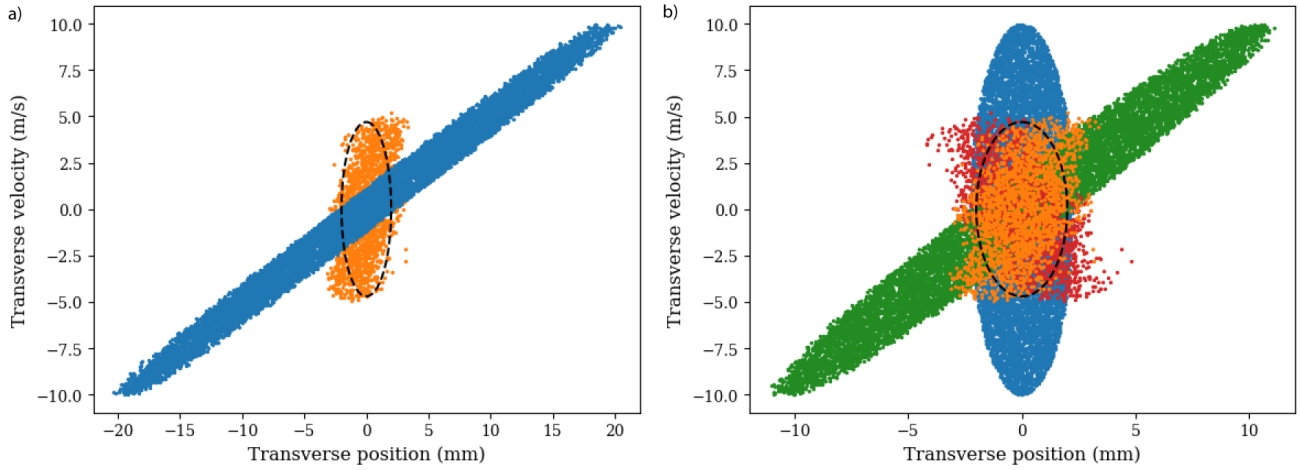

FIGURE 3.10: Simulated phase space distributions of the molecular beam at various points along the setup. **(a)** Phase space matching between molecular beam and decelerator acceptance (black dotted line) before (blue) and after the hexapole (orange) was installed, with dimensions as listed in Section 3.2.4. Optimal loading of the decelerator is achieved when the phase space acceptance is entirely filled by the molecular beam. **(b)** The phase space distribution of the molecular beam at four points along the setup, with distances between components as shown in 3.6: source emittance (blue), at the entrance (green) and exit (red) of the hexapole, and at the first ring of the decelerator (orange). In this simulation, a voltage of $\pm$ 3 kV is applied to the hexapole.

the decelerator is obtained from schematic drawings, and equal to 4536 mm.

Due to orientation of hexapole (shown in Figure 3.8, molecules can fly out through the side of the hexapole if the horizontal position of the hexapole is changed using the manipulator, as there is space between two electrodes. This is not taken into account in the simulations, which assume a molecule is lost if it's radial distance exceeds the electric field radius, corresponding to an impact with an electrode. Contrarily, molecules will at some point impact the side of the electrodes if the vertical position is changed using the manipulator.

The coupling between source and decelerator is expected to be optimal when the center of the hexapole entrance and exit are both perfectly in line with the center of cell exit and the first decelerator ring, thereby maximizing the measured number fluorescence counts. Conversely, the number of fluorescence counts is expected to decrease if the center of the hexapole entrance is transversely moved away from

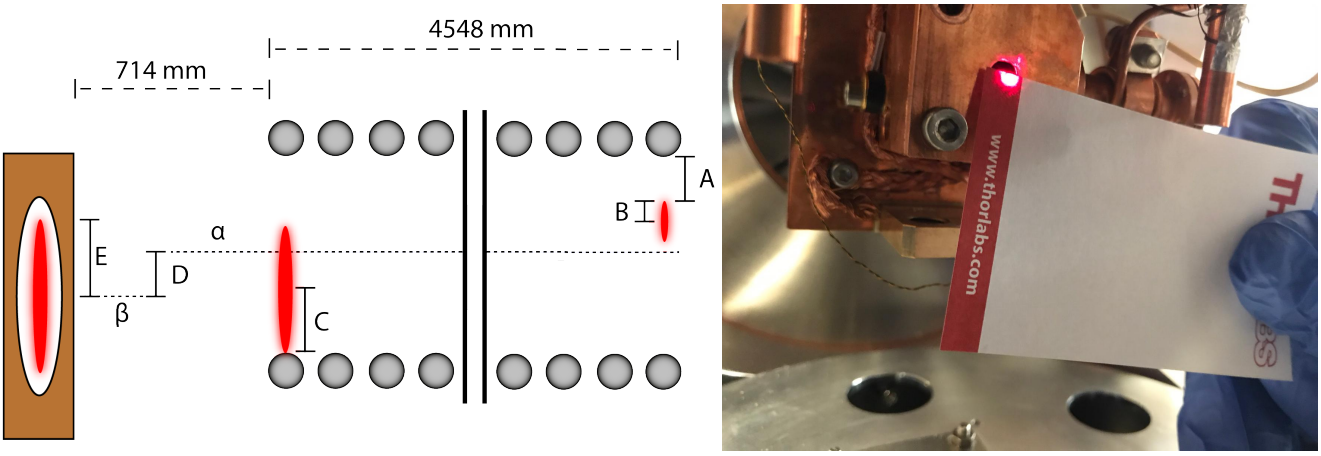

FIGURE 3.11: Alignment of the source relative to the decelerator after moving the source roughly 390 mm backwards.

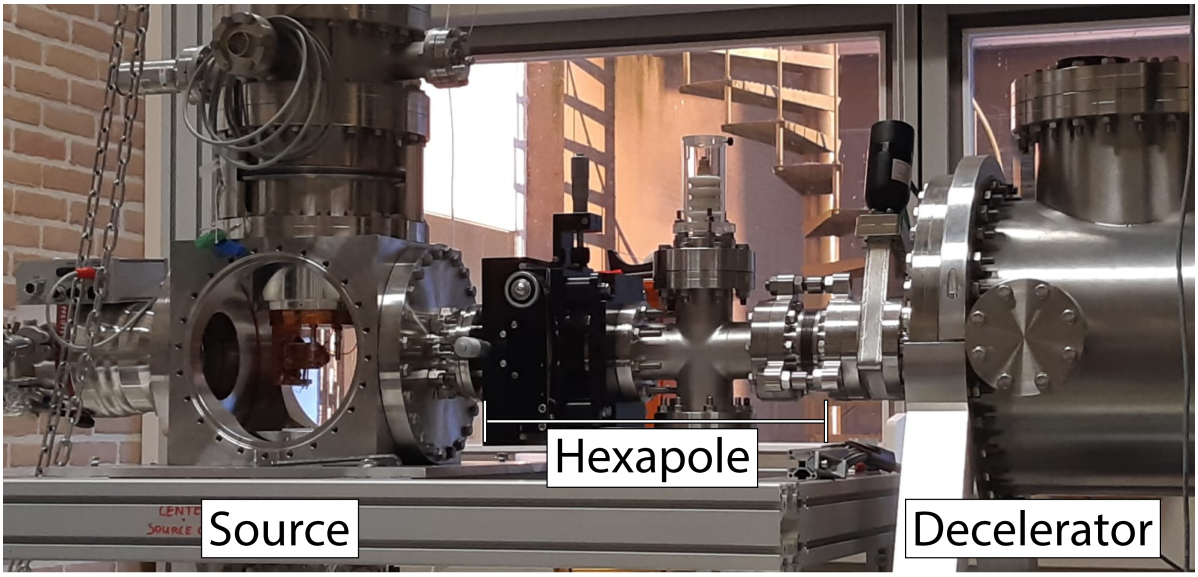

FIGURE 3.12: Picture of guide modules built in between source and decel

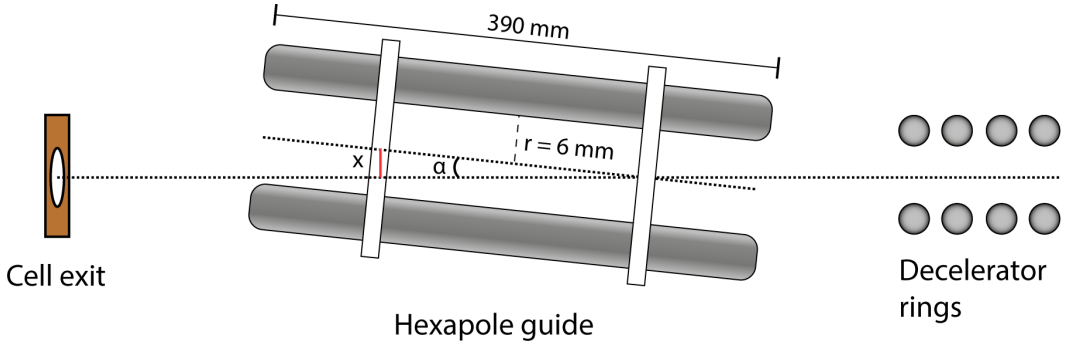

FIGURE 3.13: The manipulator can be used to move the first plastic holding ring in the transverse plane, thereby aligning the hexapole to the transmission axis between the source and decelerator. The second holding ring is mounted in a bellow, to provide the necessary flexibility if the manipulator settings are changed. All elements pictured are not to scale.

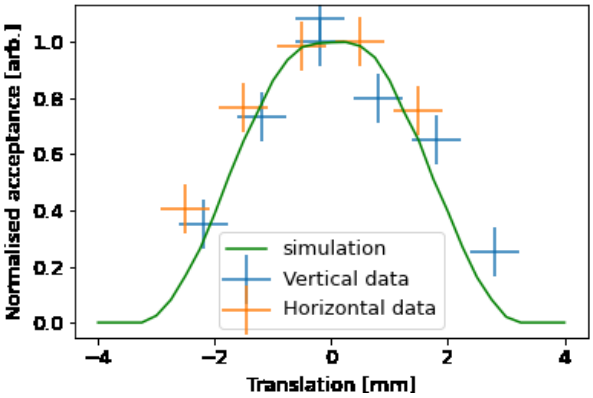

FIGURE 3.14: A series of fluorescence measurements along with the simulated transverse plane acceptance of the hexapole for various x and y translations of the manipulator. A decrease in acceptance corresponds to an increase of the value x in Figure 3.13, as the value of x denotes the translation of the manipulator. These measurements were taken to ensure that the hexapole was optimally aligned between the source and decelerator. The measurements are normalized to the highest recorded number of counts in the respective series.

the center of the rings, using the manipulator. However, only the entrance of the hexapole can be moved directly, as illustrated in Figure 3.13. Moving the hexapole entrance will also slightly move the exit, as the plastic holding ring is part mounted inside a bellow.

After the assembly of the elements required for installation of the hexapole was tested to be leakproof, it was placed between the source and decelerator, as shown in Figure 3.12. The manipulator was installed with no translation input through its dials, which means the hexapole should be located in the exact center of the manipulator. A series of 190 m/s ac-guiding measurements for varying manipulator displacements in both transverse directions were conducted, shown in Figure 3.14. A simulation of the hexapole acceptance depending on the manipulator displacement is included as well, with the hexapole rods at $\pm$ 3 kV. This simulation was conducted by Anno Touwen. The combination of measurement and simulation was used to put the manipulator at an x and y translation which is expected to produce the largest fluorescence counts at the end of the decelerator, corresponding to optimal alignment between the source, hexapole and decelerator.

3.4 Improvement in molecular transfer due to the hexapole lens

The focusing properties of the hexapole lens depend on the voltage applied to the electrodes, which alters the electric field strength inside. The phase space distribution of the molecular beam arriving at the decelerator and the acceptance of the decelerator are shown in Figure 3.10a, for the setup without and with a hexapole installed. Without the hexapole installed, the free flight distance between the source and decelerator severely limits the maximum transverse velocity of molecules that fall inside the acceptance of the decelerator. When an electrostatic hexapole (using dimensions illustrated in Figure 3.6) is placed between the source and decelerator, these transversely fast molecules experience a focusing force in the radial direction, which enables them to be focused into the first ring of the decelerator. Consequently, the hexapole allows for increased filling of the phase space acceptance of the decelerator.

The molecules that fall within the acceptance of the hexapole can be roughly divided in two categories, those with a relatively large or small transverse velocity. Molecules with a relatively large transverse velocity will experience a larger refocusing force for a longer amount of time compared to molecules with a small transverse velocity, as shown by the different curvatures of the trajectories shown in Figure 3.7b.

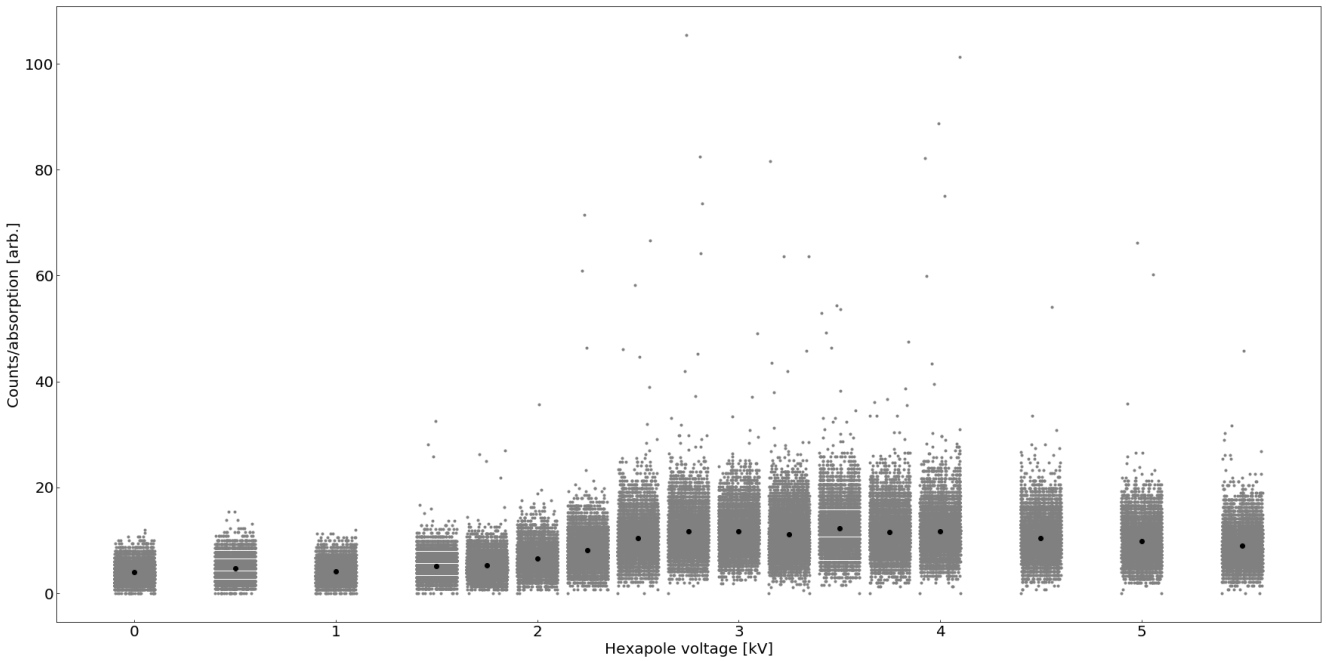

FIGURE 3.15: Fluorescence counts of the guided peak for 6000 measured shots at various hexapole voltages. A black dot marks the average value of all grey dots for a given voltage, i.e. all data points in a single block.

If the field strength inside the hexapole is increased, the plane of best focusing for these transversely fast molecules moves away from the decelerator, while altering the location of this plane for the relatively slower molecules to a lesser extent. Similarly, this plane will shift towards the decelerator if the voltage is decreased. The goal is to find a voltage for which the soft focus of the molecular beam focused by the hexapole lens maximally overlaps with the acceptance of the decelerator. The assumption is that this overlap is achieved when a maximum in the fluorescence counts originating from molecules that exit the decelerator is found. As ac-guiding generally produces a larger fluorescence signal compared to deceleration to arbitrary velocities, due to a decrease in trap depth for increasing deceleration strengths, the effect of the hexapole is tested using ac-guiding at 190 m/s.

The fluorescence data of the guided peak for 6000 measured shots at various hexapole voltages is shown in Figure 3.15. Each block corresponds to a measurement series at a single voltage setting. Each grey data point in the figure is obtained by adding the total amount of counts inside the guided peak and subtracting the total counts in a background region, and then dividing by the average measured absorption percentage for the 6000 shots. Counts obtained between 27.8 and 28.7 ms after the ablation trigger are assigned to the guided peak, while the background counts are collected between 37.8 and 38.7 ms after the trigger. The dots are slightly displaced to avoid overlap. A black dot marks the average value of all grey dots for a given voltage, i.e. all data points in a single block. These fluorescence measurements were obtained at a cell temperature of 17.5 K, a Neon flow rate of 10 sccm, an SF_6 flow rate of 0.5 sccm, a YAG laser power of 3-6 mJ and a LIF detection power of 0.5 mW. The gain is calculated by dividing the number of counts measured at each voltage V by the number of counts measured at $V = 0$. Therefore, the black datapoint at $V = 0$ corresponds to a gain of 1. The fluorescence measurements were first conducted in steps of 1 kV. An additional number of fluorescence measurements were taken in steps of 0.5 kV and 0.25 kV around the voltage where the fluorescence signal was seen to change most. The recorded absorption percentages for each voltage measurement are shown in Table 3.1, presented in the order in which the measurements were conducted.

A histogram of the recorded fluorescence counts for three different voltages applied to the hexapole

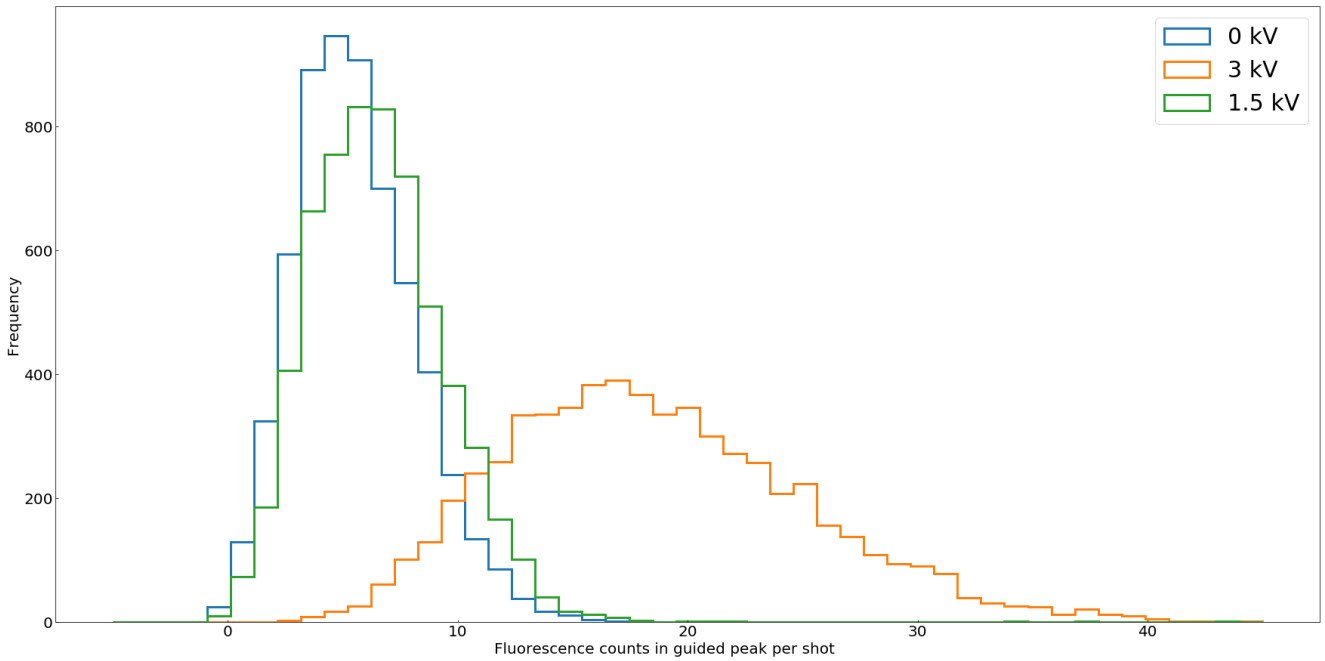

FIGURE 3.16: Histogram of the measured fluorescence counts in the guided peak for three different voltages applied to the hexapole, plotted using 50 equal sized bins. The asymmetric shape of the 3 kV curve is due to the presence of large positive outliers in Figure 3.15, but an absence of large negative outliers. Therefore, a standard deviation should not be fitted to each average point in Figure 3.15, as it cannot be said that the distribution is purely Gaussian. A more suitable error bar would be the full width at half maximum.

TABLE 3.1: Measured absorption value averaged over 6000 shots for various voltages applied to the hexapole.

Voltage V in kV	0	1	2	3	4	5	0.5	1.5	2.5
Absorption %	1.5	1.51	1.54	1.59	1.52	1.51	1.3	1.32	1.41
Voltage V in kV	3.5	4.5	5.5	2.25	2.75	3.25	3.75	1.75	
Absorption %	1.36	1.46	1.42	1.51	1.48	1.79	1.58	1.60	

is shown in Figure 3.16, which serves two purposes. First, to develop an idea of the fluctuations in the intensity of the beam emitted by the source and to what degree these fluctuations contribute to the spread in the recorded fluorescence counts shown in Figure 3.15. Second, to decide if the error bars that should be attached to the averages shown in 3.15 should be solely based on countings statistics, i.e. the standard deviation, or if a different type of error bar is more appropriate. The absorption percentage, which is measured 5 mm after the molecular beam exits the cell, provides a relative estimate of the intensity of the beam produced in a single shot. However, the data acquisition system setup did not allow for coupling the recorded absorption percentage to a collection of PMT timestamps corresponding to a single shot. Consequently, only the average absorption percentage for an entire measurement duration can be used. Therefore, when comparing the changes in the recorded number of counts between shots, it is impossible to determine if such a change is due to the lensing effect of the hexapole or due to fluctuations in the source. Furthermore, Table 3.1 shows that the largest and smallest recorded average absorption percentage differ by almost 30 %. One possible method to further distinguish between statistical error, i.e. counting statistics, and systematic error, i.e. beam intensity fluctuations, would be to measure the fluorescence counts for different total numbers of shots and seeing how the shape of the distribution changes.

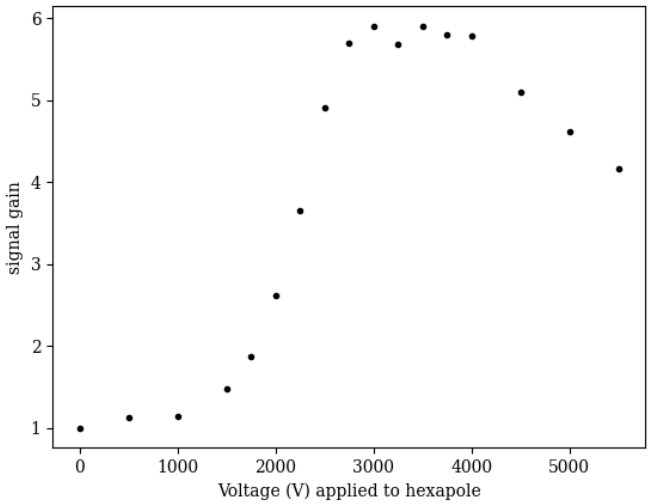

FIGURE 3.17: Average measured gain in the fluorescence signal per percentage absorption of the guided peak for various voltages applied to the hexapole. Each data point is normalized to the measurement value at $V = 0$, where 9667 counts per percentage absorption where recorded. Each measurement consists of 6000 ablation shots.

The average measured gain in the fluorescence signal of the 190 m/s guided peak for various voltages applied to the hexapole is shown in Figure 3.17, together with a simulation of the detected number of molecules guided at 190 m/s for given acceptance and detection zone dimensions. The next section discusses the credibility of the gain factor in detected guided or decelerated molecules that can be attributed to the implementation of the hexapole. Figure 3.17 shows no error bars, as time did not allow for including a full width at half maximum error bar based on the histogram of the number of counts (Figure 3.16).

3.4.1 Estimating the increase in intensity due to implementation of the hexapole

The next goal is to determine the factor increase in the detected number of molecules which can be attributed to implementation of the hexapole. In order to do so, a comparison needs to be made to the situation before the hexapole assembly (Figure 3.6) was installed. However, the exact factor increase in the detected number of molecules which can be attributed to installation of the hexapole cannot be inferred from Figure 3.17 alone. With the hexapole off, the molecules propagate through 714 mm of free flight, compared to 369 mm before the hexapole was installed. Therefore, the maximum signal gain of a factor 6 suggested by Figure 3.17 is not the true gain in fluorescence counts due to installation of the hexapole, but rather the maximum intensity difference between turning the hexapole on and off.

Therefore, a number of molecular trajectory simulations were conducted for various decelerates acceptances and detection zone dimensions. The simulated curve that produced the best agreement with the trend of the measured data was recorded and is shown as the blue line in Figure 3.17. As a final step, a simulation using the same acceptance and detection volume as the recorded simulation, but with the dimensions of the setup as they were before the hexapole was installed, was conducted. The number of detected molecules from this simulation was recorded as well, and is shown in the red dotted line in 3.17. An estimate of the increase in the detected number of molecules which can be attributed to the implementation of the hexapole can be obtained by comparing the largest difference in signal gain between both simulated curves for a certain hexapole voltage. Using this approach, Figure 3.17 suggests a factor 2.3 increase in the beam intensity due to implementation of the hexapole.

However, the true factor increase in the beam intensity is likely different, as there are various currently

unknown parameters in the fluorescence detection process. First, the 0.7 mm diameter d_ϕ of the detection laser is at least several times smaller than the transverse size of the molecular beam $\mathcal{D}$ in the detection volume, as illustrated in Figure 3.19. The detection laser is aligned to pass through the center of the molecular beam. Therefore, the laser only excites a small spatial fraction of the beam, likely missing many of the guided or decelerated molecules, especially those with a relatively large transverse velocity. Furthermore, the transverse velocity of the beam acts to spread out the beam even more, further decreasing the spatial fraction of the beam which interacts with the detection laser. The presence of an electric field in the detection zone will cause Stark shifts of the hyperfine levels of the molecules, in both the ground state and excited state of the transition employed for fluorescence detection. Consequently, an electric field will affect the fluorescence efficiency by changing the resonance conditions.

Lastly, the transverse acceptance of the decelerated has only been simulated, not directly measured. As the molecular density inside the moving traps is sufficiently low that molecules do not experience collisions inside the decelerator (order 10^3 molecules per shot distributed over several traps of order 1 mm^3 [80]), the acceptance of the decelerator largely determines the spatial and velocity spread of the molecules exiting the decelerator. Consequently, measuring the width and transverse velocity of the beam at various distances after the last ring of the decelerator can enable a measurement of the phase space acceptance of the decelerator.

The truthfulness of these simulations, and the estimate on the gain in the detected number of molecules, depends on the validity of the input parameters. Some of these, such as the rotational constant B or electric dipole moment μ_e of SrF and BaF, have been extensively studied. Other parameters which are inherent features of the setup in our laboratory, such as the positional and velocity acceptance of the decelerator and the volume inside which molecules can be detected, are known to a lesser extent. The next section describes a series of simulations which calculate the number of molecules detected after the decelerator for a range of hexapole voltages, for varying decelerator acceptances and detection volumes.

3.4.2 Simulation sensitivity to decelerator acceptance and detection volume

Two parameters with a large influence on the measured increase in fluorescence signal after installation of the hexapole are the acceptance of the decelerator and the volume from which fluorescence light is collected by the lens system, dubbed the detection volume. A number of simulations showing the change in the detected number of molecules for varying detection zone dimensions and decelerator acceptances are presented in this section.

As shown in Figure 2.10, the acceptance of the decelerator operated at 5 kV for SrF in the $X^2\Sigma^+(\nu' = 0, N = 1)$ is calculated to have a maximum allowed transverse position of $\pm$ 2 mm and a maximum velocity of $\pm$ 5 m/s. Here, the position acceptance is only limited by the physical size of the rings. However, the graphical representation of the electric field traps, obtained from [66] and shown in Figure 2.9, suggests that the acceptance might be slightly smaller in practice. The outermost closed equipotential line in the smallest confining potential, shown in Figure 2.9c, ends at a radial distance of roughly 1.5 mm. Molecules located outside of a closed equipotential line will not be stably trapped. However, due to the chosen stepsize between equipotential lines in Figure 2.9, the line that separates the regions where molecules are either attracted to the electrodes or pushed towards the trap center is likely not shown. Therefore, molecules will be able to extend slightly beyond the previously mentioned 1.5 mm and still be stable trapped. A change in the position acceptance of the decelerator on the guided or decelerated number of molecules is also investigated in the simulations.

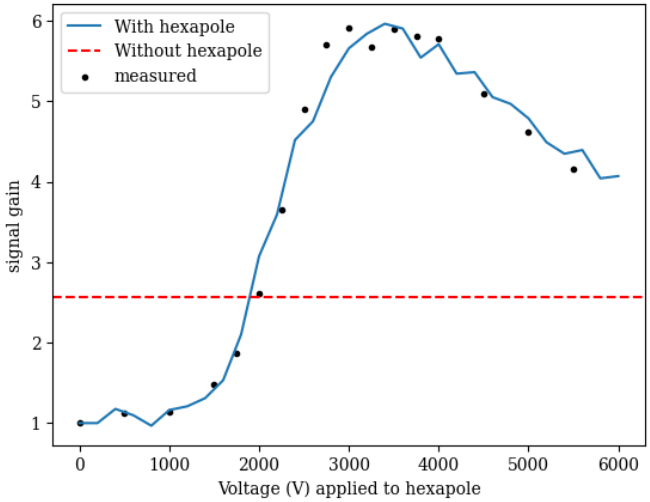

FIGURE 3.18: Measured data from Figure 3.17 shown together with molecular trajectory simulation results. The measured data points are normalized to the number of recorded fluorescence counts at $V = 0$, while both simulated curves are normalized to the simulated number of detected molecules at $V = 0$. Simulation results are obtained using 200k molecules for each of the 31 voltage steps. The red line denotes the number of detected molecules using 369 mm free flight between the source and decelerator, without a hexapole installed. The blue curve contains simulation results for a hexapole implemented as described in Figure 3.7. Both simulations use a phase space acceptance of the decelerator of $x_{acc} = \pm$ 2 mm, $vx_{acc} = \pm$ 2.6 m/s, and a transverse detection area of 1.9 mm by 0.7 mm in the horizontal and vertical direction, respectively, as viewed from the propagation direction of the molecular beam [80].

The simulation considers a molecule detected if it enters the detection volume, which is a transverse area located 10 mm after the decelerator. However, in reality, the molecules are indirectly detected by collecting the fluorescence light emitted after excitation on the electronic transition described in 2.3.3. The fluorescence light is emitted uniformly in all directions and has to be collected by a number of lenses and mirrors to be sent to the active area of the PMT. As shown in Figure 3.19, the fluorescence laser interacts with only a small part of the beam. After implementation of the hexapole, the fluorescence laser will interact with an even smaller fraction of the molecular beam, due to the presence of larger transverse velocities (Figure 3.9) and the increased position spread (Figure 3.19b). Therefore, even if the hexapole manipulates the beam exactly the same in both reality and the simulation, the hexapole voltage dependent number of recorded fluorescence counts and simulated detected number of molecules might not evolve the same.

The simulations presented in Figures 3.18 through 3.22 aim to produce an idea of the sensitivity of the detected number molecules to a change in one of the input parameters, namely the decelerator acceptance and the detection zone dimensions. The simulations illustrate that a change in detected number of molecules between hexapole on and hexapole off due to a change in one parameter, can be negated by a change in another parameter. Therefore, it is likely that several different combinations of position/velocity acceptance and detection zone dimensions can be found that create a good agreement with the measured curve. One such combination is shown in Figure 3.18, which uses a position acceptance of $\pm$ 2 mm, a velocity acceptance of $\pm$ 2.5 m/s and the dimensions of the detection zone as specified in Section 3.2. Consequently, no meaningful information on the possible value of the decelerator acceptance, detection zone dimensions or signal gain due to implementation of the hexapole can currently be extracted from agreement between simulation and theory.

It is impossible to determine the value of position and velocity acceptance of the decelerator and both dimensions of the detection area, using a measurement series which varies only a single parameter.

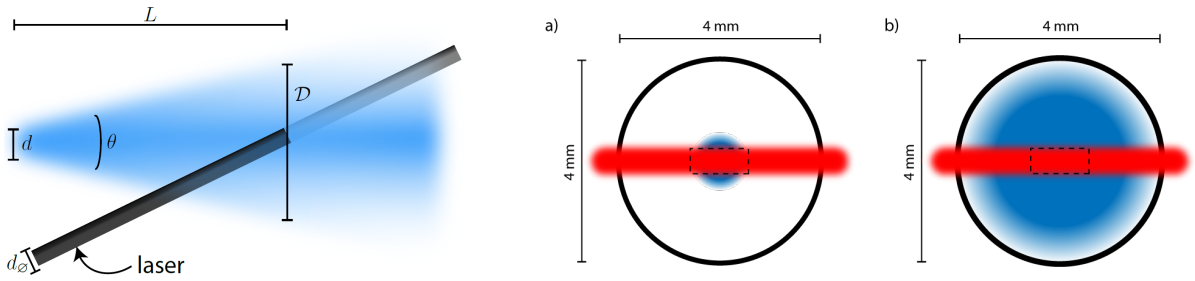

FIGURE 3.19: Side and frontal view of the detection zone, where the fluorescence laser interacts with only a small part of the molecular beam. **Left:** Once the voltage waveform is turned off, the molecular beam will start to diverge. At a distance L from the last decelerator ring with diameter d, the fluorescence laser with diameter d_ϕ interacts with the molecular beam. Figure from [20]. **Right:** Frontal view of the spatial distribution of the molecular beam (blue) as it exits the last ring of the decelerator (black) and crosses the detection laser (red), before (a) and after (b) implementation of the hexapole. The dotted line notes the dimension of the detection zone as mentioned in 3.2.3. Note that the transverse velocities of the molecules are not taken into account in this figure. The implementation of the hexapole leads to improved phase space matching between the molecular beam and the decelerator acceptance, which leads to an increase in the diameter of the beam exiting the decelerator. The width of the decelerated beam before installation of the hexapole is ($\sim$ 1 mm), obtained from [80].

Figures 3.9 and 3.19 show that is likely that the measurement series first presented in Figures 3.15 is obtained by looking only at a small transverse fraction of the molecular beam, due to the increased transverse size and velocity of the beam after installation of the hexapole. Therefore, alternative methods have to be devised in order to measure each of these unknown parameters separately. One proposed method to measure the decelerator acceptance is to mount an EMCCD camera antiparallel to the molecular beam at a distance L from the end of the decelerator, in order to measure $\mathcal{D}$, the transverse size of the beam at a certain distance from the last ring of the decelerator, by capturing the fluorescence light emitted by the molecules. Here, the naming convention presented in Figure 3.19a is used. A first estimate of the transverse velocity of the beam can then be obtained by measuring the width of the molecular beam at one distance from the last ring, using a laser sheet large enough to interact with the entire beam. If only one transverse width measurement is conducted, an assumption on the transverse width of the beam as it exits the last ring is required in order to determine the transverse velocity. Alternatively, if the transverse width of the beam is measured at two distances from the last ring of the decelerator, both the transverse velocity and the transverse width of the beam as it exits the last ring can be determined. Under the assumption that the hexapole fills the entire phase space acceptance of the decelerator (Figure 3.10), this will enable a measurement of the phase space acceptance of the decelerator.

3.5 Voltage waveform optimization

In order to further increase the intensity of the guided or decelerated molecular beam, a number of improvements were made to the voltage waveform applied to the electrodes. As mentioned in Section 2.3.1, the waveform applied to the rings starts guiding or decelerating as soon as the synchronous molecule enters the decelerator. Furthermore, the waveform is shut off once the synchronous molecule exits the last ring of the decelerator. This mode of operation has a number of consequences for molecules that arrive earlier or later compared to the synchronous molecule. The faster-than-synchronous molecules will experience an electric field as they pass through the detection zone, which alters their fluorescence resonance conditions. The slower-than-synchronous molecules will not have reached the last ring of the decelerator when the voltage waveform, and consequently the confining potential, is turned off. With no confining potential present, the slower-than-molecules are free to move in the transverse direction while propagating through the last few rings. This transverse spreading can lead to additional losses in the fluorescence signal due to for instance collisions with the decelerator rings.

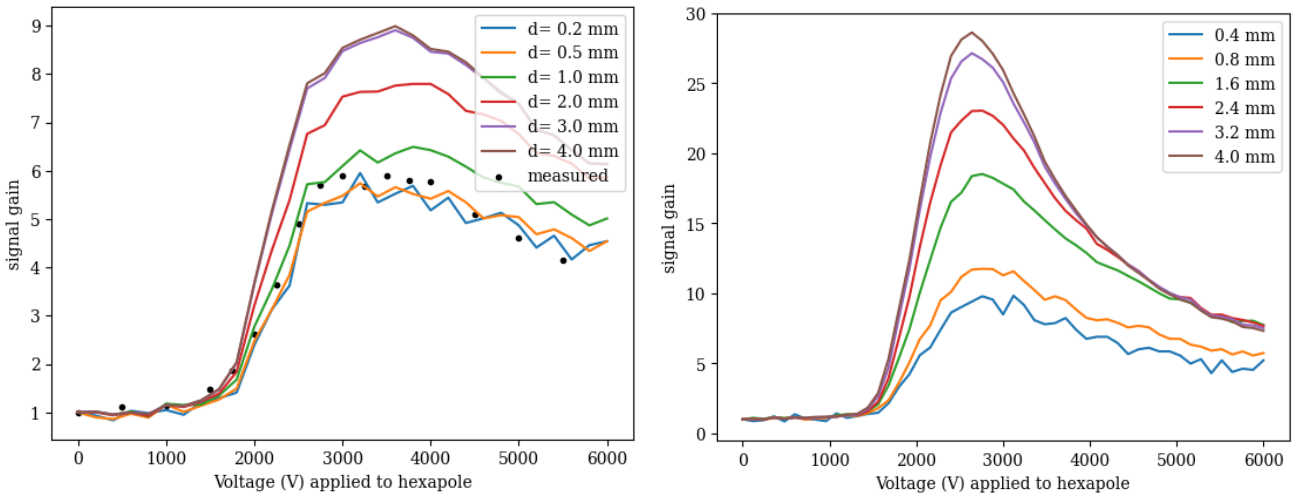

FIGURE 3.20: Simulated signal gain in the fluorescence counts of the guided peak for increasing LIF detection laser beam diameter. All curves are normalized to the detected number of molecules at zero voltage for their respective parameters. **a)** This simulation was conducted using a position acceptance of $\pm$ 1.6 mm, and a velocity acceptance of $\pm$ 2.5 m/s, using 51 voltage steps with 500k molecules each. The position acceptance used here is slightly smaller than the theoretically calculated value, as explained in 3.4.2. **b)** If the full theoretically calculated acceptance of the decelerator (as shown in Figure 2.10) is used, the electric field traps will contain more molecules with a relatively large transverse velocity compared to a). Such faster molecules will quickly diverge as they exit the decelerator. Therefore, the effect of increasing the LIF detection laser beam diameter on signal gain is larger compared to the figure on the left. The horizontal dimension of the detection zone is the same for both simulations, with a value as specified in Section 3.2.

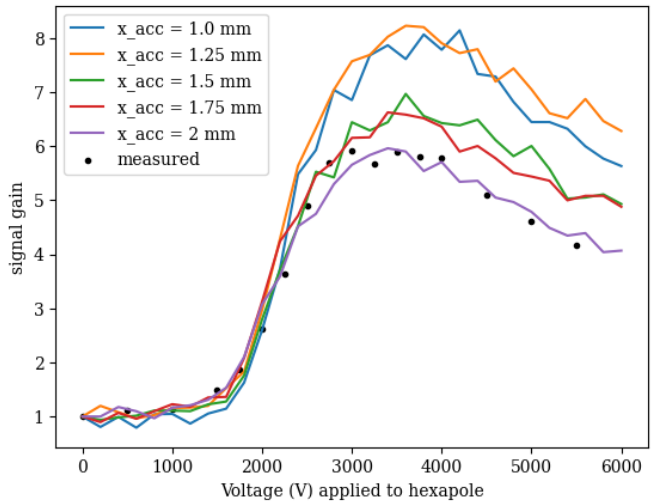

FIGURE 3.21: Simulated signal gain in the fluorescence counts of the guided peak for decreasing radial position acceptance of the decelerator. Simulations are conducted using 31 voltage steps with 200k molecules each, with a velocity acceptance of $\pm$ 2.6 m/s and the dimensions of the detection zone as specified in 3.2.3.

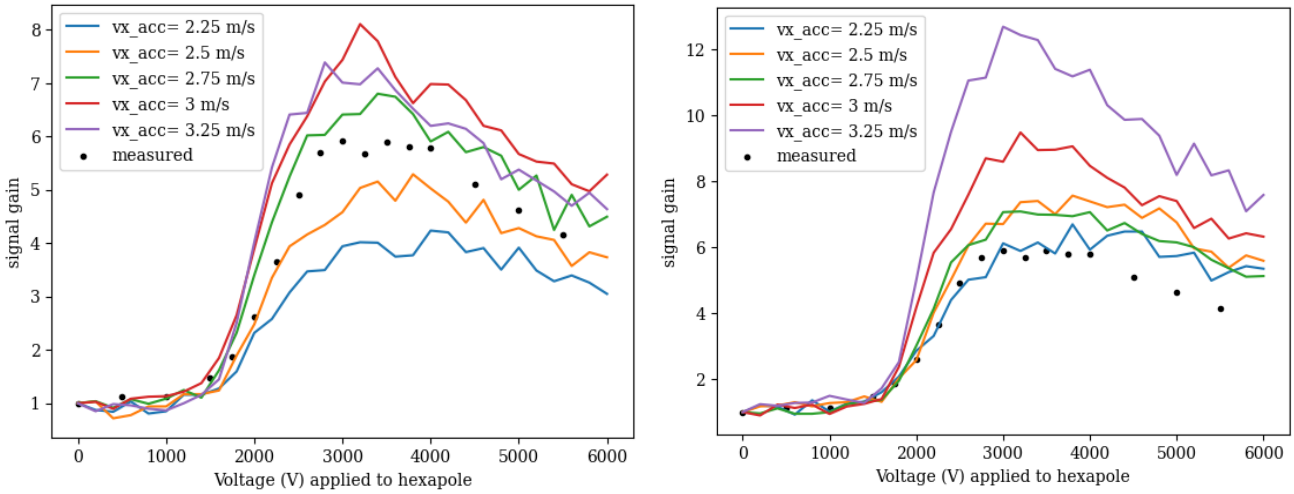

FIGURE 3.22: When the transverse position acceptance of the decelerator is reduced from ± 2 mm (**left**) to ± 1.5 mm (**right**), the influence of increasing velocity acceptance on the signal gain increases. Since a zero voltage on the hexapole corresponds to free flight, reducing the position acceptance means that the maximum transverse velocity a molecule can have in order to still enter the decelerator decreases as well. Simulations are conducted using 31 voltage steps with 100k molecules each, with the dimensions of the detection zone as specified in 3.2.3.

In order to compare the effects of an electric field in the detection zone and the transverse spreading of the beam by turning off the waveform before the molecules reach the last ring, two fluorescence measurements were conducted, for dc-guiding waveforms which are turned off at two different moments in time after the ablation trigger. These two measurements are shown in Figure 3.23a. DC-guiding was chosen such that the electric field strength in the detection zone is constant. The voltage waveform used for dc-guiding is shown in Figure 3.23b. One waveform is turned off 40 ms after the ablation trigger, such that all molecules experience both a transverse confining potential until they reach the last ring, as well as an electric field in the detection zone. The second waveform is turned off 30 ms after the ablation trigger, such that part of the beam will not experience a transverse confining potential for the last few rings, similar to the deceleration waveforms used at the time. Just after the 30 ms mark is reached, the fluorescence counts of the 30 ms waveform jump sharply, presumably due to improved resonance conditions due to the lack of an electric field. However, the subsequent loss in fluorescence counts between 30 and 40 ms, presumably due to the lack of a transverse confining potential, is much larger compared to the 40 ms waveform. Therefore, a number of changes were made to the waveform in order to ensure both the slower- and faster-than-synchronous molecules experiences a trapping potential until they pass through the last ring of the decelerator.

3.5.1 Reducing transverse spreading

As mentioned in Section 2.3.1, the waveform is turned off once the synchronous molecule exits the last ring of the decelerator. Therefore, the decision was made to investigate the merit of guiding additional traps into and out of the decelerator, in order to hopefully increase the number of decelerated molecules. Creation of the molecular beam starts with ablating the target, after which repeated collisions with the neon background gas act to cool the created molecules. As the number of collisions is different for each molecule, the source creates a relatively long pulse of molecules [20]. The peak in the absorption signal shown in Figure 2.14a is expected to correspond to the largest per-pulse flux of molecules. Using the absorption signal shown on an oscilloscope, this peak is estimated to arrive 0.36 ms after the ablation trigger. At an initial velocity of 190 m/s, 0.36 ms corresponds to an effective distance traveled of $\sim$ 68 mm. This distance alters the moment in time when the synchronous molecule is expected to enter the decelerator, and therefore needs to be incorporated in the calculation of the voltage waveform.

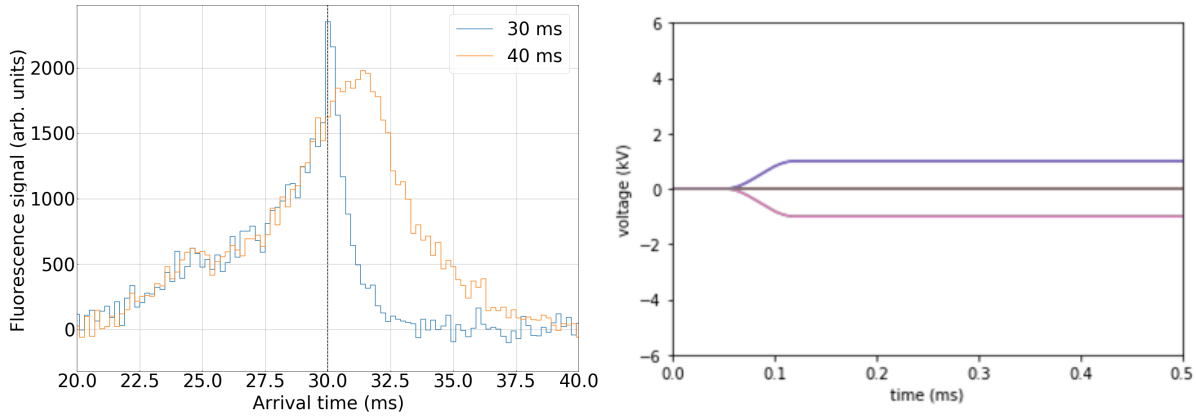

FIGURE 3.23: **a)** Measured fluorescence counts after 3000 shots for two dc-guiding at 2 kV waveforms, which are turned off at 30 ms or 40 ms after the ablation trigger. Both waveforms have a nonzero voltage on the last ring. Consequently, all molecules experience an electric field in the detection zone while the waveform is turned on. The difference in fluorescence counts after 30 ms enables a comparison between the effect of transverse spreading and the presence of an electric field. **b)** Each line corresponds to the voltage applied to an electrode during dc-guiding at 1 kV. In dc-guiding operation mode, the polarity of the voltage applied to electrode number n varies as p_n = +,0,-,0,+,0,-,0.

From the ac-guiding at 190 m/s measurements shown in for instance [64], the electric field trap which houses the synchronous molecule is shown to be preceded by at least 4 traps, and succeeded by up to 15 traps. When operated in ac-guiding mode, it is rather difficult to ascertain which peaks correspond to the guided peak and which correspond to the surrounding, non-longitudinally-trapped wings. Therefore, it was chosen to extend the waveform to include the ac-guiding of 8 traps before and 20 traps after the synchronous molecule, for a total package length of 28 traps. The total length of the decelerated peak should therefore stretch 48 mm before and 120 mm after the trap holding the synchronous molecule.

As there is no fluorescence detection near the cell entrance and the free flight distance between the hexapole exit and first ring of the decelerator is sufficiently large, any latent electric fields will not negatively alter time-of-flight measurements. Therefore, a 190 m/s ac-guiding waveform can be started as soon as the ablation trigger is registered. This is done until the synchronous molecule is 120 mm or 20 traps into the decelerator, after which the voltage ramp-up to 5 kV required for deceleration starts. Full deceleration to 30 m/s has to be completed with enough time left for the ramp-down to ac-guiding at 30 m/s before the first traps enters the last ring of the decelerator, which happens 48 mm or 8 traps before synchronous molecule leaves the decelerator. A final section of 168 mm of ac-guiding at 30 m/s guides out all 28 traps, after which a ramp-down to zero voltage is performed.

The specifications of the amplifiers dictate that the switching frequency should stay below 30 kHz. Since the full frequency span can be reached in half a period, the ramp-time would be 16 µs, which corresponds to a minimum distance of 3 or 0.5 mm for traps propagating at a velocity of 190 m/s or 30 m/s, respectively. However, the transition between different sine waves in the waveform becomes smoother if half a cycle, depending on the frequency determined by the current velocity, is used. In that case, the ramp-down time is equal to $Lv/2$, where L is the distance between two rings attached to the same electrode and v the velocity of the trap. If this ramp-down time is converted to a distance, it shows that the traps propagate exactly 6 mm, which corresponds to the center-to-center distance between successive traps. All 28 traps are dealt with as equally as possible in terms of free flight after the decelerator and Stark shifts in the detection zone. Since the period of a guiding waveform corresponds to a distance of exactly two traps, every other packet arriving at the detection zone experiences exactly the same electric field.

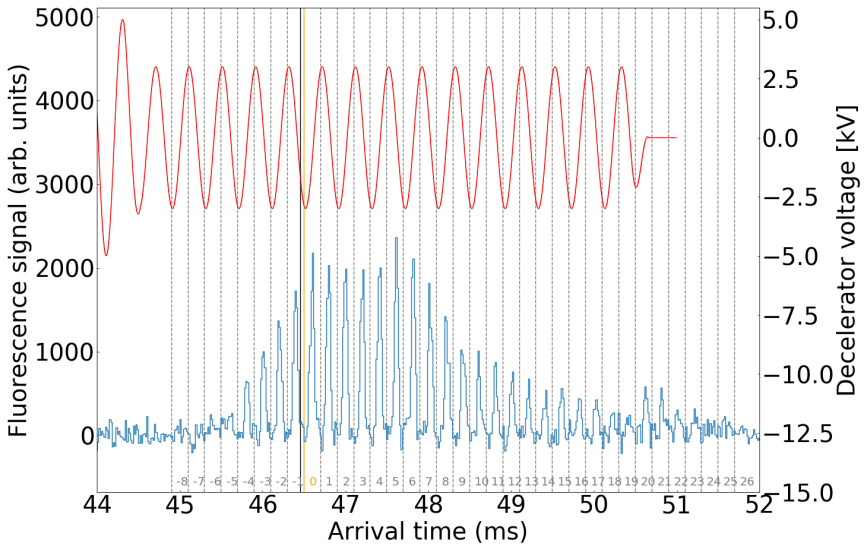

FIGURE 3.24: Fluorescence time-of-flight signal obtained from 72000 shots of deceleration to 30 m/s (blue), using the waveform improvements mentioned in Section 3.5.1. The waveform (red) shows the transition from deceleration at an amplitude of 5 kV to ac-guiding at an amplitude of 3 kV, and a final rampdown to zero voltage. The yellow line corresponds to the expected arrival time of the synchronous molecule.

A 5 kV deceleration to 30 m/s measurement consisting of 72000 shots using the aforementioned changes to the waveform, obtained after installation of the hexapole, is shown in Figure 3.24. The source parameters used to obtain this measurement are the same as mentioned in Section 3.4. Since two more peaks in the fluorescence signal can be distinguished after the voltage waveform is turned off, the ac-guiding sections before and the deceleration section could be further extended, as there are apparently more traps beyond the 28 selected in this waveform with molecules residing in them.

The combined effect of both the installation of the hexapole and the added sections of ac-guiding to the waveform on the detected number of decelerated molecules is illustrated by comparing Figure 2.14 to Figure 3.24. The comparison shows an increase in the number of packets or buckets that can be distinguished in the time-of-flight signal, which corresponds to an increase in the detected number of decelerated molecules. Consequently, the gain factor in number of molecules obtained at the end of the decelerator when decelerating to 30 m/s is likely larger than the factor 2 obtained using ac-guiding at 190 m/s. Furthermore, a second comparison between the aforementioned deceleration to 30 m/s measurement and a 3 kV ac-guiding at 190 m/s measurement is shown in Figure 3.25. This second comparison illustrates that the number of filled traps in the deceleration to 30 m/s measurement is very similar to that the ac-guiding measurement, which shows a step in the direction of the efficient deceleration required for the final eEDM experiment.

3.5.2 Shielding the detection volume from electric fields

As mentioned previously, the presence of an electric field in the detection zone will shift the resonance conditions and influence the number of fluorescence counts that are measured. This field will be present as long as a waveform is applied to the rings, which also includes the ramp-down sequence to zero voltage. Furthermore, an electric field in the detection zone also complicates the calculation of the number of detected molecules inferred from the fluorescence signal, since the influence of the rapidly oscillating voltage waveform on the fluorescence signal is difficult to predict. This difficulty is illustrated in Figure 3.27a, where two 2 kV dc-guiding waveforms are compared. These waveforms differ only in the order in which the rings have a voltage applied to them. Therefore, it is surmised that the only cause for the

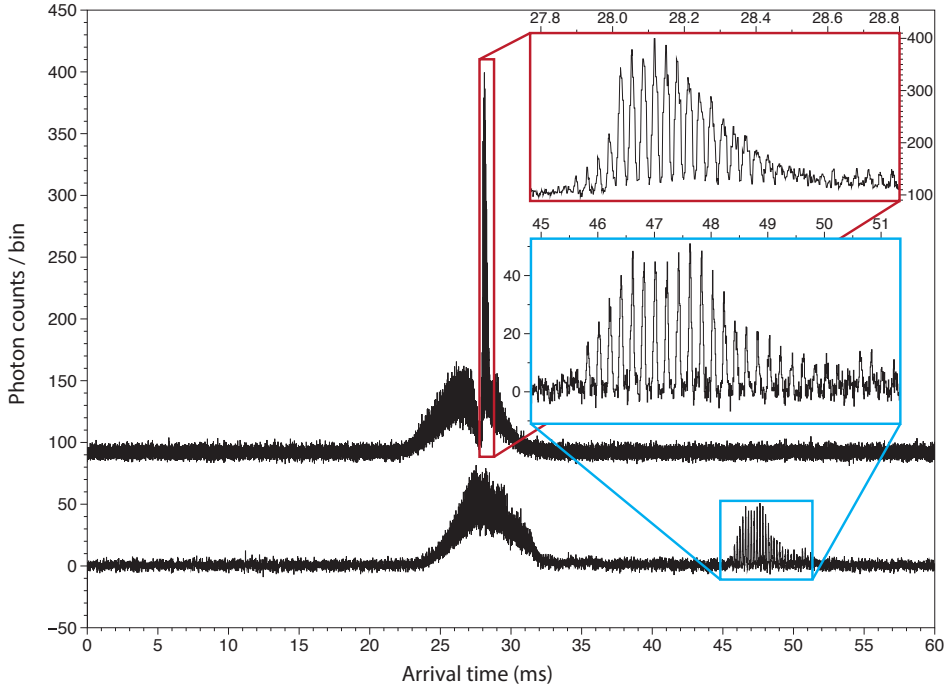

FIGURE 3.25: Fluorescence time-of-flight signal obtained from 3 kV ac-guiding at 190 m/s (red) and 5 kV deceleration from 190 m/s to 30 m/s (blue). The deceleration measurement is obtained using both the hexapole and the improved waveform. The inset shows the peak structure due to the repeating electric field traps, which illustrates a similarity between the number of filled traps in ac-guiding and deceleration. The horizontal scale of the inset is chosen such that the traps overlap. The vertical scale is less meaningful, due to the different bin sizes (5 µs for ac-guiding versus 8 µs for deceleration) and total number of recorded shots (3000 for ac-guiding versus 72000 for deceleration.

change in the shape of the fluorescence signal is the presence of the electric field. A second example of the influence of the electric field on the fluorescence signal is shown in Figure 3.26, which compares the fluorescence signal of the guided peak for three 3.0 kV ac-guiding waveforms with different ramp-down times, along with the waveform used to generate the signal. The rampdown times varies from 1 to 8 trap widths. The shorted two ramp-down times show a sharp increase in the fluorescence signal around 28.0 ms, corresponding to the arrival of the synchronous molecule, once the voltage is reduced to zero. Comparison with the third or lowest fluorescence signal shows that this sharp increase is not simply due to the arrival of a trap containing significantly more molecules than its predecessor, as the height of the fluorescence signals around 28.0 ms does not significantly change.

As the number of fluorescence counts is the only observable which can be used in determining the intensity increase of the molecular beam due to the hexapole, eliminating the influence of the electric field on the fluorescence signal will also aid in obtaining a better match between simulations and measurements. The field should be minimized to an extent where the shift induced by the electric field is comparable to the MHz scale on which the laser can be locked, as the field would then no longer be the largest limiting factor on fluorescence efficiency. Since guiding out molecules has proven effective in increasing the number of filled traps (Section 3.5.1), eliminating the electric field by turning off the waveform earlier is not ideal. Therefore, some other method of eliminating the electric field from the detection zone was taken on. A grounded copper plate is to be mounted behind the last ring of the decelerator, as shown in Figure 3.27b. The plate is covered in black paint to minimize scattering, to reduce it's contribution to the background in the fluorescence signal. The distance between the last ring and the copper plate should be large enough to avoid discharges, yet small enough to not introduce significant transverse spreading of the beam before it reaches the detection zone. The plate has been manufactured and is currently awaiting installation. Laser cooling requires extensive control over electromagnetic fields, as to avoid falling off resonance and thereby inhibiting optical cycling. Therefore, installing the field shield is also a crucial step towards transverse laser cooling of the molecular beam.

3.6 Moving towards laser cooled BaF

Due to the implementation of the hexapole, the transverse velocity of molecules entering the decelerator will increase (Figure 3.10). However, due to the length of the interaction region (Figure 2.5) and additional vacuum elements, the molecular beam is required to propagate for ~ 2 m after exiting the decelerator. At the proposed longitudinal velocity of 30 m/s, this takes roughly 6 ms. With a transverse velocity of 5 m/s, the diameter of the molecular beam will increase to ~ 30 cm during the 6 ms propagation time. Therefore, the beam of BaF molecules requires some form of transverse cooling. The solution to this problem can be found in laser cooling, which can reduce the transverse temperature of a molecular beam enormously, resulting in an intense, highly collimated molecular beam [78]. To this end, an optical cycling transition has been identified [103], which will be used to create a two-dimensional optical molasses cooling mechanism [9]. Two-dimensional optical molasses is the result of velocity-selective transfer of photon momentum from a laser beam to a moving particle [104]. This section briefly describes the custom made vacuum chamber and optical elements required for the transition towards transverse laser cooling of BaF.

Two-dimensional optical molasses is a form of Doppler cooling which uses two sets of counterpropagating lasers with a frequency tuned slightly below the absorption resonance, as illustrated in Figure 3.28a. Due to the detuning, molecules moving antiparallel with respect to the cooling laser will absorb a photon more often compared to the laser oriented parallel to their direction of motion. Photons are only absorbed if they move antiparallel to the molecule's direction of motion, but can be emitted uniformly in all directions. Therefore, the next effect of the momentum transfer that occurs upon absorption of the photon is a reduction of the velocity of the molecule in the direction antiparallel to the cooling laser. This

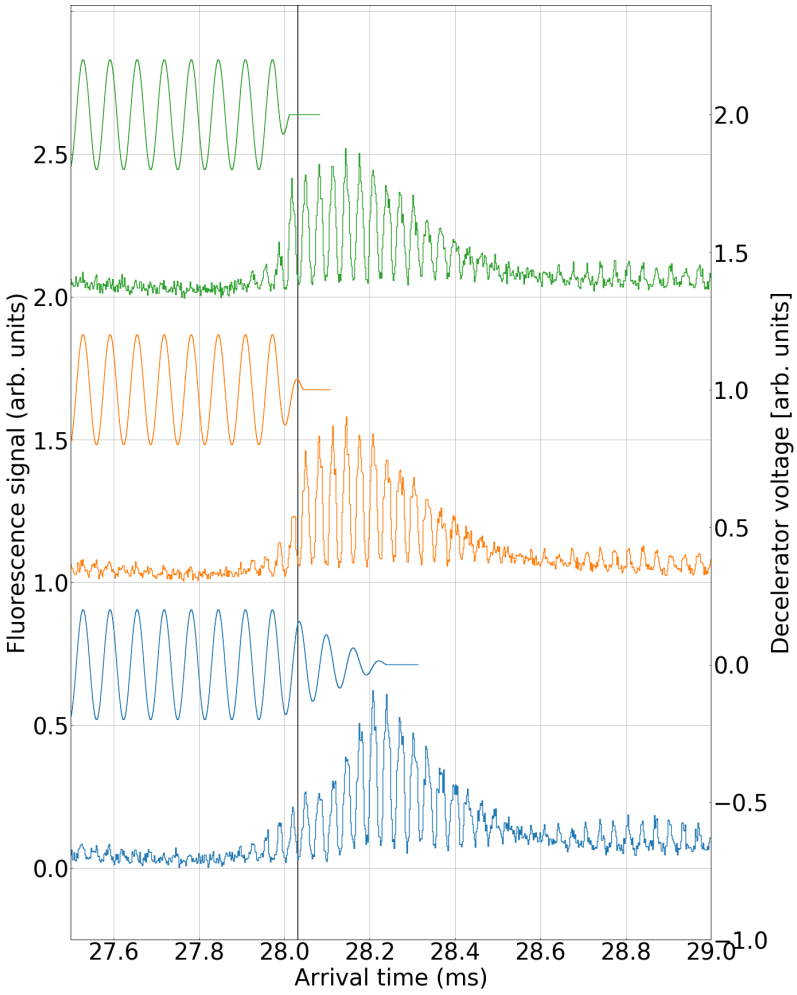

FIGURE 3.26: Fluorescence signal of the guided peak for three 3.0 kv ac-guiding waveforms with different ramp-down times, along with the waveform used to generate the signal. These measurements were obtained using 6000 shots.

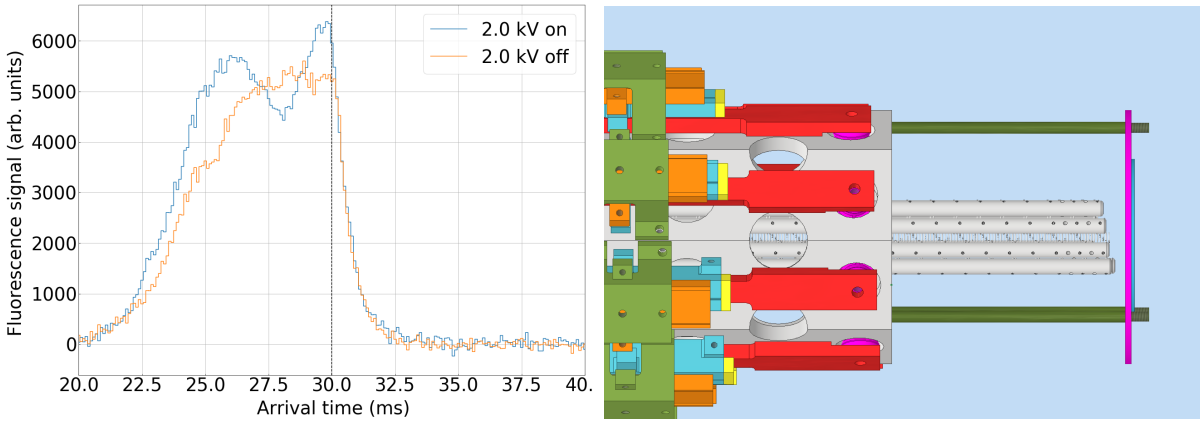

FIGURE 3.27: Fluorescence signal for two 2 kV dc-guiding waveforms that are turned off 30 ms after the ablation trigger. These waveforms differ only in the order in which the rings have a voltage applied to them. Consequently, one waveform has a voltage on the last ring (labeled 'on'), while the other has zero voltage on the last ring (labeled 'off'). **b)** Side view of the proposed electric field shield. A grounded, X shaped copper plate mounted behind the last ring of the decelerator shields the fluorescence detection zone from stray electric fields.

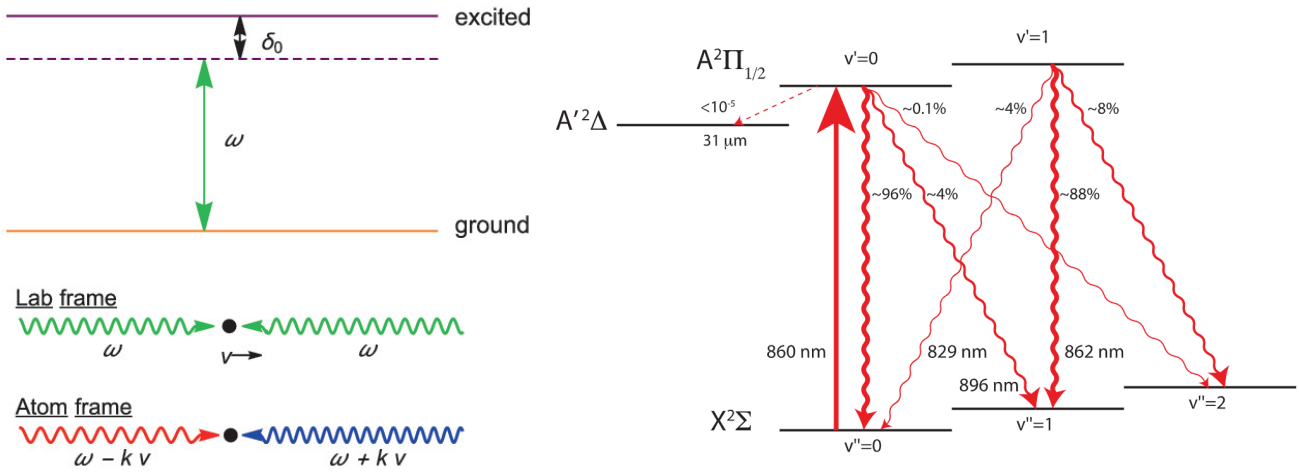

FIGURE 3.28: **a)** The principle of one-dimensional Doppler cooling applied to a two-level molecule. The laser at frequency ω used to drive the cooling transition has a detuning δ_0 such that the frequency of the laser is located slightly below resonance as seen from the lab frame. The detuning is chosen such that molecules propagating towards the cooling laser with a velocity v are on resonance, i.e. $\delta_0 = kv$. Figure from [78]. **b)** The cooling cycle identified for BaF, including wavelengths and branching ratios. Figure from [9].

creates a force linear in and opposed to the velocity of the molecule. Using optical molasses, molecules can be cooled to a temperature corresponding to the Doppler limit, where their minimum kinetic energy is essentially the same as the energy of a photon corresponding to the cooling transition [105]. The detuning of the laser frequency is swept so that all molecular velocities between the recoil limit and a maximum value are targeted.

In order to reliably scatter photons, a closed optical cycle needs to be selected. For BaF, the main transition identified for a closed cycle is the electronic $A^2\Pi_{1/2}(v' = 0, J = 1/2) \rightarrow X^2\Sigma^+(v' = 0, N = 1)$ transition, which is shown in Figure 3.28b [103]. This is the same transition previously employed for successful laser cooling of SrF [67]. The addition of two repump lasers to couple the vibrational $v = 1, v = 2$ levels of the $X^2\Sigma$ state to the $A^2\Pi_{1/2}$ state is estimated to produce a relatively closed cycle, meaning that on average enough photons can be scattered to dissipate the transverse velocity before a transition to a dark, vibrational state occurs. Furthermore, while the hyperfine splitting of the excited state is unresolved, the hyperfine splitting of the ground state presents a possible leak in the cooling cycle. The hyperfine splitting of the $N = 1$ level of $X^2\Sigma^+(v = 0)$ BaF is shown in Figure 3.29, with values comparable to those found in [106][79]. In order to couple each hyperfine level of the ground $X^2\Sigma^+(v = 0)$ state to the excited $A^2\Pi_{1/2}(v' = 0, J = 1/2)$ state, a number of acousto-optic modulators (AOM) will be used. An AOM can change the frequency of an input laser based on the electronic signal applied to it. The main Ti:Sa laser[1] in combination with three AOMs will target all four hyperfine levels.

The final design of the custom vacuum chamber where the molecules will undergo transverse laser cooling is shown in Figure 3.30. The molecules which exit the decelerator will have a maximum transverse velocity of $v_{T,RMS} = \sqrt{2k_BT/m} \approx 5$ m/s. A single photon at 860 nm results in a recoil for the BaF molecule of ~ 3 mm/s. Taking into account the fact that not every photon will produce a maximum recoil effect, ~ 2000 photon scatterings are required to dissipate a transverse velocity of ≈ 5 m/s. Since the lifetime of the $A^2\Pi_{1/2}(v' = 0, J = 1/2)$ state is ~ 50 ns [107], a molecule will propagate ~ 30 mm in the longitudinal direction during the laser cooling process. During the cooling process, the beam is expected to spread to a width of ~ 1 cm [9].

[1] MSQUARED SolsTiS

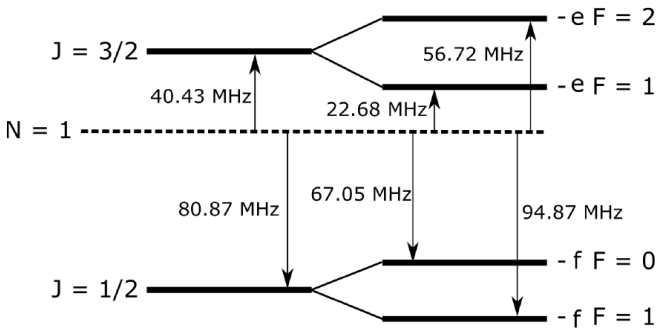

FIGURE 3.29: Hyperfine splitting of the $N = 1$ level of $X^2\Sigma^+(v = 0)$ BaF [100].

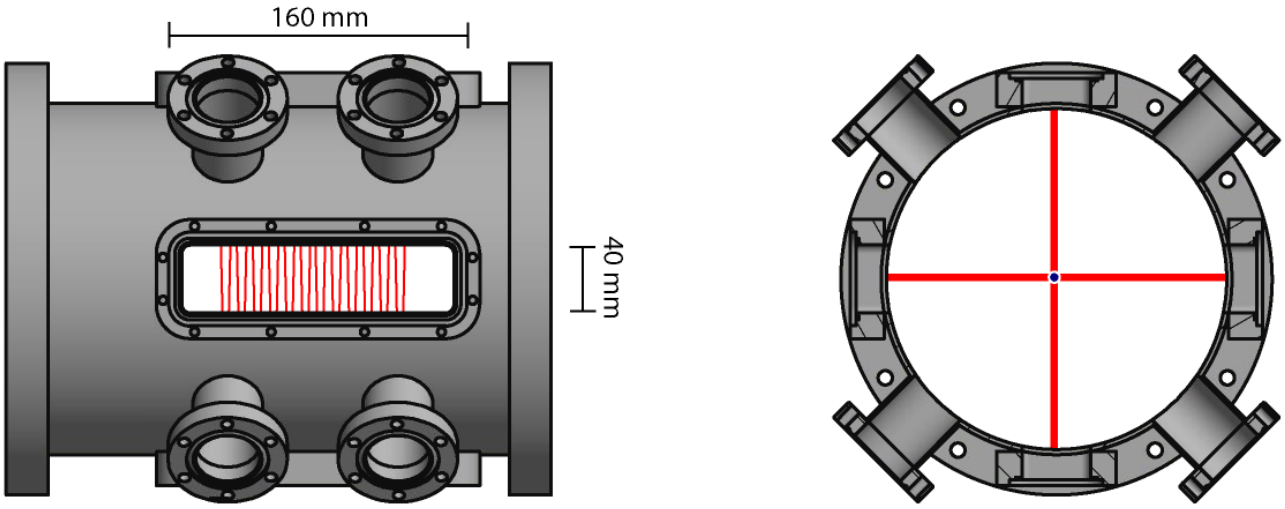

FIGURE 3.30: Schematic side view (left) and front view (right) of the vacuum chamber in which the molecular beam will undergo transverse laser cooling using a 2D optical molasses approach. Using mirrors mounted at each rectangular window, the cooling lasers (red) will repeatedly cross the vacuum chamber. In the drawing on the left, the molecular beam would enter the chamber from the left side, and the last few rings of the decelerator will be visible through the windows. The numbers indicate the dimensions of the cooling windows. An estimated $\sim$ 2000 scatterings of the 860 nm (red) laser are required to dissipate the $\approx$ 5 m/s transverse velocity of the molecular beam (blue) [9].

3.7 Conclusion

The overarching objective of the work presented in this chapter is to increase the intensity of the SrF molecular beam, in order to eventually provide the required intensity of a BaF molecular beam for a competitive measurement of the eEDM [9]. In order to improve molecular transfer between the source and the decelerator, an electrostatic hexapole is designed, built and implemented between the source and decelerator. The electric field inside the hexapole causes the molecules to experience a Stark shift, depending on their radial position. The molecular beam originates from a 4.5 mm radius orifice instead of a point source and the hexapole creates an anharmonic potential for the low field seeking molecules in the $X^2\Sigma^+(v' = 0, N = 1)$ state. Therefore, the electrostatic hexapole lens creates a soft focus rather than focusing to the exact initial distribution, like a perfect lens would.

The hexapole lens is designed to optimize filling of the area in the phase space acceptance of the decelerator near the separatrix, for molecules with a relatively large transverse velocity, as shown in Figure 3.9 and Figure 3.10. However, the fluorescence detection laser does not fully sample the transverse dimensions of the decelerated molecular beam, as shown in Figure 3.19. Consequently, these transversely fast molecules are likely not detected, both due to the increased size of the molecular packet located in each electric field trap, and the increased divergence of the beam.

A number of molecular trajectory simulations are conducted and compared to the measured hexapole voltage dependent fluorescence signal. From this comparison, a factor 2 increase in the detected number of molecules due to installation of the hexapole is estimated. However, this comparison likely underestimates the true gain factor. The simulations used a multiplicity of currently not directly measured parameters, i.e. the decelerator position and velocity acceptance and the transverse dimensions of the fluorescence detection volume. Multiple combinations of these parameters can likely be found which display a close agreement between the simulated and measured curve. Therefore, it is difficult to ascertain the precise factor of increase in the number of decelerated molecules originating from the implementation of the hexapole. The unknown parameters have to be measured separately first, using for instance an EMCCD camera to measure the transverse width of the guided or decelerated beam.

Next, the voltage waveform is optimized by adding two sections of ac-guiding before and after the deceleration section, to reduce transverse losses that occur due to the waveform turning off before molecules reach the detection zone. The combined effect of both the installation of the hexapole and the added sections of ac-guiding to the waveform is an increase in the number of packets or buckets that can be distinguished in the deceleration to 30 m/s time-of-flight signal. Consequently, the gain factor in number of molecules obtained at the end of the decelerator due to the addition of the hexapole when decelerating to 30 m/s is likely larger than the factor 2 obtained using ac-guiding at 190 m/s. Furthermore, the number of filled traps obtained in deceleration to 30 m/s is very similar to that of an ac-guiding measurement, which shows a step in the direction of the efficient deceleration required for the final eEDM experiment. The implementation of an electric field shield is also discussed, which will reduce the influence of the electric field on the fluorescence measurement and the planned transverse laser cooling.

The chapter ends by describing preparatory work conducted for the transition towards laser cooled BaF. A custom vacuum chamber has been designed, where two-dimensional transverse laser cooling of the molecular beam will take place. A Ti:Sa laser is installed, which will generate the infrared light required for transverse laser cooling of the BaF molecular beam.

Chapter 4

Summary and outlook

Heavy polar diatomic molecules can be used as sensitive probes of violations of fundamental symmetries. One such symmetry violation is a nonzero magnitude of the electron electric dipole moment, or eEDM. A measured value of the eEDM larger than the prediction of the Standard Model is a possible sign of physics beyond the Standard Model. The NL-eEDM collaboration works towards a measurement of the eEDM using a slow, cold and intense beam of BaF molecules. The main motivation for the work conducted in this thesis is increasing the intensity of the molecular beam, a necessary step towards a competitive eEDM measurement.

An outline for the field of eEDM experiments in relation to fundamental physics is provided by discussing the history and types of EDM experiments. A discussion of the experimental signature of an eEDM and the parameters which govern the sensitivity of an eEDM measurement is used to describe the elements required for an eEDM experiment. Next, the setup proposed by the NL-eEDM collaboration is discussed. As this thesis mainly concerns beam production, special attention is paid to the elements required for generating the slow, cold and intense molecular beam.

The traveling-wave Stark decelerator generates a controllable moving potential trap for low electric field seeking molecules, using time-varying electric fields. The SrF molecular beam is generated using a cryogenic buffer gas source. The decelerated beam is detected using laser induced fluorescence. The source is designed to feature a phase space emittance that fully overlaps with the phase space acceptance of the decelerator. However, the molecular beam experiences a free flight of 369 mm between the source and the decelerator, during which the beam is free to spread in the transverse direction. Due to the geometry of the decelerator rings, only molecules with a small transverse velocity enter the decelerator. If the divergent part of the molecular beam can be focused into the decelerator, an increased number of decelerated molecules can be obtained.

An electrostatic hexapole is designed, built, implemented and tested in order to focus the divergent part of the molecular beam into the decelerator. The quadratic electric field created by the hexapole induces a Stark shift that varies depending on the radial position of molecules inside the hexapole, which can create a transverse force for low field seeking molecules. For the electric field strengths inside the hexapole, the molecules located in the low field seeking $X^2\Sigma^+(\nu = 0, N = 1)$ state display a Stark shift that varies linearly or quadratically, depending on their radial distance. A quadratic or linear Stark shift requires a linear or quadratic electric field to produce a harmonic potential, respectively. Consequently, the molecules experience an anharmonic potential in the transverse direction while propagating through the hexapole, which leads to a soft focus. The lensing effect of the hexapole is estimated to increase the number of decelerated SrF molecules by at least a factor 2, after comparing measured fluorescence data to molecular trajectory simulations. A definitive conclusion on the intensity increase which can be attributed to the hexapole is currently impossible. The hexapole is designed to fully fill the phase space acceptance of the decelerator, and consequently, the phase space distribution of the molecular packets exiting the decelerator will resemble the phase space acceptance of the decelerator. However, the width of the detection laser is currently much smaller than the inner diameter of the decelerator rings.

Therefore, only a small fraction of the total amount of guided or decelerated molecules is detected. The simulations show that a decrease in decelerated number of molecules for varying hexapole voltages due to a change in the decelerator acceptance, can be negated by a change in the detection volume. Therefore, many combinations of the decelerator acceptance and detection volume can be found to produce an agreement with the measured data. Consequently, in order to compare simulation to measured data, either the complete decelerated package has to be detected, or the decelerator acceptance and detection zone have to be determined independently.

The combined effect of the hexapole lens and the addition of ac-guiding sections to the waveform are shown to increase the number of detected molecular packets in the fluorescence time of flight signal. An electric field shield is designed to minimize the influence of latent electric fields on the fluorescence measurement. Furthermore, the number of filled traps obtained in deceleration to 30 m/s is very similar to that of an ac-guiding measurement, which shows a step in the direction of the efficient deceleration required for the final eEDM experiment.

With the hexapole lens in place, the focus can turn towards transverse laser cooling of BaF. The transverse velocity of the beam has to be reduced in order for the molecular beam to propagate without loss of intensity for ~ 2 m through the remainder of the NL-eEDM setup. A custom vacuum chamber where the laser cooling will occur is designed. A form of Doppler cooling dubbed two dimensional optical molasses will be employed to dissipate the transverse velocity of the decelerated molecules. The possibility of attempting sub-Doppler cooling is not ruled out. Reducing the tranverse velocity of the beam is an essential step towards an eEDM measurement using a slow, intense and cold beam of BaF molecules.

Acknowledgements

I would like to extend my gratitude towards all members of the Cold Molecules group, but in particular to my first examiner Steven and Anno. Steven, I would like to thank you for providing me the opportunity to become acquainted with conducting scientific research. Your enthusiasm in both talking about the details of an experiment and doing hands on work in the laboratory is infectious, and I hope the coming years will bring many more conversations about the decelerator and all of it's intricacies. Anno, I have thoroughly enjoyed working alongside you. I think you contribute a valuable combination of physical insight, critical thinking and uplifting attitude to the experiment. The past year of 'deeltjes toeteren' has been a wonderful experience, and I am glad that we will be able to continue doing so. Leo, I appreciate your unwavering technical support and cheerful greetings every morning. Parul and Yanning, your steadfast approach to solving problems is remarkable, and I have learned a lot about the decelerator from you. Mina, your humour, nanospheres and snack cabinet always presented a welcome break from the noise of the amplifiers.

Furthermore, I would like to thank all members of the NL-eEDM collaboration, with a special focus on Hendrick Bethlem, for the detailed discussions about Stark shifts, phase space and constructing molecular lenses from electrostatic multipoles, and Lorenz Willmann, for providing valuable feedback on my thesis.

Bibliography

[1] CDF Collaboration. "Observation of Top Quark Production in $\bar{p}p$ Collisions with the Collider Detector at Fermilab". In: *Phys. Rev. Lett.* 74 (14 1995), pp. 2626–2631. DOI: 10.1103/PhysRevLett.74.2626.

[2] ATLAS Collaboration. "Observation of a new particle in the search for the Standard Model Higgs boson with the ATLAS detector at the LHC". In: *Physics Letters B* 716.1 (2012), pp. 1–29. ISSN: 0370-2693. DOI: https://doi.org/10.1016/j.physletb.2012.08.020.

[3] C. Wetterich. "Where to look for solving the gauge hierarchy problem?" In: *Physics Letters B* 718.2 (2012), pp. 573–576. DOI: https://doi.org/10.1016/j.physletb.2012.11.020.

[4] G. R. Blumenthal et al. "Formation of galaxies and large-scale structure with cold dark matter". In: *Nature* 311.5986 (1984), pp. 517–525.

[5] J. Ellis. "Outstanding questions: physics beyond the Standard Model". In: *Philosophical Transactions of the Royal Society A: Mathematical, Physical and Engineering Sciences* 370.1961 (2012), pp. 818–830.

[6] M. E. Shaposhnikov. "Standard model solution of the baryogenesis problem". In: *Physics Letters B* 277.3 (1992), pp. 324–330. DOI: https://doi.org/10.1016/0370-2693(92)90753-Q.

[7] B. Abi et al. "Measurement of the Positive Muon Anomalous Magnetic Moment to 0.46 ppm". In: *Phys. Rev. Lett.* 126 (14 2021). DOI: 10.1103/PhysRevLett.126.141801.

[8] W. N. Cottingham and D. A. Greenwood. *An introduction to the standard model of particle physics*. 2nd ed. Cambridge University Press, 2007.

[9] The NL-eEDM collaboration et al. "Measuring the electric dipole moment of the electron in BaF". In: *The European Physical Journal D* 72.11 (2018), p. 197. DOI: 10.1140/epjd/e2018-90192-9.

[10] M. Kobayashi and T. Maskawa. "CP-violation in the renormalizable theory of weak interaction". In: *Progress of theoretical physics* 49.2 (1973), pp. 652–657.

[11] W. Bernreuther and M. Suzuki. "The electric dipole moment of the electron". In: *Reviews of Modern Physics* 63.2 (1991), p. 313.

[12] E. Hinds and B. Sauer. "Electron dipole moments". In: *Physics World* 10.4 (1997), p. 37.

[13] N. R. Hutzler. "A new limit on the electron electric dipole moment: beam production, data interpretation, and systematics". PhD thesis. 2014.

[14] Z. Lasner. "Order-of-Magnitude-Tighter Bound on the Electron Electric Dipole Moment". PhD thesis. Yale University, 2019.

[15] J. H. Christenson et al. "Evidence for the 2π Decay of the K_2^0 Meson". In: *Phys. Rev. Lett.* 13 (4 1964), pp. 138–140. DOI: 10.1103/PhysRevLett.13.138.

[16] J. Engel, M. J. Ramsey-Musolf, and U. van Kolck. "Electric dipole moments of nucleons, nuclei, and atoms: The Standard Model and beyond". In: *Progress in Particle and Nuclear Physics* 71 (2013), pp. 21–74.

[17] T. Fukuyama. "Searching for new physics beyond the standard model in electric dipole moment". In: *International Journal of Modern Physics A* 27.16 (2012), p. 1230015.

[18] T. Ibrahim and P. Nath. "*CP* violation from the standard model to strings". In: *Rev. Mod. Phys.* 80 (2 2008), pp. 577–631. DOI: 10.1103/RevModPhys.80.577.

[19] E. M. Purcell and N. F. Ramsey. "On the possibility of electric dipole moments for elementary particles and nuclei". In: *Physical Review* 78.6 (1950), p. 807.

[20] K. Esajas. "Intense slow beams of heavy molecules to test fundamental symmetries". In: (2021).

[21] Y. Nakai and M. Reece. "Electric dipole moments in natural supersymmetry". In: *Journal of High Energy Physics* 2017.8 (2017), pp. 1–53.

[22] N. F. Ramsey. "Electric-dipole moments of elementary particles". In: *Reports on progress in physics* 45.1 (1982), p. 95.

[23] N. F. Ramsey. "Electric dipole moment of the neutron". In: *Annual Review of Nuclear and Particle Science* 40.1 (1990), pp. 1–14.

[24] J. E. Kim and G. Carosi. "Axions and the strong C P problem". In: *Reviews of Modern Physics* 82.1 (2010), p. 557.

[25] B. Graner et al. "Reduced limit on the permanent electric dipole moment of hg 199". In: *Physical review letters* 116.16 (2016), p. 161601.

[26] J. Dragos et al. "Confirming the existence of the strong CP problem in lattice QCD with the gradient flow". In: *Phys. Rev. C* 103 (1 2021), p. 015202. DOI: 10.1103/PhysRevC.103.015202.

[27] M. Pospelov and A. Ritz. "Theta vacua, QCD sum rules, and the neutron electric dipole moment". In: *Nuclear Physics B* 573.1-2 (2000), pp. 177–200.

[28] M. Dine. "TASI lectures on the strong CP problem". In: *arXiv preprint hep-ph/0011376* (2000).

[29] P. G. H. Sandars. "Electric dipole moments of charged particles". In: *Contemporary Physics* 42.2 (2001), pp. 97–111.

[30] A. Sunaga et al. "Enhancement factors of parity-and time-reversal-violating effects for monofluorides". In: *Physical Review A* 98.4 (2018), p. 042511.

[31] P. A. B. Haase et al. "Systematic study and uncertainty evaluation of P, T-odd molecular enhancement factors in BaF". In: *The Journal of Chemical Physics* 155.3 (2021), p. 034309. DOI: 10.1063/5.0047344. URL: https://doi.org/10.1063/5.0047344.

[32] A. C. Vutha et al. "Search for the electric dipole moment of the electron with thorium monoxide". In: *Journal of Physics B: Atomic, Molecular and Optical Physics* 43.7 (2010), p. 074007.

[33] L. I. Schiff. "Measurability of nuclear electric dipole moments". In: *Physical Review* 132.5 (1963), p. 2194.

[34] E. D. Commins, J. D. Jackson, and D. P. DeMille. "The electric dipole moment of the electron: An intuitive explanation for the evasion of Schiff's theorem". In: *American Journal of Physics* 75.6 (2007), pp. 532–536.

[35] E. A. Hinds. "Testing time reversal symmetry using molecules". In: *Physica Scripta* 1997.T70 (1997), p. 34.

[36] Yannis K Semertzidis. "Review of EDM experiments". In: *Journal of Physics: Conference Series*. Vol. 335. 1. IOP Publishing. 2011, p. 012012.

[37] J. Engel, M. J. Ramsey-Musolf, and U. Van Kolck. "Electric dipole moments of nucleons, nuclei, and atoms: The Standard Model and beyond". In: *Progress in Particle and Nuclear Physics* 71 (2013), pp. 21–74.

[38] V. V. Flambaum et al. "Sensitivity of EDM experiments in paramagnetic atoms and molecules to hadronic *CP* violation". In: *Phys. Rev. D* 102 (3 2020), p. 035001. DOI: 10.1103/PhysRevD.102.035001.

[39] P. Sushkov and V. V. Flarnbaurn. "Parity breaking effects in diatomic molecules". In: *Zh. Eksp. Teor. Fiz* 75 (1978), pp. 1208–1213.

[40] J. Lim et al. "Laser Cooled YbF Molecules for Measuring the Electron's Electric Dipole Moment". In: *Physical Review Letters* 120.12 (2018), p. 123201. ISSN: 0031-9007. DOI: 10.1103/physrevlett.120.123201. eprint: 1712.02868.

[41] N. R. Hutzler et al. "Searches for new sources of CP violation using molecules as quantum sensors". In: *arXiv preprint arXiv:2010.08709* (2020).

[42] M. Pospelov and A. Ritz. "Electric dipole moments as probes of new physics". In: *Annals of Physics* 318.1 (2005), pp. 119–169. DOI: https://doi.org/10.1016/j.aop.2005.04.002.

[43] M. Pospelov and A. Ritz. "CKM benchmarks for electron electric dipole moment experiments". In: *Phys. Rev. D* 89 (5 2014), p. 056006. DOI: 10.1103/PhysRevD.89.056006.

[44] V. Andreev and N. R. Hutzler. "Improved limit on the electric dipole moment of the electron". In: *Nature* 562.7727 (2018), pp. 355–360.

[45] Van Swinderen Institute. *electron-EDM*. https://www.rug.nl/research/vsi/newtopics/eedm.

[46] N. Fortson, P. Sandars, and S. Barr. "The search for a permanent electric dipole moment". In: *Physics Today* 56.6 (2003), pp. 33–39.

[47] W. B. Cairncross and J. Ye. "Atoms and molecules in the search for time-reversal symmetry violation". In: *Nature Reviews Physics* 1.8 (2019), pp. 510–521.

[48] J. J. Hudson. "Measuring the electric dipole moment of the electron with YbF molecules". PhD thesis. University of Sussex, 2001.

[49] W. C. Campbell et al. "Advanced cold molecule electron EDM". In: *EPJ Web of Conferences*. Vol. 57. EDP Sciences. 2013, p. 02004.

[50] J. J. Hudson et al. "Improved measurement of the shape of the electron". In: *Nature* 473.7348 (2011), pp. 493–496.

[51] C. D. Panda et al. "Attaining the shot-noise-limit in the ACME measurement of the electron electric dipole moment". In: *Journal of Physics B: Atomic, Molecular and Optical Physics* 52.23 (2019), p. 235003.

[52] J. Baron et al. "Methods, analysis, and the treatment of systematic errors for the electron electric dipole moment search in thorium monoxide". In: *New Journal of Physics* 19.7 (2017), p. 073029.

[53] M. R. Tarbutt et al. "A jet beam source of cold YbF radicals". In: *Journal of Physics B: Atomic, Molecular and Optical Physics* 35.24 (2002), p. 5013.

[54] S. M. Skoff. "Buffer gas cooling of YbF molecules". In: (2011).

[55] M. Abe et al. "Application of relativistic coupled-cluster theory to the effective electric field in YbF". In: *Physical Review A* 90.2 (2014), p. 022501.

[56] W. B. Cairncross et al. "Precision measurement of the electron's electric dipole moment using trapped molecular ions". In: *Physical review letters* 119.15 (2017), p. 153001.

[57] E. R. Meyer and J. L. Bohn. "Prospects for an electron electric-dipole moment search in metastable ThO and Th F+". In: *Physical Review A* 78.1 (2008), p. 010502.

[58] A. E. Leanhardt et al. "High-resolution spectroscopy on trapped molecular ions in rotating electric fields: A new approach for measuring the electron electric dipole moment". In: *Journal of Molecular Spectroscopy* 270.1 (2011), pp. 1–25.

[59] T. E. Chupp et al. "Electric dipole moments of atoms, molecules, nuclei, and particles". In: *Rev. Mod. Phys.* 91 (1 2019), p. 015001. DOI: 10.1103/RevModPhys.91.015001.

[60] C. J. Ho et al. "New techniques for a measurement of the electron's electric dipole moment". In: *New Journal of Physics* 22.5 (2020), p. 053031.

[61] D. DeMille. "Diatomic molecules, a window onto fundamental physics". In: *Physics Today* 68.12 (2015), pp. 34–40.

[62] M. A. Trigatzis. "An ultracold molecular beam for measuring the electric dipole moment of the electron". In: (2020).

[63] D. N. Gresh et al. "Broadband velocity modulation spectroscopy of ThF+ for use in a measurement of the electron electric dipole moment". In: *Journal of Molecular Spectroscopy* 319 (2016), pp. 1–9.

[64] P. Aggarwal et al. "Deceleration and trapping of SrF molecules". In: *arXiv preprint arXiv:2103.07968* (2021).

[65] J. E. van den Berg. "Traveling-wave Stark deceleration of SrF molecules". In: (2015).

[66] A. Zapara. "Dynamics of molecular beams in a traveling-wave Stark decelerator". In: (2019).

[67] J. F. Barry. *Laser cooling and slowing of a diatomic molecule*. Yale University, 2013.

[68] I. V. Hertel and C. Schulz. *Atoms, molecules and optical physics*. Springer, 2014.

[69] M. Brieger. "Stark effect, polarizabilities and the electric dipole moment of heteronuclear diatomic molecules in 1Σ states". In: *Chemical physics* 89.2 (1984), pp. 275–295.

[70] H. L. Bethlem et al. "Alternating gradient focusing and deceleration of polar molecules". In: *Journal of Physics B: Atomic, Molecular and Optical Physics* 39.16 (2006), R263.

[71] S. Y. T. van de Meerakker et al. "Manipulation and control of molecular beams". In: *Chemical reviews* 112.9 (2012), pp. 4828–4878.

[72] J. R. Meinema. "Obtaining ultracold molecules through Stark deceleration and laser cooling". In: (2016).

[73] H. L. Bethlem et al. "Deceleration and trapping of ammonia using time-varying electric fields". In: *Physical Review A* 65.5 (2002), p. 053416.

[74] S. C. Mathavan et al. "Deceleration of a supersonic beam of SrF molecules to 120 m/s". In: *arXiv preprint arXiv:1609.09734* (2016).

[75] P. Aggarwal et al. "A supersonic laser ablation beam source with narrow velocity spreads". In: *Review of Scientific Instruments* 92.3 (2021), p. 033202.

[76] S. N. Vogels, Z. Gao, and S. Y. T. van de Meerakker. "Optimal beam sources for Stark decelerators in collision experiments: a tutorial review". In: *EPJ techniques and instrumentation* 2.1 (2015), p. 12.

[77] N. R. Hutzler, H. Lu, and J. M. Doyle. "The buffer gas beam: An intense, cold, and slow source for atoms and molecules". In: *Chemical reviews* 112.9 (2012), pp. 4803–4827.

[78] N. J. Fitch and M. R. Tarbutt. "From Hot Beams to Trapped Ultracold Molecules: Motivations, Methods and Future Directions". In: *Molecular Beams in Physics and Chemistry*. Springer, 2021, pp. 491–516.

[79] R. Albrecht et al. "Buffer-gas cooling, high-resolution spectroscopy, and optical cycling of barium monofluoride molecules". In: *Physical Review A* 101.1 (2020), p. 013413.

[80] A. Aggarwal. "Production, deceleration and trapping of SrF molecules". PhD thesis. 2021. DOI: 10.33612/diss.177484581.

[81] M. D. Di Rosa. "Laser-cooling molecules". In: *The European Physical Journal D-Atomic, Molecular, Optical and Plasma Physics* 31.2 (2004), pp. 395–402.

[82] E. S. Shuman et al. "Radiative force from optical cycling on a diatomic molecule". In: *Physical review letters* 103.22 (2009), p. 223001.

[83] J. Kändler, T. Martell, and W. E. Ernst. "Electric dipole moments and hyperfine structure of SrF A 2Π and B 2Σ+". In: *Chemical physics letters* 155.4-5 (1989), pp. 470–474.

[84] E. S. Shuman, J. F. Barry, and D. DeMille. "Laser cooling of a diatomic molecule". In: *Nature* 467.7317 (2010), pp. 820–823.

[85] A. J. Lichtenberg. "Phase-space dynamics of particles". In: (1969).

[86] T. D. Hain, R. M. Moision, and T. J. Curtiss. "Hexapole state-selection and orientation of asymmetric top molecules: CH2 F2". In: *The Journal of chemical physics* 111.15 (1999), pp. 6797–6806.

[87] T. Cremers et al. "Multistage Zeeman decelerator for molecular-scattering studies". In: *Physical Review A* 95.4 (2017), p. 043415.

[88] A. P. P. Van Der Poel et al. "A compact design for a magnetic synchrotron to store beams of hydrogen atoms". In: *New Journal of Physics* 17.5 (2015), p. 055012.

[89] A. Sørensen. "Liouville's theorem and emittance". In: (1989).

[90] F. M. H. Crompvoets et al. "Longitudinal focusing and cooling of a molecular beam". In: *Physical review letters* 89.9 (2002), p. 093004.

[91] J.B. Marion and S.T. Thornton. *Classical dynamics of particles and systems*. Academic Press, 1965.

[92] F. M. H. Crompvoets, H. L. Bethlem, and G. Meijer. "A storage ring for neutral molecules". In: *Advances in atomic, molecular, and optical physics* 52 (2005), pp. 209–287.

[93] B. Bertsche and A. Osterwalder. "State-selective detection of velocity-filtered ND 3 molecules". In: *Physical Review A* 82.3 (2010), p. 033418.

[94] J. J. Everdij, A. Huijser, and N. F. Verster. "Improved space focusing of polar diatomic molecules in a system of quadrupole and hexapole fields". In: *Review of Scientific Instruments* 44.6 (1973), pp. 721–725.

[95] S. Y. T. Van De Meerakker, H. L. Bethlem, and G. Meijer. "Taming molecular beams". In: *Nature Physics* 4.8 (2008), pp. 595–602.

[96] R. W. Anderson. "Tracks of symmetric top molecules in hexapole electric fields". In: *The Journal of Physical Chemistry A* 101.41 (1997), pp. 7664–7673.

[97] V. V. Zashkvara and N. N. Tyndyk. "Electrostatic axially symmetric multipole in deflector-type analyzers". In: *Nuclear Instruments and Methods in Physics Research Section A: Accelerators, Spectrometers, Detectors and Associated Equipment* 313.3 (1992), pp. 315–327.

[98] W. E. Ernst, J. Kändler, and T. Törring. "Hyperfine structure and electric dipole moment of BaF X 2Σ+". In: *The Journal of chemical physics* 84.9 (1986), pp. 4769–4773.

[99] A. C. Vutha, M. Horbatsch, and E. A. Hessels. "Orientation-dependent hyperfine structure of polar molecules in a rare-gas matrix: A scheme for measuring the electron electric dipole moment". In: *Physical Review A* 98.3 (2018), p. 032513.

[100] J. Maat. "Calculations on the energy level structure and the effects of external fields in barium monofluoride and The design and construction of an optical trap for nanoparticles as vibration sensors". PhD thesis. June 2018.

[101] M. Cohen, T. Feldmann, and S. Kais. "Stark effect of a rigid rotor". In: *Journal of Physics B: Atomic and Molecular Physics* 17.17 (1984), p. 3535.

[102] A. A. K. Mohammed, P. A Limacher, and B. Champagne. "Finding optimal finite field strengths allowing for a maximum of precision in the calculation of polarizabilities and hyperpolarizabilities". In: *Journal of computational chemistry* 34.17 (2013), pp. 1497–1507.

[103] Y. Hao et al. "High accuracy theoretical investigations of CaF, SrF, and BaF and implications for laser-cooling". In: *The Journal of chemical physics* 151.3 (2019), p. 034302.

[104] A. M. Sessler. "The cooling of particle beams". In: *AIP Conference Proceedings*. Vol. 356. 1. American Institute of Physics. 1996, pp. 391–407.

[105] P. D. Lett et al. “Optical molasses”. In: *JOSA B* 6.11 (1989), pp. 2084–2107.

[106] T. Chen, W. Bu, and B. Yan. “Structure, branching ratios, and a laser-cooling scheme for the BaF 138 molecule”. In: *Physical Review A* 94.6 (2016), p. 063415.

[107] P. Aggarwal et al. “Lifetime measurements of the $A\ ^2\Pi_{1/2}$ and $A\ ^2\Pi_{3/2}$ states in BaF”. In: *Phys. Rev. A* (). DOI: 10.1103/PhysRevA.100.052503.